

**EVALUATION OF LOGGERHEAD SEA TURTLE CARAPACE
PROPERTIES AND PROTOTYPE BIOMIMETIC
CARAPACE FABRICATION**

*A Thesis
Presented to
The Academic Faculty*

By

Justin E. Hodges

*In Partial Fulfillment
Of the Requirements for the Degree
Master of Science in Civil Engineering*

Georgia Institute of Technology

December 2008

**EVALUATION OF LOGGERHEAD SEA TURTLE CARAPACE
PROPERTIES AND PROTOTYPE BIOMIMETIC
CARAPACE FABRICATION**

Approved by:

Dr. David W. Scott, Chair
School of Civil and Environmental Engineering
Georgia Institute of Technology

Dr. Paul Work
School of Civil and Environmental Engineering
Georgia Institute of Technology

Dr. Kimberly Kurtis
School of Civil and Environmental Engineering
Georgia Institute of Technology

Date Approved: 10/2/2008

Acknowledgements

First, I would like to express sincere gratitude and respect for my thesis advisor, Dr David Scott, for his role as my primary mentor. Without his guidance, patience, and motivation this thesis would not have been possible. I would like to acknowledge Dr. Paul Work as a critical resource throughout this research project and Dr. Kimberly Kurtis for serving on my thesis committee.

In addition, I would like to thank my colleagues Andrew Fiser, Chad Spurlock, and Yavuz Menten for their friendship and insight throughout the duration of this work. Their companionship made each day enjoyable. Gratitude must also be expressed to Mark Dodd and the Georgia Department of Natural Resources for funding the study and supplying much needed information and experimental specimens.

I would also like to thank my family for their never ending support. Finally, I would like to express my deepest gratitude for my fiancée, Kassy McBurney, for her patience, understanding, and encouragement throughout my academic career.

Table of Contents

Acknowledgments	iii
List of Tables	vii
List of Figures	ix
Nomenclature	xiii
Summary	xv
Chapter 1 Introduction	1
Chapter 2 Previous Work	4
2.1 Carapace Composition	4
2.2 Review of Coupon Harvesting and Preservation Techniques	5
2.3 Review of Biological Material Testing Procedures	6
2.4 Review of Methods for Developing Biomimetic Materials	10
2.5 Significance of Vessel Strikes on Sea Turtle Mortality Rates	13
Chapter 3 Coupon Harvesting and Preparation	15
3.1 Classification of Loggerhead Injuries	15
3.2 Coupon Harvesting	16
3.3 Preservation Methodology	19
Chapter 4 Development of Test Procedures and Data Collection	20
4.1 Specialized Tab Design	21
4.2 Comparison of Rigid and Specialized Tabs	24

4.3 Tensile Test Procedure	30
4.4 Summary of Tensile Test Results – Carapace 1	33
4.5 Summary of Tensile Test Results – Carapace 2	37
4.6 Consideration of Additional Normal Stress Due to Bending	42
4.7 Flexural Test Procedures and Data Collection	45
Chapter 5	
Effects of Sample Geometry on Experimental Results and Determination of Target Properties	52
5.1 Effects of Sample Geometry on Tensile Strength	53
5.2 Effects of Sample Geometry on Strain at Failure	55
5.3 Effects of Sample Geometry on Tensile Modulus	56
5.4 Relationship between Sample Thickness and Tensile Load Capacity	58
5.5 Determination of Target Properties	60
Chapter 6	
Prototype Fabrication and Evaluation	63
6.1 Candidate Materials for Synthetic Shell Fabrication	63
6.2 Evaluation of Prototype Fabrication Techniques	65
6.3 Mold Fabrication	66
6.4 Fabrication and Evaluation of Synthetic Carapace 1	69
6.5 Fabrication and Evaluation of Synthetic Carapace 2	74
6.6 Production Methodology	83
Chapter 7	
Conclusions	85
7.1 Conclusions	85
7.2 Recommendations for Continuing Tests	87

Appendix A	Tensile Stress-Strain Plots – Carapace 1	90
Appendix B	Tensile Stress-Strain Plots – Carapace 2	97
Appendix C	Tensile Stress-Strain Plots – Carapace 3	111
Appendix D	Three-Point Bending Load-Deformation Plots – Carapace 3	117
Appendix E	Sample Dimensions	126
Appendix F	Calculations for the Comparison of Rigid and Specialized Tabs	129
Appendix G	Proposed Test Method for Tensile Properties of Sea Turtle Carapace	131
	G.1 Summary of Method	131
	G.2 Essential Apparatus and Materials	132
	G.3 Coupon Harvesting and Preservation	132
	G.4 Fabrication of Bonded Tabs	134
	G.5 Tensile Test Procedure	136
	G.6 Determination of Tensile Properties	136
	G.7 Report	139
Appendix H	Load-Extension Plots – Synthetic Carapace 1	141
Appendix I	Load-Extension Plots – Synthetic Carapace 2	144
References		149

List of Tables

Table 3.1:	Loggerhead Impact Injury Classification	16
Table 4.1:	Rigid and Specialized Tab Comparison (frame analysis)	27
Table 4.2:	Middle Longitudinal Tensile Test Summary (Carapace 1)	35
Table 4.3:	Middle Transverse Tensile Test Summary (Carapace 1)	36
Table 4.4:	Front Transverse Tensile Test Summary (Carapace 1)	37
Table 4.5:	Front Longitudinal Tensile Test Summary (Carapace 2)	39
Table 4.6:	Front Transverse Tensile Test Summary (Carapace 2)	39
Table 4.7:	Middle Longitudinal Tensile Test Summary (Carapace 2)	40
Table 4.8:	Middle Transverse Tensile Test Summary (Carapace 2)	40
Table 4.9:	Rear Longitudinal Tensile Test Summary (Carapace 2)	40
Table 4.10:	Rear Transverse Tensile Test Summary (Carapace 2)	41
Table 4.11:	Mean Tensile Properties Obtained from Carapace 2	41
Table 4.12:	Comparison of Carapace 1 and 2 Mean Properties	42
Table 4.13:	Middle Longitudinal Flexural Test Summary (Carapace 3)	49
Table 4.14:	Middle Transverse Flexural Test Summary (Carapace 3)	49
Table 4.15:	Front Transverse Flexural Test Summary (Carapace 3)	49
Table 5.1:	Target Tensile Material Properties	61
Table 5.2:	Target Flexural Material Properties	62
Table 6.1:	Matrix Candidate Materials for Prototype Fabrication	63
Table 6.2:	Candidate Fiber Materials for Prototype Fabrication	64
Table 6.3:	Summary of Synthetic Carapace 1 Tensile Testing	73

Table 6.4:	Comparison of Synthetic Carapace 1 Mean Properties and the Target Tensile Properties	74
Table 6.5:	Summary of Synthetic Carapace 2 Longitudinal Tensile Testing	81
Table 6.6:	Summary of Synthetic Carapace 2 Transverse Tensile Testing	82
Table 6.7:	Comparison of Synthetic Carapace 2 Mean Longitudinal Properties and the Target Tensile Properties	82
Table 6.5:	Comparison of Synthetic Carapace 2 Mean Transverse Properties and the Target Tensile Properties	82

List of Figures

Figure 2.1:	Dumbbell Sample Geometry (Burstein et al., 1975)	6
Figure 3.1:	Carapace 3 as Received from the GA DNR	16
Figure 3.2:	Water-Cooled Masonry Saw Utilized in Coupon Harvesting	17
Figure 3.3:	Test Coupon Location and Orientation	18
Figure 3.4:	Typical Test Coupon Harvested from Carapace	19
Figure 4.1:	Free-Body of Sample Secured Through Rigid Tabs	21
Figure 4.2:	Free-Body of Sample Secured Through Specialized Tabs	22
Figure 4.3:	Fabrication of Specialized Tab	23
Figure 4.4:	Typical Test Sample and Cross-Section of Specialized Tabs	24
Figure 4.5:	SAP2000 Model Dimensions	25
Figure 4.6:	Moment Diagram for Rigid Tab Frame Analysis Model	26
Figure 4.7:	Moment Diagram for Specialized Tab Frame Analysis Model	26
Figure 4.8:	Finite Element Model for Stress Evaluation of Alternate Tabs	27
Figure 4.9:	Artificial Members Used to Permit Axial Translation	28
Figure 4.10:	Normal Stress Distribution for Analysis Modeling Rigid Tabs	28
Figure 4.11:	Normal Stress Distribution for Analysis Modeling the Specialized Tabs	29
Figure 4.12:	Tension-Compression Screw-Type Load Device	30
Figure 4.13:	Example of Acceptable Tensile Failure of a Specimen	32
Figure 4.14:	Stress-Strain Curve for Sample ML6 (Carapace 1)	33
Figure 4.15:	Stress-Strain Curve for Sample MT4 (Carapace 1)	34

Figure 4.16: Middle Longitudinal Samples and Orientation (Carapace 1)	35
Figure 4.17: Middle Transverse Samples and Orientation (Carapace 1)	36
Figure 4.18 Front Transverse Samples and Orientation (Carapace 1)	37
Figure 4.19: Unsuccessful Test due to Failure of the Bone Epoxy Interface	38
Figure 4.20: Initial Eccentricity and Transverse Displacement Of a Curved sample Subject to Tension Testing	44
Figure 4.21: Typical Flexure Test	46
Figure 4.22: Load-Deflection Curve for Sample ML4 (Carapace 3)	47
Figure 4.23: Load-Deflection Curve for Sample MT3 (Carapace 3)	48
Figure 4.24: Soft Tissue in Middle Longitudinal Samples (Carapace 3)	50
Figure 5.1: Sample Dimension used to Determine Dimensionless Ratios	52
Figure 5.2: Ultimate Stress versus the Ratio of Gage Length to Thickness (Carapace 2)	53
Figure 5.3: Ultimate Stress versus the Ratio of Gage Length to Width (Carapace 2)	54
Figure 5.4: Ultimate Load versus the Ratio of Thickness to Width (Carapace 2)	54
Figure 5.5: Ultimate Stress versus the Ratio of Thickness to Width (Carapace 2)	55
Figure 5.6: Strain at Failure versus the ratio of Thickness to Width (Carapace 2)	55
Figure 5.7: Strain at Failure versus the ratio of Gage Length to Thickness (Carapace 2)	56
Figure 5.8: Strain at Failure versus the ratio of Gage Length to Width (Carapace 2)	56
Figure 5.9: Modulus versus the ratio of Thickness to Width (Carapace 2)	57

Figure 5.10: Modulus versus the ratio of Gage Length to Thickness (Carapace 2)	57
Figure 5.11: Modulus versus the ratio of Gage Length to Width (Carapace 2)	58
Figure 5.12: Ultimate Stress versus the ratio of Gage Length to Thickness (Carapace 3)	59
Figure 5.13: Ultimate Stress Versus the Ratio of Gage Length to Width (Carapace 3)	59
Figure 5.14: Ultimate Load versus the ratio of Thickness to Width (Carapace 3)	59
Figure 5.15: Ultimate Stress versus the ratio of Thickness to Width (Carapace 3)	60
Figure 6.1: Load-Elongation curve for Single-Ply Polyester / e-Glass Composite Sample	65
Figure 6.2: Initial Condition of the Carapace Employed as the Mold	67
Figure 6.3: Close-Up of Damage to Front Right Quadrant of Shell	67
Figure 6.4: Repair of Mold	68
Figure 6.5: Completed Mold with Surface Leveling	69
Figure 6.6: Synthetic Carapace 1 (top view)	70
Figure 6.7: Comparison of Synthetic Carapace 1 and the Biological Mold	71
Figure 6.8: Underside of Synthetic Carapace 1	72
Figure 6.9: Load-Extension Curve for Sample 3, Synthetic Carapace 1	73
Figure 6.10: Synthetic Carapace 2 Fabrication Process	75
Figure 6.11: Synthetic Carapace 2 Fully Cured and Removed from Mold	76
Figure 6.12: Synthetic Carapace 2 with Addition of Faux Ribs	77
Figure 6.13: Completed Synthetic Carapace 2	78
Figure 6.14: Comparison of the Underside of the Natural and Synthetic Shell	78

Figure 6.15:	Tensile Testing of Synthetic Carapace 2 Coupons	79
Figure 6.16:	Load-Extension curve for Longitudinal Sample 4, Synthetic Carapace 2	80
Figure 6.17:	Load-Extension Curve for Transverse Sample 1, Synthetic Carapace 2	81

Nomenclature

A	cross-sectional area of coupon
b	width of coupon
d	depth of coupon
δ_f	cross head extension at failure
δ_i	cross head extension at the i th data point
Δ_t	transverse displacement at the time ultimate load is achieved
e	initial eccentricity of tensile loading
E^p	pseudo tensile modulus of elasticity
ε_f^p	pseudo strain at failure
ε_i	pseudo strain at the i th data point
ε_{i+n}	pseudo strain at the i th plus n data point
F_{ult}^p	pseudo ultimate tensile strength
F_{UW}	ultimate force per unit width
I	moment of inertia
L_o	initial gage length of sample
M	bending moment
P	tensile load
P_i	tensile load at the i th data point
P_{ult}	ultimate tensile load
σ	tensile stress

σ_i	pseudo tensile stress at the <i>ith</i> data point
σ_{i+n}	pseudo tensile stress at the <i>ith</i> plus <i>n</i> data point
σ_{ult}	ultimate tensile strength
y	distance from the centroid of the coupon cross-section

Summary

The research presented in this study has been conducted in an effort to aid in the creation of a biomimetic shell that may be employed in full-scale field experiments to determine the efficacy of mitigation options to limit loggerhead mortality in boat strike incidents. The objectives of this research include the development of experimental testing procedures for the material characterization of the loggerhead carapace, and the design, fabrication, and evaluation of an artificial prototype carapace.

A photographic database of wounded sea turtles in Georgia was evaluated in order to determine the primary sources of loggerhead collision injuries and the most common regions of the carapace damaged in boat strike incidents. Skeg impact was found to be the most common source of injury, with a frequency of 44%. In addition, 74% of the sea turtles reviewed sustained injuries to the center third of their carapace length, indicating this region as the most probable impact location.

Material testing procedures were developed for evaluating the material properties of the loggerhead carapace. This was followed by the material testing of three loggerhead shells for the purpose of determining localized mechanical properties. Samples were harvested from the shells in a manner designed to identify potential variations in properties due the location and orientation of the coupons within the carapace. Each coupon was subjected to axial tension or three-point bending. Specialized tabs were designed for tension testing in order to accommodate the coupon's irregular geometry and minimize curvature-induced moments. The tensile test results indicated that the longitudinal and transverse properties of the loggerhead carapace were similar. The

tensile strength, elongation at failure, and modulus of elasticity were determined to have percent variations of 12.2%, 10.7%, and 10.1% respectively. In contrast, the three-point bending test results indicated that the modulus of rupture and flexural modulus for the transverse samples were approximately four times greater than those of the longitudinal samples. This variation may be attributed to regions of weak tissue running transversely through the carapace.

The results of the material testing were utilized in the design of two prototype composite shells. The prototypes were successful in simulating the strain at failure and force per unit width to within 10% of the loggerhead carapace. The resulting procedure may be used to create artificial shells suitable for prototype scale tests in natural environments. In addition, the material testing methods developed for this investigation may offer insight into procedures for evaluating alternate forms of rigid or curved biological specimens.

Chapter 1

Introduction

Loggerhead sea turtles (*Caretta caretta*) are highly migratory and inhabit coastal estuarine and continental shelf waters in subtropical and tropical areas around the world. They have been observed as far north as Newfoundland and as far south as Argentina (Plotkin 1995). The primary populations in the United States can be found between North Carolina and Florida, with smaller populations located in the U.S. Gulf of Mexico (USFWS 1978). The adults have a rust-colored carapace with an average length of 92 cm and a typical weight of 113 kg (Plotkin 1995). The loggerhead reproduces by laying eggs in nests on beaches (Ernst et al. 1994). During nesting time there is significant potential for interaction between the turtles and humans.

The loggerhead was classified as an endangered species and placed on the International Union for Conservation of Nature and Natural Resources (IUCN) Red List in 1996 (IUCN 2006). The species was initially listed as threatened within the United States by the U.S. Fish and Wildlife Service in 1978 (USFWS 1978). This status was reviewed and maintained in 2007, listing bottom trawling, dredging, incidental capture (bycatch), marine pollution, entanglement in marine debris, and climate change as threats affecting the loggerhead in oceanic zones. It was also noted that the percentage of recovered dead loggerheads exhibiting propeller and collision injuries from boats and ships had risen from approximately 10% in the 1980's to a record high of 20.5% in 2004 (USFWS 2007). It has been estimated that vessel strikes account for 50 – 500 mortalities per year within the U.S. (Plotkin 1995). Many vessel strikes have been documented in

southeast Florida, with as many as 60% of stranded loggerheads displaying signs of propeller-related injuries (USFWS 2007). Furthermore, a large fraction of sea turtle fatalities in Georgia have been attributed to impacts of boats and boat propellers (Dodd 2006).

There have been few studies that focus directly on the interaction between marine vessels and sea turtles. Much of the previous research on loggerheads addresses growth rates, behavior, and population distributions. However, Venizelos (1993) in the Mediterranean and Hazel (2006) in Australia studied the significance of boat and sea turtle interactions. The Georgia Department of Natural Resources (GA DNR) has been asked to comment on the potential for loggerhead mortality rates to rise as a result of increases in marine traffic and structural development on the coast. At present, there is only limited empirical and statistical evidence on which to base a response. This fact served as the motivation for the work described herein, which is designed to investigate the mechanical properties of the loggerhead carapace and develop an artificial prototype carapace.

The following tasks outline the requirements for completion of the material characterization of the loggerhead carapace and the development of an effective prototype biomimetic shell.

- 1) Define the physical parameters governing failure of natural turtle shells, considering the material as a deformable solid. This includes a review of previously developed testing protocols for other natural organic materials, such as bones, shell, and cartilage.

- 2) Classify the primary sources and impact locations of sea turtle injuries associated with boat collision incidents, to the extent possible, based on inspection of photographs of wounded turtles, in order to design the testing program.
- 3) Quantitatively describe loggerhead sea turtle physical characteristics, including size, shape, flexural strength and tensile strength.
- 4) Select materials for the construction of artificial turtle shells. Use quantitative, empirical evaluation parameters to select the most appropriate material system.
- 5) Design and build a prototype turtle shell with chosen material(s) and configuration.
- 6) Design an evaluation procedure to ensure that the mechanical behavior of the artificial shell is representative of the behavior of the natural shell.
- 7) Refine the production methodology to allow fabrication of multiple shells for field experiments.

Chapter 2

Previous Work

Research focusing on the material characterization of the loggerhead sea turtle (*Caretta caretta*) carapace does not exist in the current body of literature. However, extensive studies have been conducted on other biological materials such as human and animal bones. This research offers insight into applicable test procedures and data interpretation. Reviewed in the current study are a number of works pertaining to bone preservation techniques, biomechanical testing of related materials, and the simulation of relevant biological materials. In addition, publications considering the significance of vessel strikes on sea turtle mortality rates have been included.

2.1 Carapace Composition

The loggerhead carapace is an exoskeletal bone and a viscoelastic composite material. Bone is primarily composed of mineral (hydroxyapatite, approximately 2/3 dry weight), fibrous collagen (1/3 dry weight), and water. Collagen is the principal structural protein and directly affects the mechanical properties of the material (Puxkandl 2002). However, the two most significant characteristics are the degree of porosity and mineralization. Specifically, variations in mineralization significantly impact the elastic modulus of bone, which can range from 4 to 32 GPa. Intuitively, a larger volume fraction of pores results in a lower modulus value (Currey 1984).

2.2 Review of Coupon Harvesting and Preservation Techniques

Preservation of biological samples is critical for obtaining results that accurately reflect the properties of living bone. For instance, unpreserved human bone samples exhibit a 3% decrease in modulus of elasticity after 24 hours (An and Draughn 2000). Storage techniques that have proven successful include the placement of small specimens in a solution of 50% saline solution and 50% alcohol at room temperature for time periods of up to three months. For long-term preservation, samples should be frozen and kept as hydrated as possible (An and Draughn 2000). Alternatively, physiological saline, a sterile solution of sodium chloride, is frequently employed independently to aid in conserving material properties. For example, Burstein et al. (1976) evaluated the mechanical properties of machined human cortical bone specimens and required the samples to be preserved during transport. The bone segments were wrapped in cloth, saturated with physiological saline, covered in plastic, and encased in dry ice.

Bone can be cut using a band saw or circular saw. However, care must be taken to avoid burning the sample which can dramatically affect the mechanical properties (An and Draughn 2000). In many cases milling or shaping is required to form a test coupon. Burstein et al. (1976) formed femoral and tibial specimens into square cross-section bars and dumbbells using a high speed milling device. A water jet was used to mitigate burn damage on the samples. The dimensions of the dumbbell samples are given in Figure 2.1.

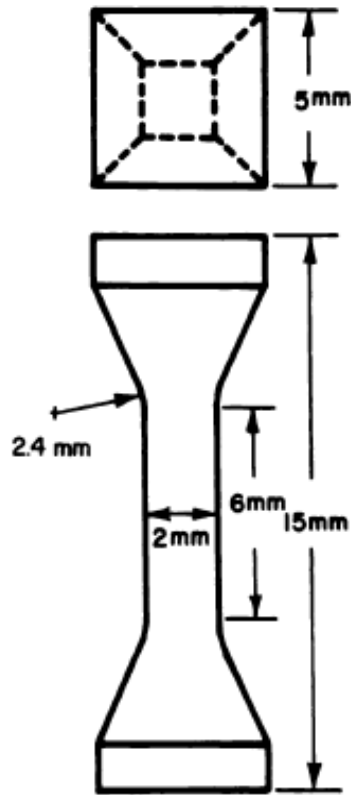


Figure 2.1: Dumbbell Sample Geometry (Burstein et al., 1975)

2.3 Review of Biological Material Testing Procedures

The number of variables associated with biological testing is significantly increased when compared to traditional engineering materials. Biological materials are frequently nonhomogeneous due to their composition of both collagen and elastin fibers; in addition, factors such as age, diet, and lifestyle can affect the mechanical characteristics of the material (Karchin 2004). Many of the procedures and ideologies associated with the characterization of traditional construction or manufacturing materials may not be directly applicable when testing organic samples. The material properties should be tested in multiple orientations in order to evaluate the planes of symmetry (transversely isotropic / orthotropic) (An and Draughn 2000). Testing samples in tension adds an

additional level of complexity when compared to procedures for evaluating flexural properties. During testing, organic tissue will frequently slip in the grips of the test fixture resulting in inaccurate strain and modulus values (Milthorpe et al. 1987). Specimens are often potted in bone cement (Polymethylmethacrylate, often referred to as PMMA) in order to obtain a reliable grip interface and prevent sample damage. PMMA mechanically bonds to bone by penetrating the pores on the bone surface and is also frequently employed to adhere implants to biological tissue in living organisms (Wang et al. 1996).

Many studies focused on the effects of aging on the tensile properties of human bone. For example, Burstein et al. (1976) conducted testing on thirty-three femoral and tibial tissue samples obtained from a human population ranging in age from twenty-one to eighty-six. It was found that the ultimate tensile strength and elongation at failure of the femoral tissue both decreased with age. This is in contrast to the majority of engineering materials which become increasingly brittle as tensile strength is increased. This study also found that the mechanical properties of the tibial bone tissue were significantly higher than the corresponding properties of the femoral tissue. The author noted that this phenomenon may be attributed to sample variation at the structural or organ level where bone development is influenced by alternate loading conditions during the life of the individual.

Currey (1984) conducted tensile and flexural testing on red deer antler, crocodile skull bone, Galapagos tortoise femur, muntjac antler, cow femur, and fin whale tympanic bulla samples in order to evaluate the effects of variations in mineralization on the mechanical properties of bone. The author noted two factors that question the validity of

the tests for modeling real world behavior. The first considers the fact that the samples are loaded at low displacement rates resulting in force induced failure. However, in many situations bone breaks due to the absorption of an overwhelming quantity of kinetic energy resulting from impact. The second factor considers the imperfections associated with bone geometry in real life that are not present in carefully prepared samples. These imperfections will frequently define the location at which a crack will start and propagate. This is highly significant when employing “fracture mechanics” principles to evaluate sample failure.

Wang et al. (1996) conducted a study focusing on the effects of specimen configuration on push-out, tensile, and compact sandwich (CS) fracture toughness tests designed to evaluate the strength of the tissue-implant interface. The strength of this interface is vital for total joint prosthesis as it is a common location for prosthesis failure. The author found it was necessary to create identical interfaces among samples in order to ensure equivalent molding conditions for the bone cement. The samples were fashioned into the desired geometry using a bench-top milling machine under constant irrigation. In order to prevent moisture from decreasing the interface strength, the bone coupons were allowed to dry at 23 °C prior to bonding with PMMA. Various specimen configurations were employed for each of the three types of tests. The test results did not indicate any statistically significant differences between the results of the various CS configurations. However, there was a difference of approximately 300% and 500% for the push-out and tensile test configurations, respectively.

Wang et al. (2001) conducted three-point bending tests on 6 human cadaveric femurs in order to evaluate the role of collagen in determining bone mechanical properties. The

bone samples were preserved in a freezer prior to test preparation. A diamond saw and bench-top milling machine were used to form the samples into 30 mm x 4 mm x 2mm bar shapes. The samples were then heat treated different temperatures in order to induce collagen denaturation at dissimilar levels. Each bone coupon was subjected to flexural testing with a span length of 16 mm at a deflection rate of 5 mm/min. The author determined the elastic modulus, ultimate yield strength, and work to fracture for each sample tested. The results of the study indicated that increased volume fractions of denatured collagen decreased the strength and work to fracture of bone. In contrast, variations in denatured collagen did not alter the elastic modulus of the samples.

Marine vessel-related injuries have accounted for 24% of all Florida manatee (*Trichechus manatus latirostris*) deaths from 1974 to 2006 (Clifton et al. 2007). This fact served as the motivation for multiple studies addressing potential mitigation options and demonstrated the need to quantify the biomechanical effects of boat strikes on manatees. Clifton et al. (2007) conducted three-point flexural tests on manatee rib samples in order to evaluate the bending strength, elastic modulus, and fracture toughness of the bone. The coupons were machined into the desired geometry using a band saw under constant water spray. The three-point flexural testing was conducted in accordance with ASTM standard D790M-92 for flexural testing of plastics. The bending strength, elastic modulus and fracture toughness were found to range from 61 – 160 MPa, 4 – 18 GPa, and 1.4 – 2.9 MPa m^{1/2} respectively.

2.4 Review of Methods for Developing Biomimetic materials

In recent years, researchers working on the development of new materials have begun looking to nature for inspiration. Many studies focus on understanding the mechanisms that promote the favorable characteristics of biological materials in an effort to incorporate the attributes into synthetic material design. For example, bone, sponge spicules, and shells have been considered as models for synthetic structural composites due to their ability to maximize multiple properties, such as strength, elastic modulus, and toughness (Mayer 2005). The field of study that focuses on the simulation of natural structural models and systems in order to solve human problems is known as biomimetics.

Many efforts have been made to mimic biological materials on the chemical or molecular level. However, other studies have placed an emphasis on understanding the macromechanical behavior of organic materials from more traditional relationships. Much of the evolution of a biological material structure is guided through mechanical contact with its environment. Therefore, when designing a biomimetic structure, it is necessary to quantify the mechanical behavior of the organic material being simulated with respect to the natural structure-property relationship (Bruck et al. 2002).

Studies have been conducted that examine plant structures in order to advance synthetic composite design strategies. Li et al. (1995) considered the development of biomimetic materials modeled after bamboo due to the relative high strength-to-weight ratio of the plant. Bamboo fibers are comprised of multiple concentric layers with alternating thickness. Each layer contains parallel microfibrils. The orientation of the microfibrils is dependent upon the layer at which they are located. In correlation with

these characteristics, four types of synthetic specimens were designed and fabricated in order to evaluate their individual mechanical properties. The samples were constructed of a glass fiber-reinforced epoxy resin with either single or double-helical fiber orientations. In addition, hollow and solid axial fiber reinforced specimens were manufactured. Each specimen type was subjected to axial compression, flexure, and tension testing. The findings indicated that the double-helical structure possessed the optimum mechanical properties and offers an ideal model for constructing engineering composite materials.

Garita and Rapoff (2003) conducted an investigation of the structural behavior of human bone under static and cyclic loading in order to utilize the findings to determine structurally optimizing geometry that integrates ideal mechanical properties at minimum weight. The author discovered spatial variation near the foramen (a natural hole in bone) that was hypothesized to force stress concentrations away from the edge of the material and into a region that possesses superior strength and toughness. A finite element model (FEM) of the bone was constructed using comparison based properties. The model was validated through the development of a biomimetic sample to be employed in mechanical testing. The resulting design was a “dog bone” polyurethane foam plate containing a circular hole at its center. The foramen and adjacent tissue were simulated by surrounding the hole with rings of varying densities. The biomimetic plate was subjected to tensile testing and displayed approximately twice the strength of a homogeneous plate exposed to identical loading conditions. Similarly, the sample with varying density was found to have increased toughness when compared to the homogeneous specimen under cyclic loading. The study suggests that the foramen and adjacent tissue with spatial

variation are structurally optimizing features that can be simulated in discontinuous synthetic materials to increase strength and toughness by mitigating stress concentrations.

Mayer et al. (2005) studied the mechanisms that contribute to the elevated toughness values associated with mollusk shells. In addition, a simplified biomimetic composite was developed based on the structure of the shell. The structure of the mollusk shell resembled a brick and mortar system composed of a ceramic phase, with a high volume fraction, encased in a matrix of viscoelastic proteins and other organic material. Multiple macro-scale biomimetic composite beams were constructed and subjected to mechanical testing. Each beam was comprised of a ceramic/organic segmented material encased in thin layers of organic adhesive. The thickness of the organic adhesive was varied for each sample. The arrangement of the constituents mimicked the brick and mortar stacking sequence observed in the natural shell. Mechanical testing of the synthetic beam yielded an increased understanding of the critical level at which the matrix layers offer optimum energy dissipation.

Other investigations have focused on the benefits of biological systems employed as models for large-scale structures. Yiatros (2007) considered integrating biological principles into the design of complete systems. Multiple examples of large structures that unintentionally imitate geometry observed in nature were listed. Examples of this include suspension bridges that share many of the same structural principles as spider webs and the multidimensional curvature of a sea shell that can be observed in the geometry of the Pantheon in Rome. In addition, it was noted that membrane structures, such as modern stadia roofs and canopies, behave similar to cell walls by gaining strength and stability through remaining in constant tension. The author suggests employing a

tree trunk as the ideal model for a multi-story load bearing duct. Due to the longitudinally aligned fibers, the trunk proficiently resists axial compression and flexural forces due to gravity and wind loads. This model also contributes to the development of advanced energy efficient design features. Examples of this include the implementation of natural heat-induced air flow for superior ventilation at minimal energy cost.

2.5 Significance of Vessel Strikes on Sea Turtle Mortality Rates

Venizelos (1993) requested a reduction in the number of speed boats permitted in the Laganas Bay after the discovery of eight deceased loggerhead turtles within a two month period. The deaths were attributed to multiple carapace fractures caused by speed boat impacts. The author noted that only a fraction of the sea turtles killed by boat collisions are recovered and expressed concern regarding the detrimental effects of marine congestion on the implementation of protection measures.

Hazel (2006) reviewed sea turtle stranding records in Queensland, Australia in order to assess the significance of vessel strikes on turtle mortality rates. It was found that a minimum of sixty-five turtles were killed annually as a result of boat collisions on the Queensland east coast. This was considered to be comparable to the mortality rate attributed to trawl fishing prior to the introduction of mandatory turtle-exclusion devices. The majority of the mortalities involved green and loggerhead turtles with 72% of cases involving adults or subadults. This study indicated that vessel strikes should be considered in conservation planning and in the development of threat mitigation programs.

Hazel et al. (2007) conducted an additional study designed to evaluate the behavioral response of green turtles to marine vessel approaching at various speeds in shallow water. Data was recorded for 1890 observations sighted within 10 m of the research vessel. The findings indicated that the proportion of turtles actively attempting to avoid the vessel decreased as speeds were increased. The author noted that boat operators, traveling at speeds that exceed 4 km/h cannot rely on the green turtles to avoid impact. The results of this investigation suggest that mandatory speed restrictions will aid in green turtle mortality mitigation by reducing collision incidents.

Chapter 3

Coupon Harvesting and Preservation

This chapter discusses coupon harvesting procedures and sample preservation techniques. In addition, the primary modes of loggerhead injury were classified in order to identify critical locations for coupon harvesting. This information aided in the development of a harvesting procedure designed to evaluate the properties' dependence on sample location and orientation. Preservation techniques were employed to prevent deterioration of the samples prior to axial tension or flexural testing.

3.1 Classification of Loggerhead Injuries

Photographs of 110 deceased loggerhead sea turtles, discovered between 2001 and 2006 in Georgia, were obtained from the Georgia Department of Natural Resources. Each animal was photographed from multiple angles at the location at which it was recovered. The photographs were converted into a database categorizing the impact location and likely cause of damage. The sources of injury considered included skeg, propeller, blunt object, and indeterminate impact damage. Damage location was categorized into four regions: the front, center, and rear third of the carapace, along with the carapace rim. The data were then used to determine the frequency of specific fatal injuries sustained by loggerhead sea turtles occurring off the Georgia coast. The results are listed in Table 3.1 and indicate that skeg impact to the center of the carapace is the most common type of fatal injury. This fact aided in selecting critical locations for coupon harvesting and the determination of target properties. It should be noted that many specimens exhibited characteristics of multiple classifications of source and/or

location of injury and each was recorded. This resulted in category summations exceeding 100%.

Table 3.1: Loggerhead Impact Injury Classification

Source of Injury (%)		Location of Injury (%)	
Skeg	44%	Front of Carapace	45%
Propeller	13%	Back of Carapace	45%
Blunt Object	11%	Center of Carapace	74%
Indeterminate	42%	Carapace Rim	55%

3.2 Coupon Harvesting

The Georgia Department of Natural Resources provided three carapaces for the purpose of determining localized mechanical properties of the loggerhead shell. Figure 3.1 displays one of the cleaned carapaces with propeller injuries located on the front left quadrant. Section 3.3 will address the condition of each shell and the nature at which they were obtained in further detail.



Figure 3.1: Carapace 3 as Received from the GA DNR

A masonry saw with a water-cooled blade was employed for coupon harvesting (Figure 3.2). Constant irrigation was used to mitigate burn damage as this may significantly affect the measured material properties (An and Draughn 2000).



Figure 3.2: Water-Cooled Masonry Saw Utilized in Coupon Harvesting

In order to determine any variation in tensile properties associated with the sample location within a carapace, each shell was divided into six distinct regions. This was accomplished by first bisecting the carapace along the spine. The two halves of the shell were then cut into three segments of equal length orthogonal to the spinal column. The resulting six regions are depicted in Figure 3.3.

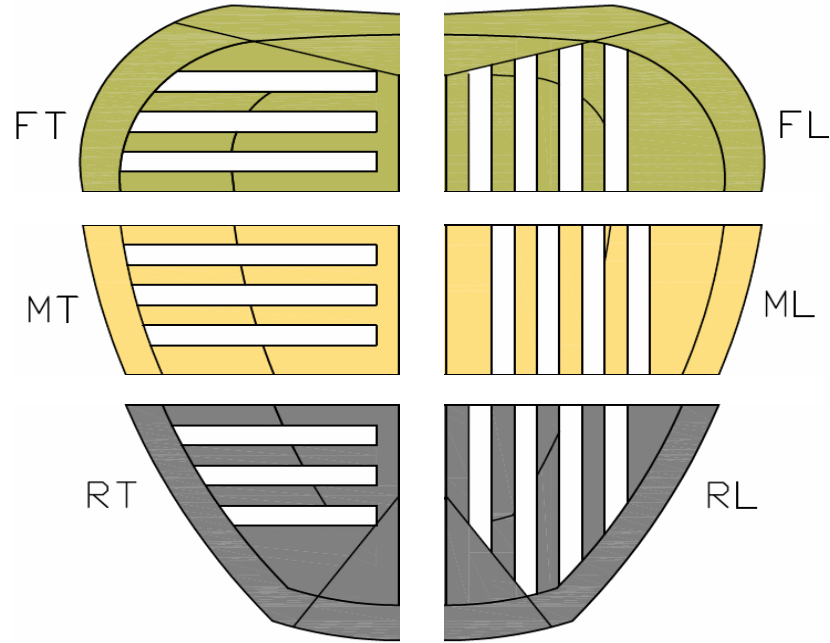


Figure 3.3: Test Coupon Location and Orientation

Each region with designation (*T*) was cut into approximately 2.5 cm wide coupons with the gage length transverse to the spine. Similarly, the regions with designation (*L*) were harvested into approximately 2.5 cm wide samples with gage length longitudinal to the spine. The sample location and orientation is illustrated by the white, rectangular spaces in Figure 3.3. It should be noted that the depiction has been modified for clarity and does not accurately quantify the number of specimens obtained from each region or the size of the sample relative to the intact carapace. The designations (*F*), (*M*), and (*R*), denote the front, middle, and rear respectively. The numerical value following the alphabetic designation (e.g. MT2) corresponds to the location of the sample within the region previously specified. A typical sample is shown in Figure 3.4.



Figure 3.4: Typical Test Coupon Harvested from Carapace

Approximately seven samples were obtained from each region. The average length and thickness of the coupons were 10.7 cm and 1.05 cm respectively. However, the geometry of each sample varied and was dependent upon the region of the carapace from which it was harvested. The gage length, thickness, and width of each sample are listed in Appendix E.

3.3 Preservation Methodology

The first carapace studied in this investigation, designated Carapace 1, was stored in a temperature controlled environment, at 20-25 °C, for approximately 6 months before coupons were harvested from the shell. The second loggerhead was euthanized by the Georgia Department of Natural Resources due to injuries sustained by vessel impact. This carapace (Carapace 2) was cleaned prior to transport. Once received, coupons were harvested immediately. Sample preservation was performed by individually wrapping the coupons in gauze before saturating the bone in a solution of 50% alcohol and 50% saline solution. These specimens were then placed in airtight bags and frozen until the test date. Carapace 3 was cleaned by the Georgia Department of Natural Resources and frozen for approximately one month before transport. The coupons did not require preservation when received as they were immediately harvested and tested.

Chapter 4

Development of Test Procedures and Data Collection

Early testing indicated that specialized tabs would be required for tensile testing due to the samples' curvature and sensitivity to damage from the grips. Tension-induced elongation causes sample ends to rotate as the curvature of the specimen decreases. Resistance to this rotation introduces fixed-end moments at the grips. Therefore, tensile loading of curved samples adhered to traditional rigid tabs, comprised of bone cement or fiberglass, induces moments by resisting the straightening of the curved coupon. The fixed-end moments increased the axial stresses resulting in premature failure of the sample at the grips. It should be noted that rupture occurs adjacent to the tab. Figure 4.1 illustrates the condition of a curved sample at the initiation of loading secured through rigid tabs and displays a free-body diagram of the deformed shape as the axial displacement is increased. The forces labeled (P) denote the applied load and the value of the vertical reaction at the static lower grip. The designation (M) refers to the moments developed at the grips as they resist rotation.

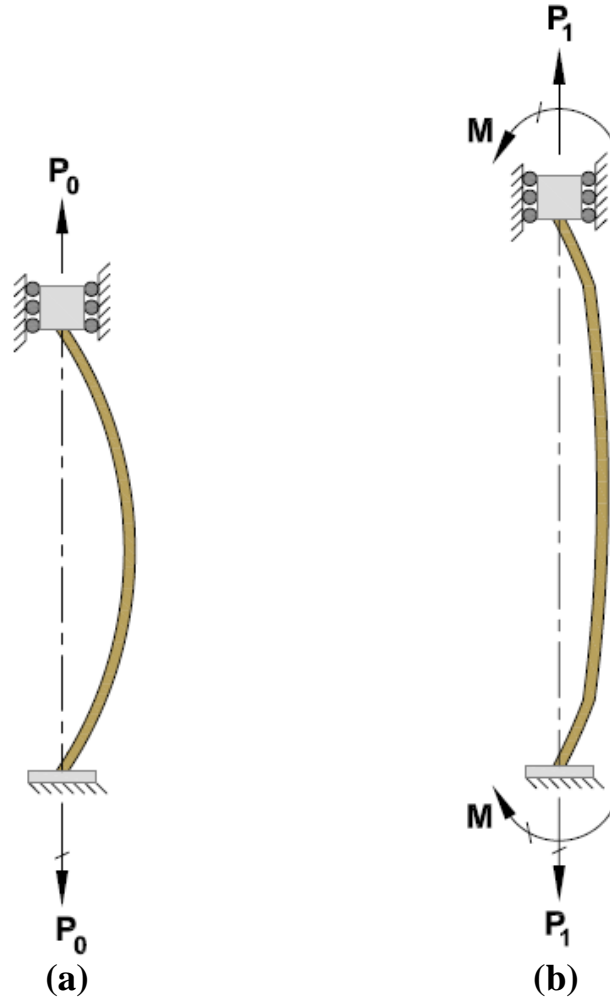


Figure 4.1: Free-body of Sample Secured through Rigid Tabs
 (a) Loading at initiation of test. (b) The deformed shape as axial displacement is increased.

4.1 Specialized Tab Design

In order to remove the fixed-end moments, it was necessary to develop specialized tabs that behaved as simple pin supports. The initial condition of a sample secured through pinned connections is shown in Figure 4.2 along with a free-body diagram of the deformed shape as the axial displacement is increased. It should be observed that the fixed-end moments are minimized as the restraints allow for rotation at the grips.

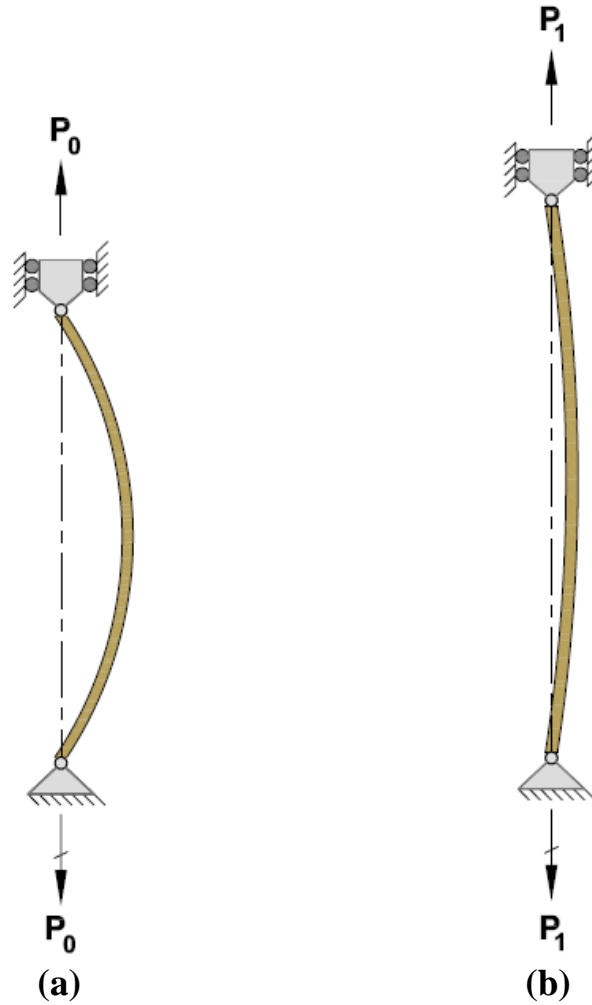


Figure 4.2: Free-body of Sample Secured through Specialized Tabs
(a) Loading at initiation of test. (b) The deformed shape as axial displacement is increased.

Numerous configurations of epoxy and steel tabs were tested prior to finalizing the tab design. The specialized tabs are constructed of a thin metal plate protruding from a short section of PVC pipe that is capped and filled with epoxy. A commercially available plumbers putty is employed to contain the epoxy within the PVC cap prior to solidification. The steel tab is formed into a hook at the end encased in epoxy in order to prevent pull-out failure. Prior to the epoxy curing, the tab is positioned on the samples and the resin is permitted to solidify for twenty-four hours. This process securely bonds

the coupon to the tab preventing any slipping at the carapace-epoxy interface. The low resistance to bending associated with the steel tab allows for rotation at the grips. As a result, the coupon may be modeled as simply supported. One sample being prepared is shown in Figure 4.3. The rubber pipe coupler and clamps are employed to support the tab and coupon while the epoxy is curing. Further details addressing the fabrication of the bonded tabs are provided in Appendix G.

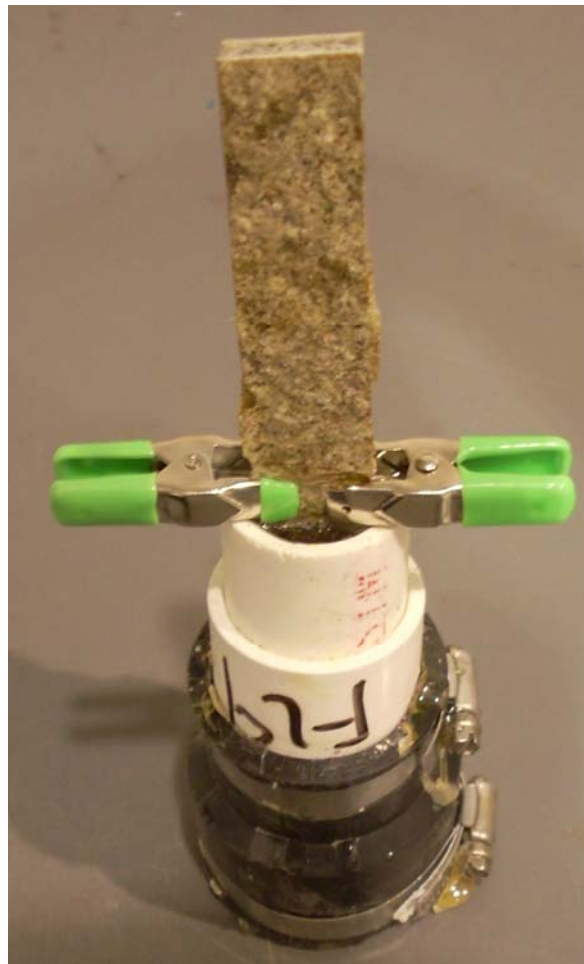


Figure 4.3: Fabrication of Specialized Tab

Figure 4.4 shows a completed sample being tested and a cross-section of the specialized tabs. In addition to mitigating the fixed-end moments, the specialized tabs

also aid in damage prevention by gripping the specimen through adhesion and mechanical bonding rather than clamping force.

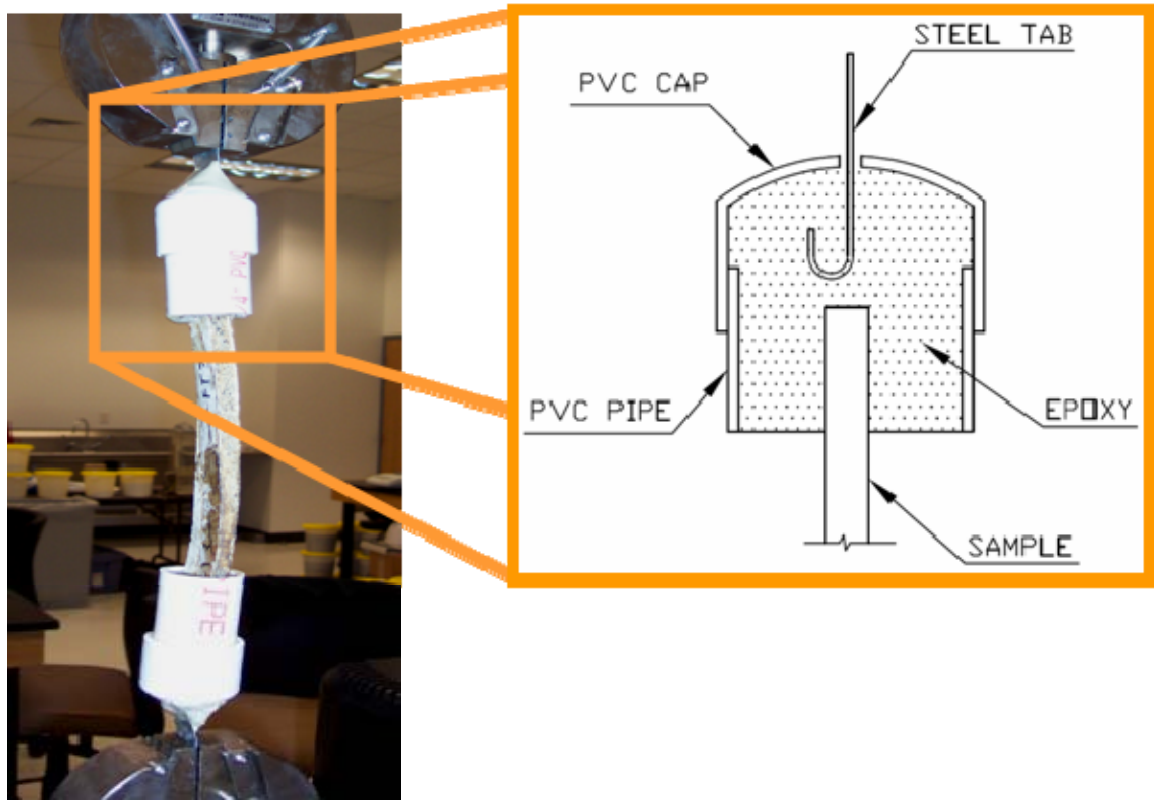


Figure 4.4: Typical Tension Test Sample and Cross-Section of Specialized Tabs

4.2 Comparison of Rigid and Specialized Tabs

The advantages of the specialized tabs were evaluated through frame and finite element analyses created to model the geometry and material properties of one of the coupons (Carapace 2, FT3). The significant curvature associated with the specimen made it ideal for this investigation. The sample was tested in axial tension utilizing the specialized tabs and a stress-strain curve was generated. The stress-strain data were input into SAP2000 and used to determine the material properties of the sample. Two frame

analysis models were then created. The geometry of the member was simplified to a prismatic section with a thickness equal to the minimum thickness of the sample being modeled. The specific dimensions are given in Figure 4.5.

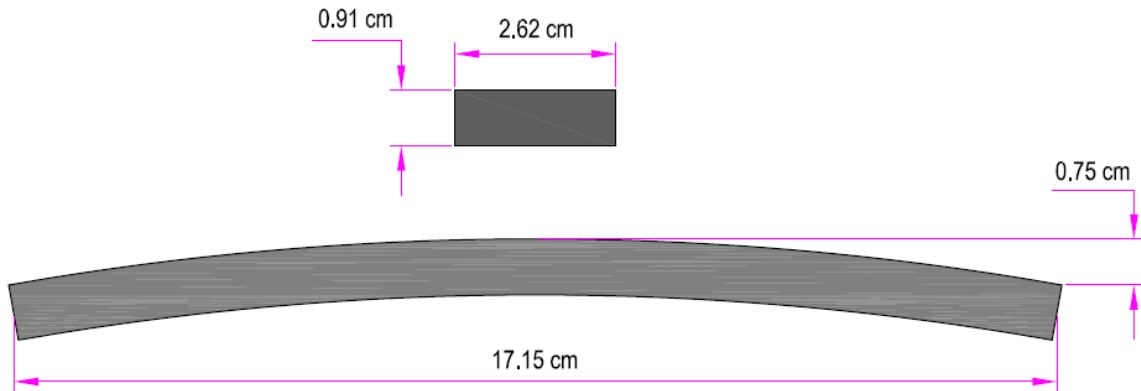


Figure 4.5: SAP2000 Model Dimensions
Top: Cross-sectional dimensions. Bottom: Span-length and curvature

The first frame model was designed to simulate the behavior of the sample secured through traditional rigid tabs. This was accomplished by applying a fixed support to one end of the member. The alternate end, at which the axial load was applied, possessed fixities preventing rotation and vertical translation. However, axial extension was permitted. A 768 N load was then placed on the model, which represents the ultimate force exhibited by sample FT3 during the experimental testing. A nonlinear plane frame analysis was conducted and the resulting moment diagram is displayed in Figure 4.6. The moment diagram clearly shows significant fixed-end moments induced by the rigid tabs. This would reduce the accuracy of properties determined from the axial tension test by increasing the normal stress within the coupon and inducing premature failure.

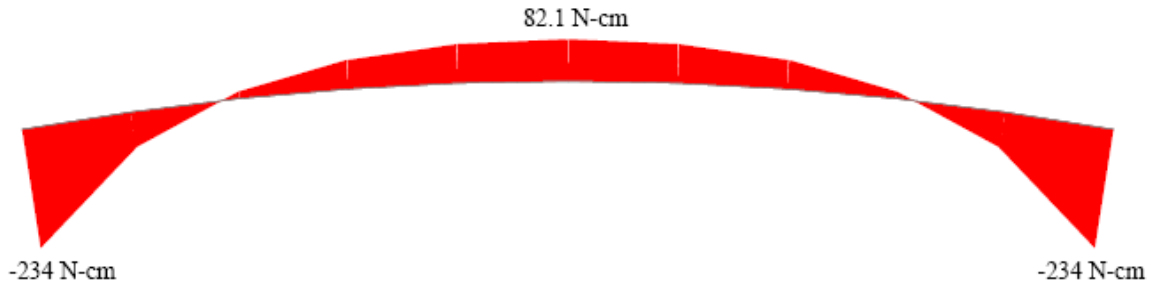


Figure 4.6: Moment Diagram for Rigid Tab Frame Analysis Model

The second frame model was constructed to simulate the behavior of the coupon secured by the specialized tabs. This was accomplished by simply supporting the coupon and applying the 768 N load at the end permitting translation. A nonlinear plane frame analysis was conducted and the resulting moment diagram is displayed in Figure 4.7.

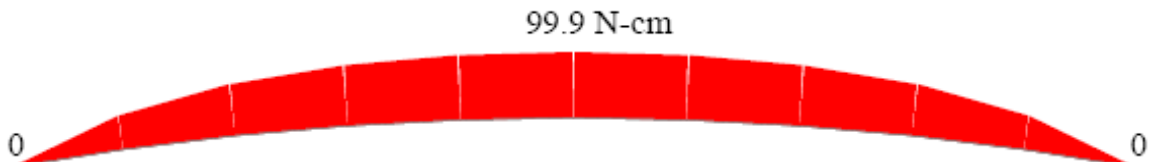


Figure 4.7: Moment Diagram for Specialized Tab Frame Analysis Model

The results of the frame analyses were used to compute the values in Table 4.1, which compares the maximum bending moment and ultimate stress found for the rigid and specialized tabs. The calculations used to generate these values are given in Appendix F. The findings indicate that the specialized tabs offer significant benefits when subjecting curved samples to axial tension testing by reducing the ultimate stress and maximum bending moment.

Table 4.1: Rigid and Specialized Tab Comparison (frame analysis)

Tab Modeled	Maximum Bending Moment (N-cm)	Ultimate Stress (kPa)	% Stress due to Bending
Traditional Rigid Tab	234	9600	67%
Specialized Tab	99.9	5980	46%
% Difference	80.3%	46.5%	37%

As previously mentioned, two finite element models were also constructed to simulate coupon FT3 (Carapace 2) secured through restraints modeling the alternate tabs. The finite element analyses were performed to aid in understanding how the alternate tabs effect the normal stress distribution throughout the coupon. The model developed for the analysis is shown in Figure 4.8 and has dimensions equivalent to those given in Figure 4.5. As with the frame analysis, the stress-strain curve obtained from the tensile testing of sample FT3 was used to define the material properties of the elements.

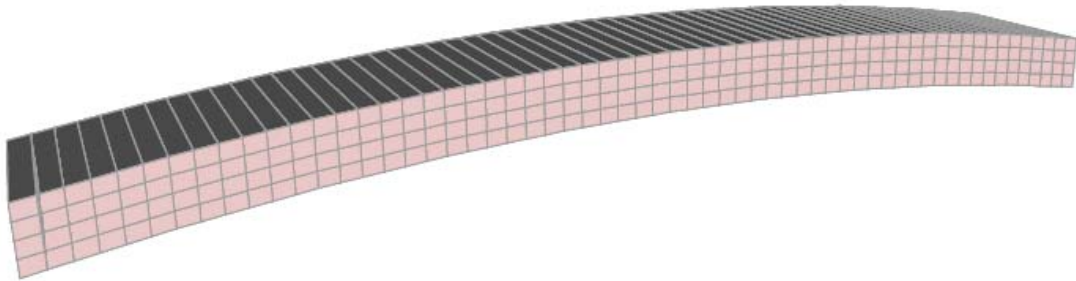


Figure 4.8: Finite Element Model for Stress Evaluation of Alternate Tabs

The models for the rigid and specialized tabs are identical with the exception of the fixities at either end. The rigid model has vertical and lateral translation prevented at the center node along the depth. The two nodes above and below this point have fixities

preventing only lateral translation. These supports prevent rotation at the end and therefore perform as a fixed support. Artificial members were employed for the end of the coupon allowing translation. These members possess near infinite stiffness relative to that of the coupon. In effect, all deformation that takes place may be attributed to the carapace sample. The artificial members are subject to continuous constraints where they connect with the finite element mesh. At the location at which the members intersect all degrees of freedom are restrained with the exception of axial translation. The artificial members are displayed in Figure 4.9 on the right side of the coupon.



Figure 4.9: Artificial Members used to Permit Axial Translation

The 768 N load is distributed over the end of the coupon, permitting translation with the center three nodes loaded with 192 N and the outer two subjected to 96 N. The normal stress distribution resulting from the nonlinear analysis is displayed as a contour plot in Figure 4.10.

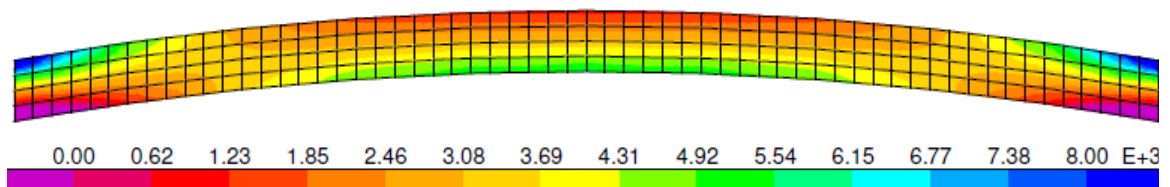


Figure 4.10: Normal Stress Distribution for Rigid Tab Analysis Model (Units: kPa)

The scale in the preceding figure is set to a maximum of 8000 kPa in order to clearly view the stress distribution, although stresses as high as 10800 kPa were observed at the upper corners of the coupon.

The model developed to simulate the specialized tabs was similar to that utilized in the previous analysis with the exception of the fixities. The member was simply supported with the loads applied at the end permitting lateral translation. The pin and roller supports were located at the center node along the ends of the member. The 768 N load was distributed among the end nodes in the manner described for the rigid tab model. The normal stress contour plot generated from the nonlinear finite element analysis is displayed in Figure 4.11.

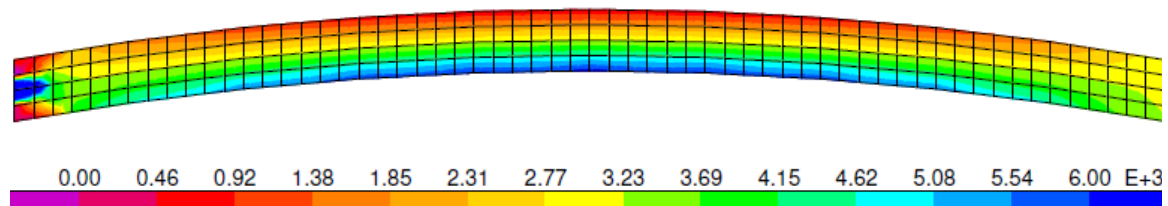


Figure 4.11: Normal Stress Distribution for Specialized Tab Analysis Model (Units: kPa)

The maximum stress was found to be 6100 kPa located along the bottom of the sample at span midpoint. This was relatively consistent with the 5980 kPa found for the frame analysis. However, the stress concentration located at mid-height of the left end was neglected since it can be attributed to the axial load being resisted by the pin fixity. The specialized tab secures the full depth of the sample preventing this stress concentration from forming.

The analysis models suggest that the specialized tabs allow for rotation and subsequently permit the sample to become more linear under loading. The specialized

tabs theoretically remove the fixed-end moments and reduce the ultimate bending moment and axial stress. The ultimate moment was found to be reduced by 57% for the frame analysis. Similarly, a 43% reduction in ultimate stress was observed for the finite element analysis. However, these results are specific to the geometry of the sample and will vary as the curvature and cross-sectional dimensions are altered.

4.3 Tensile Test Procedure

The tensile and flexural properties of the loggerhead carapace were determined through experimental investigation. A screw-type axial load testing device, with an accuracy of ± 4.45 N, was used for load application and data collection for the axial tension and three-point bending tests (Figure 4.12).



Figure 4.12: Tension-Compression Screw-Type Load Device

Bone is a composite material composed of a minerals and fibrous collagen. For this reason, ASTM D 3039 - *Standard Test Method for Tensile Properties of Polymer Matrix Composite Materials* was selected as a basis to determine the longitudinal and transverse tensile properties of the loggerhead sea turtle carapace. This test is suitable because it employs rectangular samples as an alternative to dog-bone specimens, which require extensive milling. However, the test sample parameters specified in the ASTM standard were modified where necessary in order to accommodate irregular specimen geometry.

The test is conducted by securing a sample in the grips of the test fixture and subjecting it to axial extension at a constant crosshead displacement rate of 2.54 mm/min. The load required to maintain the displacement rate and the sample elongation are recorded at 1.0 second intervals. The test is completed when rupture of the specimen occurs. Upon completion of testing, each sample is stored for future inspection. A successful tensile test is defined as tensile rupture perpendicular to the direction of loading that occurs along the gage length of the sample with no slipping detected at the bone-epoxy interface. A photo of the acceptable failure of a specimen is presented in Figure 4.13.

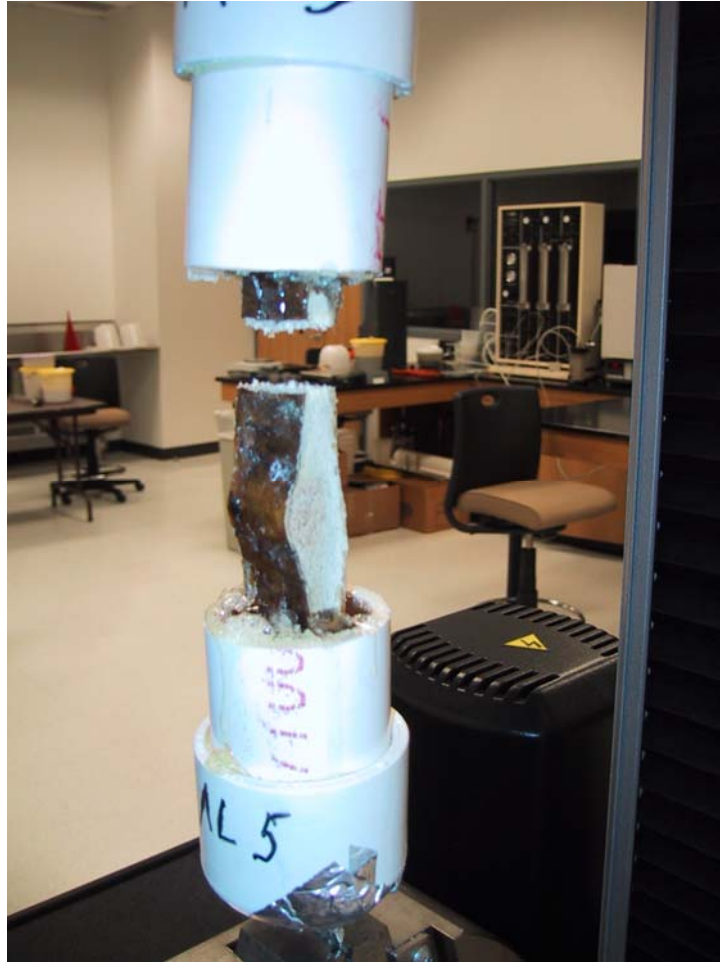


Figure 4.13: Example of Acceptable Tensile Failure of a Specimen (Tensile Rupture)

The primary mechanical properties of interest computed from the test data include ultimate tensile stress (σ_{ult}), tensile strain at failure (ϵ_f), and modulus of elasticity (E). Tensile stress is a quantitative measure of the intensity of load over a given area that is independent of specimen size. It is calculated by dividing the applied load by the original cross-sectional area. Thus, for non-prismatic specimens the stress is often determined using the minimum cross-sectional area. Tensile strain describes the potential for a material to deform in the direction of loading. This dimensionless property allows for the comparison of elongation data between specimens of various gage lengths and is computed by dividing the elongation of the sample by the initial length. The modulus of

elasticity is determined by computing the slope of the linear portion of the stress-strain curve.

4.4 Summary of Tensile Test Results - Carapace 1

For each test performed, stress-strain data were generated and used to compute the tensile properties. The subsequent plots offer examples developed through the testing of Carapace 1. Figure 4.14 is a graph of the stress-strain curve obtained through the testing of a longitudinally harvested sample. Similarly, Figure 4.15 is a plot of data acquired through the testing of a transversely harvested sample. Stress-strain graphs for each tensile sample harvested from Carapace 1 are displayed in Appendix A.

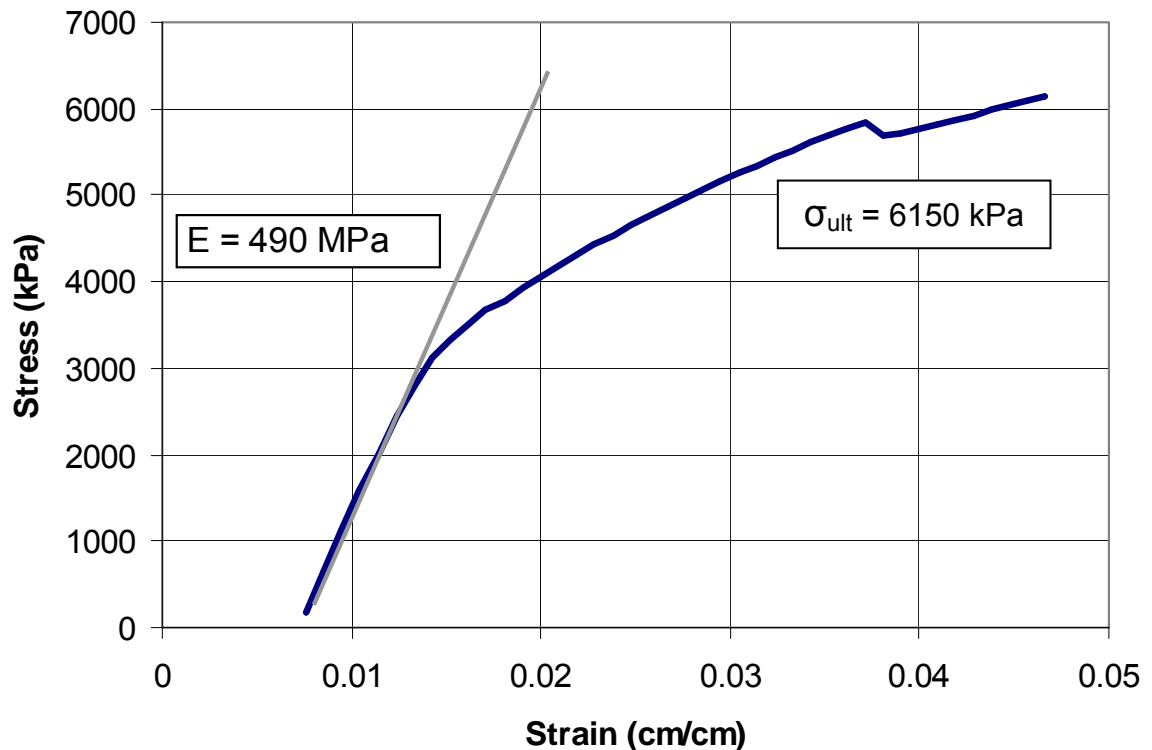


Figure 4.14: Stress-Strain Curve for Sample ML6 (Carapace 1)

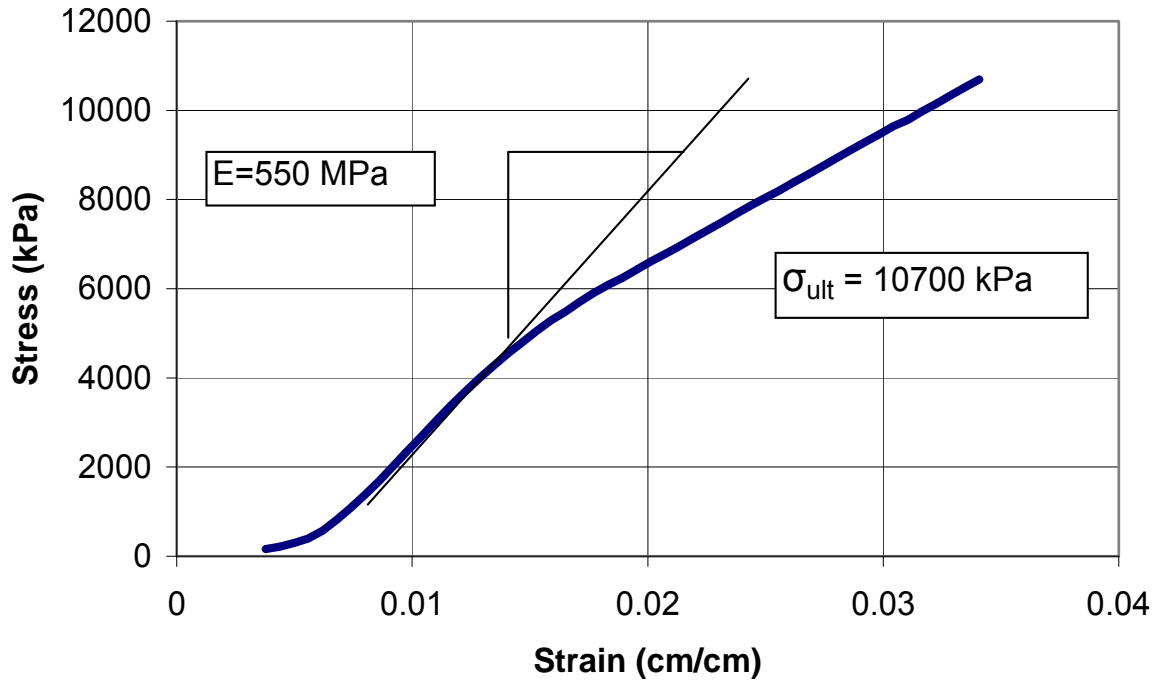


Figure 4.15: Stress-Strain for Sample MT4 (Carapace 1)

The following schematics illustrate the location and orientation of the samples harvested for tensile testing. The samples that are hatched in the schematics are excluded from the data analysis because they were utilized in the development of the test method and the results were obtained prior to finalizing the test parameters. The tables accompanying each schematic list the ultimate tensile strength, elastic modulus and strain at failure for each sample. In addition, the mean, standard deviation (STD), and coefficient of variation (COV) for each property have been included. The coefficient of variation is calculated by dividing the standard deviation by the mean. This value gives a dimensionless indication of the scatter within the data. Figure 4.16 shows the location and orientation of the middle longitudinal (ML) samples harvested, and Table 4.2 summarizes the physical properties computed.

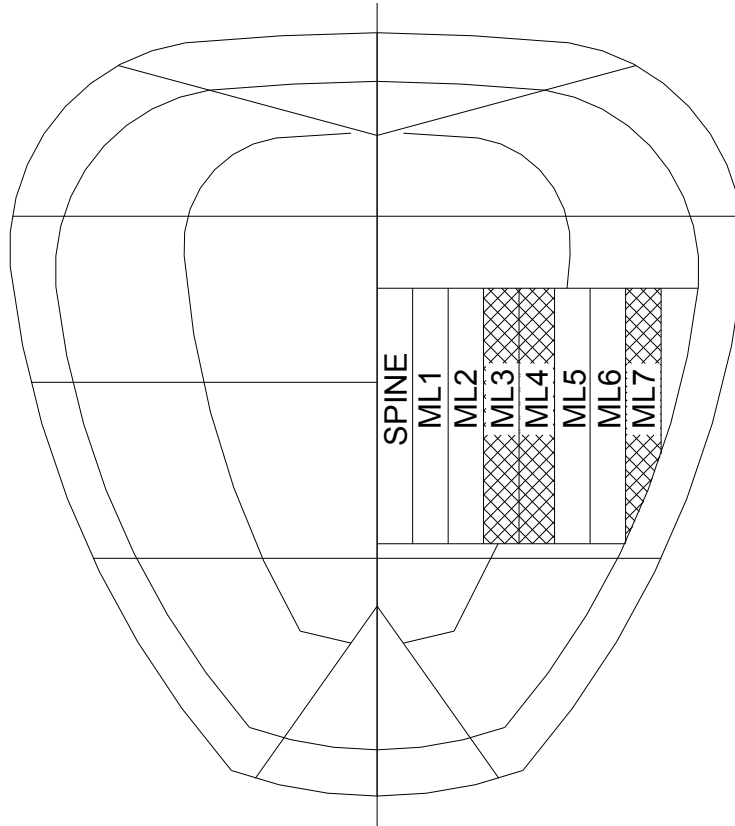


Figure 4.16: Middle Longitudinal Sample Locations and Orientations (Carapace 1)

Table 4.2: Middle Longitudinal Tensile Test Summary (Carapace 1)

Coupon Designation	Ult. Tensile Strength (kPa)	Elastic Modulus (MPa)	Strain at Failure
ML1	6190	530	2.82%
ML2	5190	323	3.66%
ML5	6610	257	4.83%
ML6	6150	490	4.61%
Mean	6030	400	3.98%
STD	601	131	0.925%
COV	10.0%	32.7%	23.2%

Figure 4.17 is a schematic illustration of the location and orientation of the middle transverse (MT) samples tested from Carapace 1. Table 4.3 summarizes the test results.

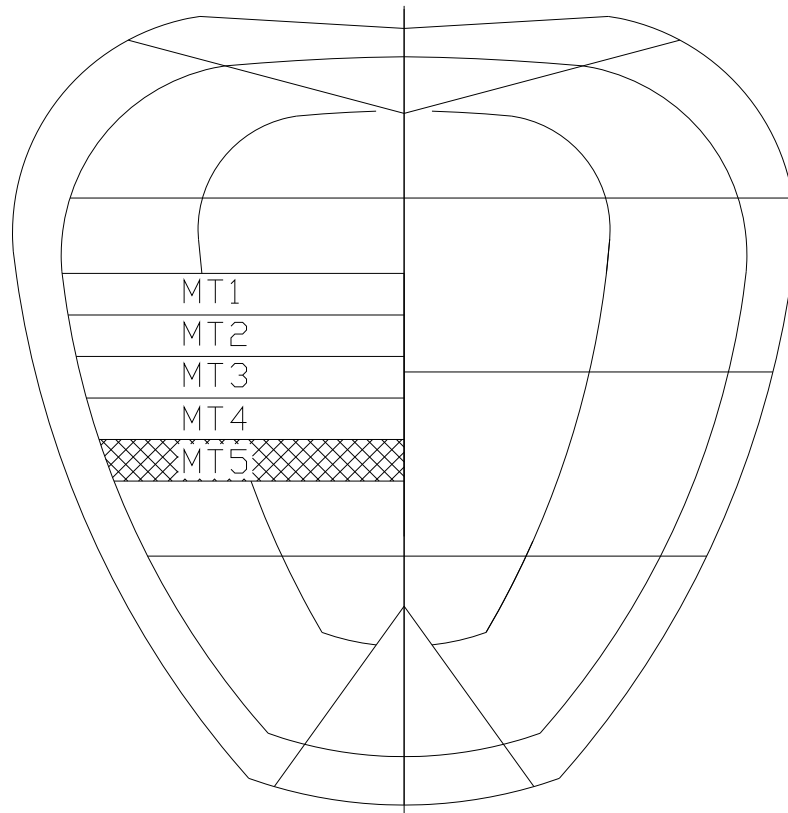


Figure 4.17: Middle Transverse Sample Locations and Orientations (Carapace 1)

Table 4.3: Middle Transverse Tensile Test Summary (Carapace 1)

Coupon Designation	Ult. Tensile Strength (kPa)	Elastic Modulus (MPa)	Strain at Failure
MT1	16200	740	9.10%
MT2	9170	579	3.57%
MT3	10100	527	6.34%
MT4	10700	550	3.42%
Mean	11600	599	5.61%
STD	3170	96.4	2.69%
COV	27.3%	16.1%	47.9%

Figure 4.18 depicts the location and orientation of the front transverse (FT) samples.

Table 4.4 summarizes the data collected from this region.

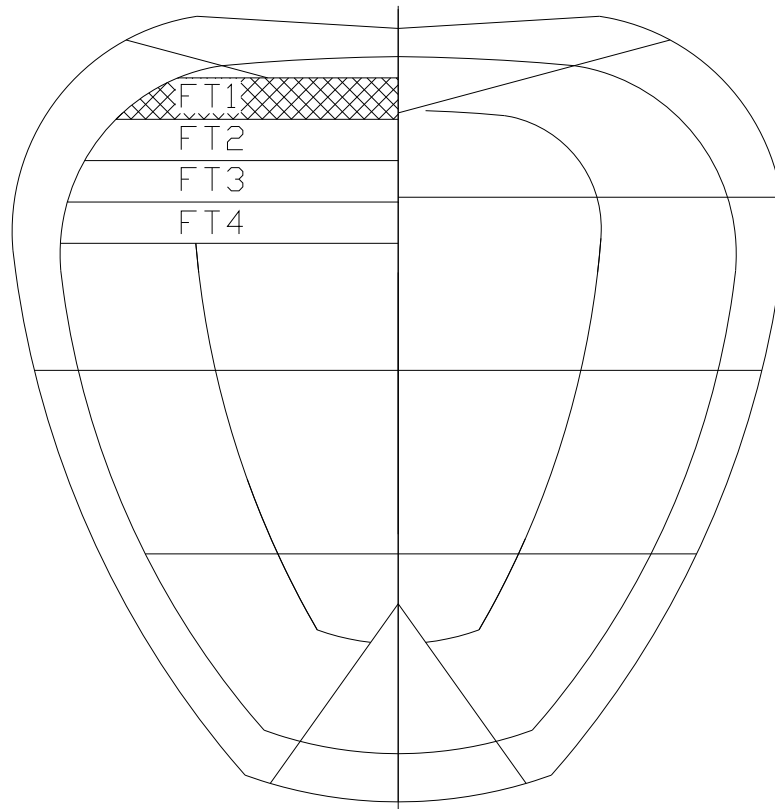


Figure 4.18: Front Transverse Sample Locations and Orientations (Carapace 1)

Table 4.4: Front Transverse Tensile Test Summary (Carapace 1)

Coupon Designation	Ult. Tensile Strength (kPa)	Elastic Modulus (MPa)	Strain at Failure
FT2	10000	433.0	2.42%
FT3	10100	464.0	8.35%
FT4	7850	217.0	7.58%
Mean	9320	371.0	6.12%
STD	1270	135.0	3.22%
COV	13.6%	36.4%	52.7%

4.5 Summary of Tensile Test Results - Carapace 2

The Carapace 2 samples that were removed from storage and immediately tested were found to have an inferior epoxy bond compared to those from Carapace 1. Numerous tests specimens failed at the bone-epoxy interface prior to tensile rupture. One example

of this is shown in Figure 4.19. The tests were considered unsuccessful and the resulting data were discarded.



Figure 4.19: Unsuccessful Test due to Failure of the Bone-Epoxy Interface

The unsuccessful failure may be attributed to moisture contained in the coupons that degraded the strength of the epoxy-bone interface. For this reason, it was necessary to allow the samples to dry for 3 days prior to testing. The sample designations were determined in accordance with Carapace 1 and the associated schematics may be referenced to determine location and orientation of the samples for Carapace 2.

The results of Carapace 2 tensile testing are summarized in the following tables. Tables 4.5, 4.6, 4.7, 4.8, 4.9 and 4.10 refer to the front longitudinal, front transverse, middle longitudinal, middle transverse, rear longitudinal, and rear transverse orientations respectively. Stress-strain plots for each Carapace 2 sample tested in tension are displayed in Appendix B.

Table 4.5: Front Longitudinal Tensile Test Summary (Carapace 2)

Coupon Designation	Ult. Tensile Strength (kPa)	Elastic Modulus (MPa)	Strain at Failure
FL1	2260	221	2.0%
FL3	5260	659	1.6%
FL4	2680	295	2.0%
FL6	1960	93.8	3.5%
FL9	2370	484	0.9%
Mean	2900	351	2.0%
STD	1340	223	1.0%
COV	46.2%	63.6%	48%

Table 4.6: Front Transverse Tensile Test Summary (Carapace 2)

Coupon Designation	Ult. Tensile Strength (kPa)	Elastic Modulus (MPa)	Strain at Failure
FT1	4770	297	2.11%
FT3	3340	380	1.70%
FT5	4310	258	2.58%
FT6	4910	515	1.60%
FT8	3490	368	1.33%
Mean	4160	364	1.86%
STD	721	98.5	0.487%
COV	17.3%	27.1%	26.1%

Table 4.7: Middle Longitudinal Tensile Test Results (Carapace 2)

Coupon Designation	Ult. Tensile Strength (kPa)	Elastic Modulus (MPa)	Strain at Failure
ML1	6190	530	2.80%
ML2	4240	499	1.30%
ML4	4410	485	1.74%
ML5	4120	232	2.70%
ML6	3110	272	2.81%
ML7	5790	656	1.66%
Mean	4640	446	2.27%
STD	1140	162	0.703%
COV	24.6%	36.4%	31.0%

Table 4.8: Middle Transverse Tensile Test Summary (Carapace 2)

Coupon Designation	Ult. Tensile Strength (kPa)	Elastic Modulus (Mpa)	Strain at Failure
MT1	3870	290	2.69%
MT3	4800	308	2.19%
MT4	5350	390	3.50%
MT5	5300	203	3.85%
MT10	5000	265	3.09%
Mean	4860	291	3.06%
STD	600	67.7	0.654%
COV	12%	23.2%	21.4%

Table 4.9: Rear Longitudinal Tensile Test Summary (Carapace 2)

Coupon Designation	Ult. Tensile Strength (kPa)	Elastic Modulus (MPa)	Strain at Failure
RL1	4460	218	2.60%
RL4	4720	308	3.04%
RL2	2630	113	3.48%
RL5	3010	90.3	5.35%
RL3	4660	213	3.78%
Mean	3900	189	3.65%
STD	996	88.2	1.05%
COV	25.5%	46.8%	28.8%

Table 4.10: Rear Transverse Tensile Test Summary (Carapace 2)

Coupon Designation	Ult. Tensile Strength (kPa)	Elastic Modulus (MPa)	Strain at Failure
RT2	2880	75.8	5.80%
RT4	2560	148	2.83%
RT5	3060	225	2.29%
RT3	6850	524	2.36%
RT7	4610	177	5.79%
Mean	3990	230	3.81%
STD	1780	173	1.82%
COV	44.6%	75.2%	47.7%

Table 4.11 summarizes the average tensile material properties for Carapace 2 for the longitudinal and transverse orientations. In addition, the overall average material properties have been included.

Table 4.11: Mean Tensile Properties Obtained from Carapace 2

Orientation	Ult. Tensile Strength (kPa)	Elastic Modulus (Mpa)	Strain at Failure
Longitudinal	3820	328	2.64%
Transverse	4340	295	2.91%
Overall	4080	312	2.77%

The average transverse and longitudinal ultimate strength values for Carapace 2 are relatively consistent with a 12.2% variation. In addition, the modulus and strain at failure values have similar results with 10.1% and 10.7% variation respectively. The higher tensile capacity associated with the transverse direction found in Carapace 1 is not observed in the results of the preserved sample testing. This is illustrated in Table 4.12, which compares the average tensile properties found in Carapace 1 with those of Carapace 2 for the longitudinal and transverse orientations.

Table 4.12: Comparison of Carapace 1 and 2 Mean Properties

Orientation	Ult. Tensile Strength (kPa)	Elastic Modulus (MPa)	Strain at Failure
Longitudinal Carapace 1	6030	400	3.95%
Longitudinal Carapace 2	3820	328	2.60%
% Difference	36.7%	18.0%	34.2%
Transverse Carapace 1	10500	485	5.85%
Transverse Carapace 2	4340	295	2.91%
% Difference	58.7%	39.2%	50.3%

4.6 Consideration of Additional Normal Stress due to Bending

The properties displayed in the previous section do not account for the bending induced stresses. However, the objective of this study is to mimic failure under equivalent loading. The curvature, harvesting techniques, and tensile test procedure will be analogous for the synthetic and biological shells. In effect, it will be possible to simulate the force required to fail the shell without directly determining the curvature induced moments. In contrast, it will be necessary to account for the additional stress in order to determine the true tensile properties.

It was previously shown that the specialized tabs used for the axial tension test reduce the effects of curvature-induced bending moment. However, it was also noted that the stress induced by bending is not insignificant. In many applications it is necessary to determine the precise stress at failure. This may be difficult for curved samples as second-order effects must be considered. Although, it is possible to determine this property from the axial test if the transverse displacement of the sample is recorded. The ultimate load at failure and the curvature of the sample may be considered with simple

mechanics to calculate the strength. The normal stress due to the combination of axial loading and bending moment may be computed through Equation (4.1):

$$\sigma = \frac{P}{A} \pm \frac{M \cdot y}{I} \quad (4.1)$$

Where

σ = normal stress

P = tensile load

A = cross - sectional area

M = bending moment

y = distance from the centroid of the cross - section

I = Moment of Inertia

For a curved coupon, the moment is equivalent to the axial load multiplied by the eccentricity (e), which is determined by the initial geometry of the sample. The ultimate stress is located within the extreme fibers at a distance from the centroid equal to one half the depth (d). Substituting these values into Equation (4.1) yields:

$$\sigma_{ult} = \frac{P_{ult}}{b \cdot d} \left(1 + \frac{6 \cdot e}{d} \right) \quad (4.2)$$

Where

σ_{ult} = ultimate normal stress

P_{ult} = ultimate tensile load

b = width of coupon

d = depth of coupon

e = initial eccentricity of tensile loading

However, this calculation does not consider the decrease in sample curvature that develops as a result of the axial extension. Neglecting these second order effects will result in significantly over-predicting the strength of the sample. In order to determine the stress accurately, the transverse displacement (Δ_t) must be recorded at the time the ultimate load is reached. This value can then be subtracted from the initial eccentricity resulting in Equation (4.3). This calculation may be employed to determine the ultimate normal stress that occurs in the sample during the tensile test.

$$\sigma_{ult} = \frac{P_{ult}}{b \cdot d} \left(1 + \frac{6 \cdot (e - \Delta_t)}{d} \right) \quad (4.3)$$

Where

Δ_t = transverse displacement at the time ultimate load is achieved

Figure 4.20 displays the unloaded and deformed shape for a curved sample subjected to an axial tension test. The initial eccentricity and transverse displacement have been included and are labeled at mid-span.

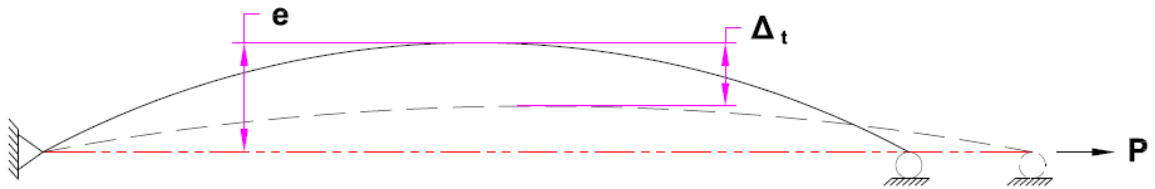


Figure 4.20: Initial Eccentricity and Transverse Displacement of a Curved Sample Subjected to an Axial Tension Test

Equation (5.3) was employed to determine the ultimate stress in coupon FT3 harvested from Carapace 2. The results were then compared to the finite element stress

distribution in Figure 4.10. The cross-sectional dimensions are given in Figure 4.4 with (d) and (b) equal to 0.91 cm. and 2.62 cm. respectively. Furthermore, the initial eccentricity and transverse displacement at mid-span of the model were found to be 0.75 cm. and 0.61 cm. respectively. The tensile test resulted in an ultimate load of 768 N. Substituting these values into Equation (3) yields an ultimate tensile strength of 6200 kPa. Similarly, the finite element analysis determined the ultimate tensile strength to be equal to 6100 kPa. This results in a percent variation of 1.5%, suggesting that Equation (4.3) offers a reasonable estimation of the ultimate normal stress for a curved sample subjected to axial tension.

4.7 Flexural Test Procedure and Data Collection

The test performed in order to determine the longitudinal and transverse flexural properties of the loggerhead sea turtle carapace is based on ASTM D 790 - *Standard Test Method for Flexural Properties of Unreinforced and Reinforced Plastics and Electrical Insulating Materials*. As with the tensile testing procedure, this standard was selected for its effectiveness at directly evaluating the flexural capacity of rectangular composite samples. Test parameters were modified where necessary in order to accommodate irregular specimen geometry. The screw-type load testing device shown in Figure 4.12 was utilized in load application and data logging.

The mechanical properties computed from the test results are modulus of rupture (maximum flexural stress), flexural strain at failure, and flexural modulus. The modulus of rupture is the stress in the outermost fibers determined at failure of the sample. Strain at failure is a measure of the deformation of the samples outermost fibers at the point of

rupture. Lastly, the flexural modulus is a quantitative measure of a sample's resistance to bending and is a function of the slope of the linear portion of the load versus deformation curve. The dimensions of the coupons allow for all properties to be determined through a three-point bending test where a load-deformation curve is developed. The flexure test is shown in Figure 4.21.

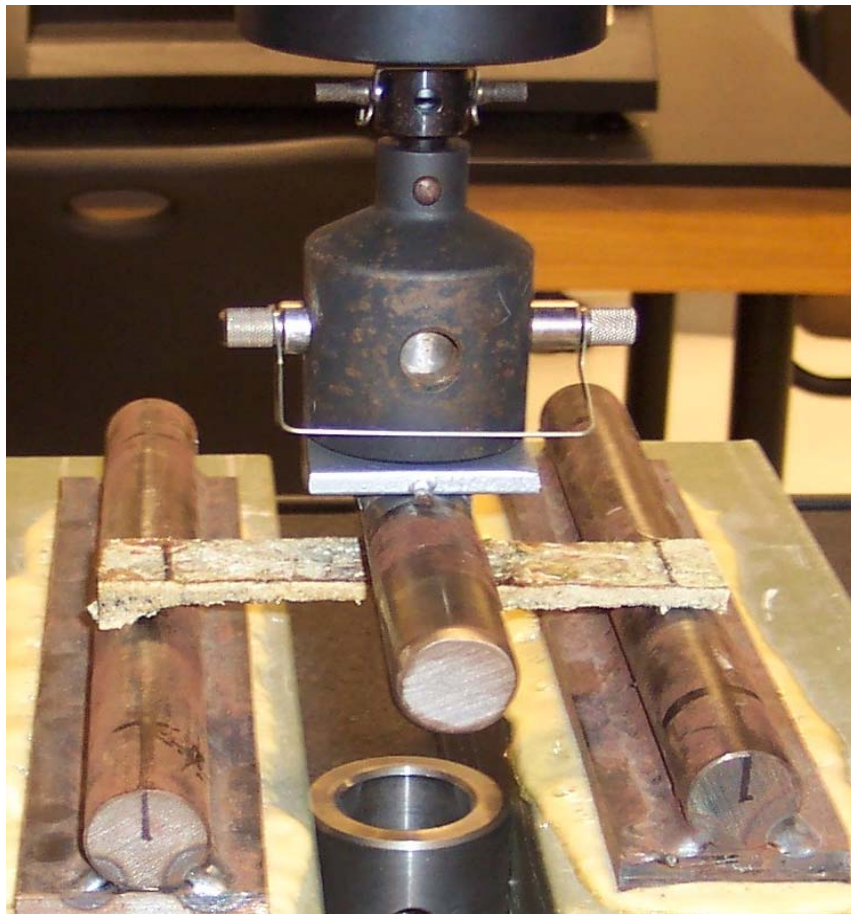


Figure 4.21: Typical Flexure Test

For this test, a variable point load is applied at mid-span of the coupon to maintain a constant deformation rate. The force is resisted by the supports at either end. The load required to maintain the displacement and the deformation at mid-span are recorded at

1.0 second intervals. The three-point bending test is completed when rupture of the specimen occurs. Upon completion of testing, each sample is stored for future inspection.

For each bending test performed, load-deformation data were acquired and used to compute the properties shown in the following data summaries. The subsequent graphs offer an example of the typical load-deformation curves developed through the flexural testing of Carapace 3. The plots developed for each sample subjected to three-point bending are displayed in Appendix D. Figure 4.22 is a plot of data obtained through the testing of one of the longitudinally harvested samples. Similarly, Figure 4.23 is a plot of data acquired through the flexural testing of one of the transversely harvested samples. The slope of the linear portion of the curve, designated (m), has been included in each figure.

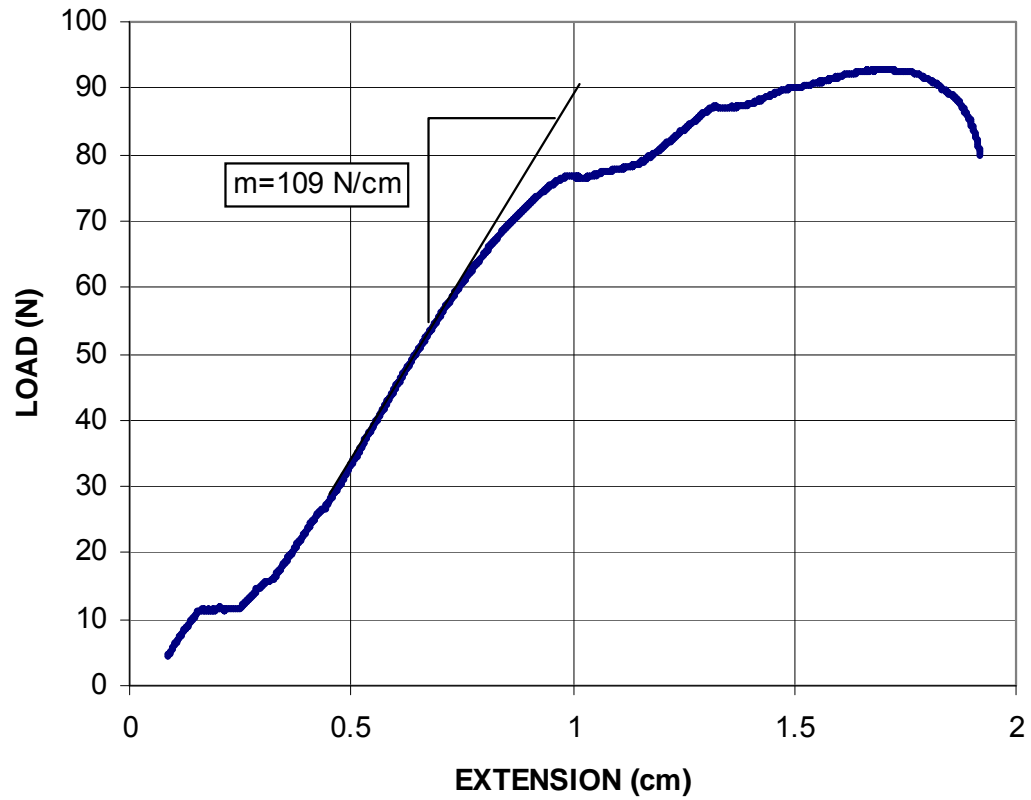


Figure 4.22: Load-Deflection Curve for Sample ML4 (Carapace 3)

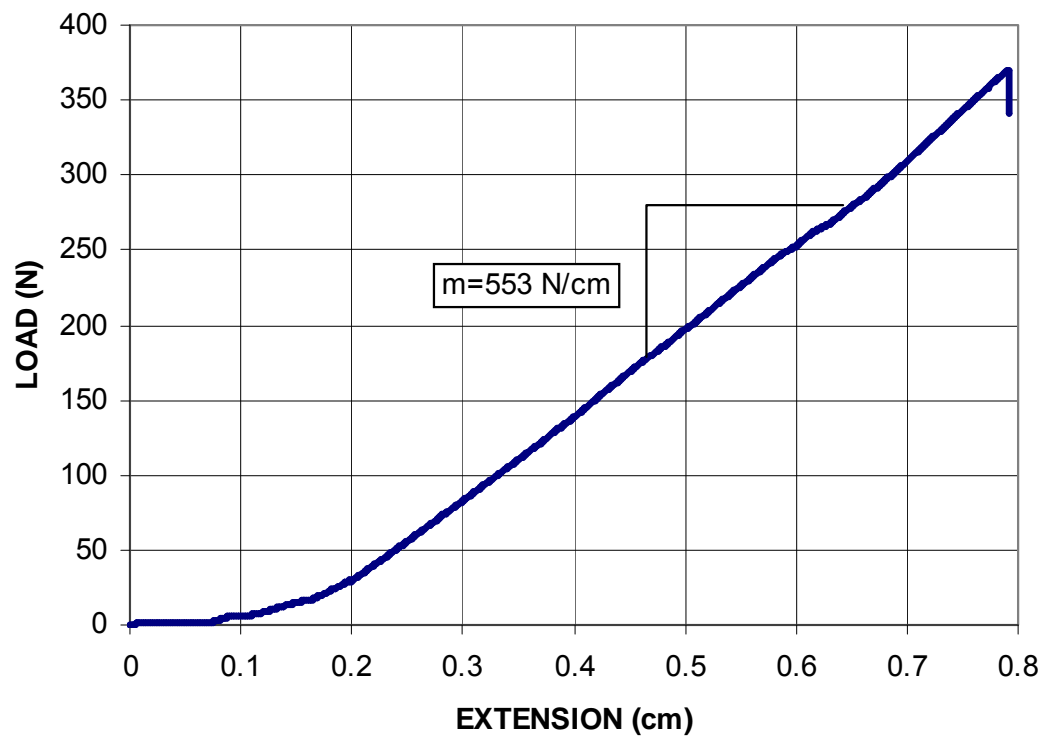


Figure 4.23: Load - Deflection Curve for Sample MT3 (Carapace 3)

The sample designations for flexure are identical to those used for tension testing and denote the specimen's location relative to the intact carapace. Figures 3.3, 4.16, 4.17, and 4.18 may be referenced in order to determine specimen location and orientation. Tables 4.13, 4.14, and 4.15 list the material properties determined through flexural testing of the middle longitudinal, middle transverse, and front transverse specimens respectively. The geometry of the samples harvested from the rear of the carapace prevented testing due to insufficient span lengths. In addition, impact damage associated with the front right quadrant prohibited the testing of samples from this region.

Table 4.13: Middle Longitudinal Flexural Test Summary (Carapace 3)

Coupon Designation	Modulus of Rupture (kPa)	Flexural Strain at Failure	Bending Modulus (Mpa)
ML1	10900	1.07%	1260
ML2	7070	2.60%	774
ML3	5680	2.53%	336
ML4	16000	2.32%	1520
ML5	10600	1.21%	860
ML6	8500	1.51%	799
Mean	9790	1.87%	925
STD	3640	0.69%	414
COV	37.2%	36.8%	44.7%

Table 4.14: Middle Transverse Flexural Test Summary (Carapace 3)

Coupon Designation	Modulus of Rupture (kPa)	Flexural Strain at Failure	Bending Modulus (Mpa)
MT1	47200	1.82%	4150
MT2	49000	1.39%	4730
MT3	27500	1.50%	2230
MT4	70700	1.17%	5580
MT5	22600	1.90%	1600
MT6	19700	1.82%	1240
Mean	39500	1.60%	3260
STD	19700	0.291%	1800
COV	49.9%	18.2%	55.2%

Table 4.15: Front Transverse Flexural Test Summary (Carapace 3)

Coupon Designation	Modulus of Rupture (kPa)	Flexural Strain at Failure	Bending Modulus (Mpa)
FT1	33200	1.97%	1620
FT2	7150	1.43%	1140
FT3	17700	1.52%	1640
FT4	20400	2.09%	1300
FT5	22400	1.85%	1350
Mean	20200	1.77%	1410
STD	9360	0.287%	215
COV	46.3%	16.2%	15.3%

The flexural test results indicate that the modulus of rupture for the middle transverse samples is approximately 4 times greater than the modulus of rupture for the middle longitudinal samples. Furthermore, the mean modulus of rupture found for the front transverse samples is approximately twice the value determined for the middle longitudinal samples. Similar relationships are observed between the bending modulus values for the alternate test regions. In contrast, the strain at failure values are relatively consistent with an average of 1.8%. The reduced values found for modulus of rupture and bending modulus associated with the longitudinal samples may be attributed to a soft, light-colored tissue running transversely through the carapace at approximately 5 cm increments. This tissue has a significantly reduced bending capacity, inducing a localized failure of the specimen. Figure 4.24 shows the light-colored tissue located in the previously tested middle longitudinal samples. Predictably, each longitudinal specimen failed in bending at the centermost location of the soft tissue.



Figure 4.24: Soft Tissue in Middle Longitudinal Samples (Carapace 3)

The modulus of rupture and the bending modulus determined from the three-point bending test are significantly larger than the ultimate strength and the elastic modulus found from the tensile testing. This may be explained by perceiving the carapace as a sandwich composite with the outer layers comprised of a stiffer, stronger material. When the sample is loaded in pure bending, the longitudinal stress is highest at the outer surfaces of the sample and approaches zero at the centroid of the cross-section. Thus, weak tissue at the center of the sample would not have a significant impact on the flexural strength. Conversely, samples loaded in axial tension are assumed to resist the force uniformly over the entire cross-sectional area. Weak material located at the center of the sample would increase the cross-sectional area without significantly increasing the load-carrying capacity of the sample. In effect, the tensile strength would be reduced.

Chapter 5

Effects of Sample Geometry on Experimental Results and Determination of Target Properties

In order to determine the effects of varying sample geometry on tensile behavior, the properties obtained for the Carapace 2 samples were plotted against dimensionless ratios associated with their geometry (e.g. thickness / width). The dimensionless values are advantageous because they are independent of the scale of the sample. Identifying any trends will aid in determining geometrical characteristics that directly influence the measured properties of the loggerhead carapace.

The nominal sample dimensions were identified as shown in Figure 5.1. The gage length is measured as the linear length of exposed carapace located between the specialized tabs. It should also be noted that the minimum thickness and width were recorded for each sample and used to compute the properties discussed within this chapter. The measured width, thickness, and gage length ranged from 2.39 cm to 2.69 cm, 0.74 cm to 1.52 cm, and 1.98 cm to 17.15 cm respectively.

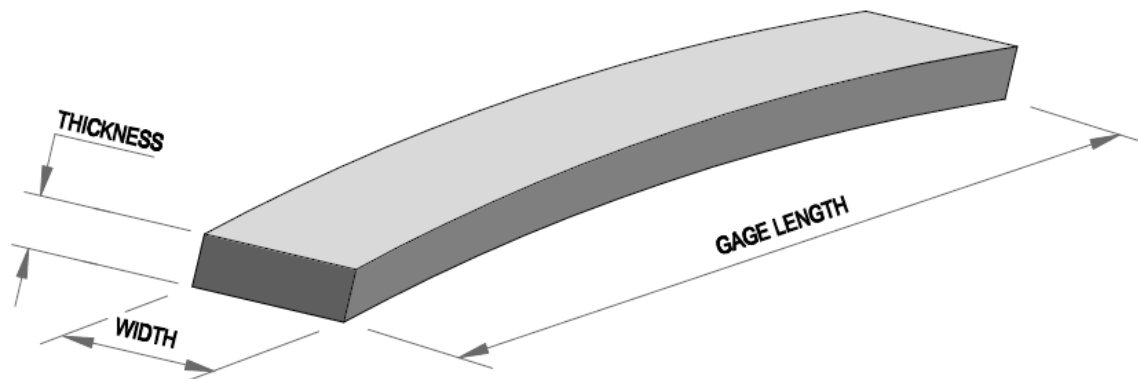


Figure 5.1: Sample Dimensions used to Determine Dimensionless Ratios

5.1 Effects of Sample Geometry on Tensile Strength

Figure 5.2 is a plot of ultimate stress versus the ratio of gage length to thickness for each coupon harvested from Carapace 2. While significant scatter exists, the relatively flat trend line may suggest that the ratio of gage length to thickness does not have a significant impact on the measured strength of the samples.

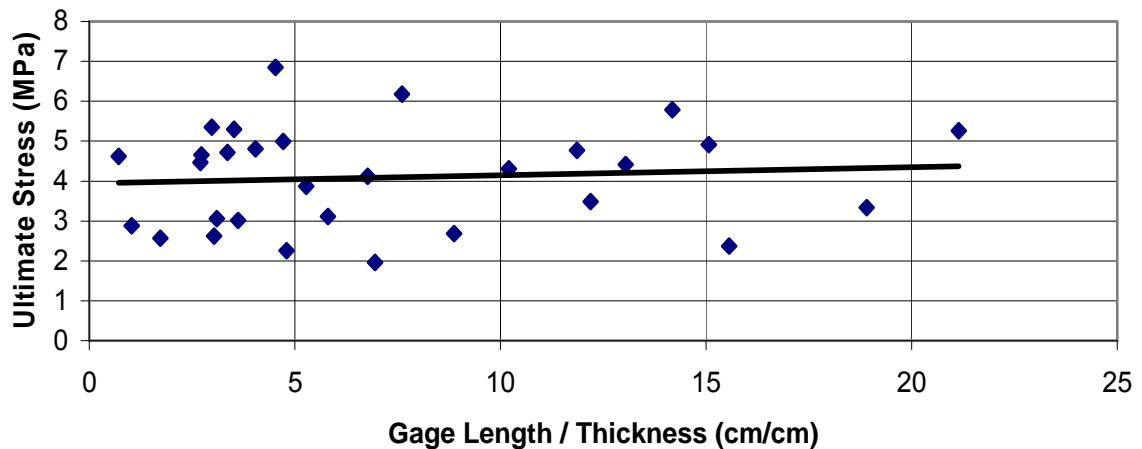


Figure 5.2: Ultimate Stress versus the Ratio of Gage Length to Thickness (Carapace 2)

Figure 5.3 is a plot of ultimate stress versus the ratio of gage length to width. Since the width of each sample was held relatively constant at approximately 2.5 cm, this graph offers insight into the effects of the gage length on the strength of the sample. The relatively flat trend line indicates no significant relationship between these two variables.

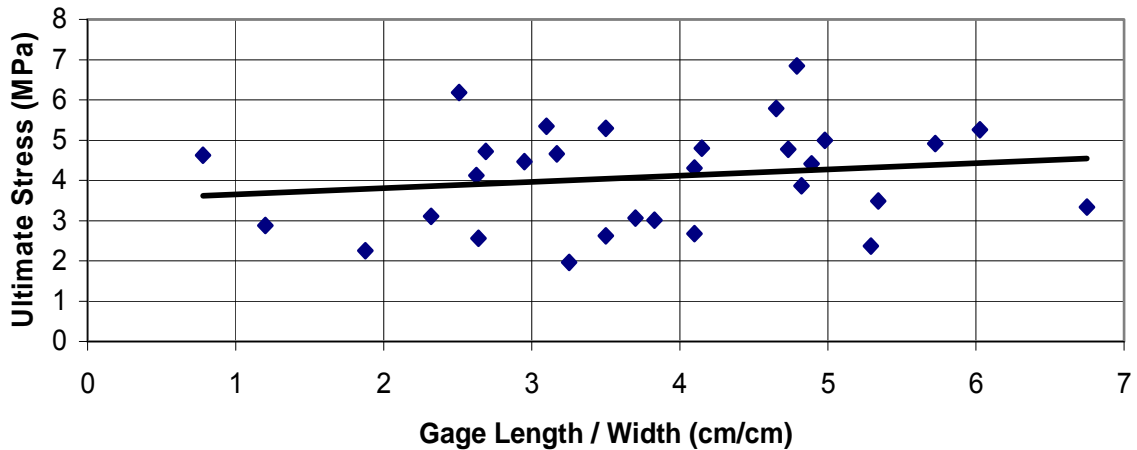


Figure 5.3: Ultimate Stress versus the Ratio of Gage Length to Width (Carapace 2)

Figure 5.4 shows ultimate load versus the ratio of thickness to width. The width of each sample was constant, permitting direct evaluation of the relationship between strength and thickness. The trend of this plot indicates that the thickness has no significant impact on the load capacity of the sample. This phenomenon is further reinforced by observing Figure 5.5, which illustrates the relationship between ultimate stress and the ratio of thickness to width. This graph indicates that as the thickness of the sample increases the ultimate stress decreases.

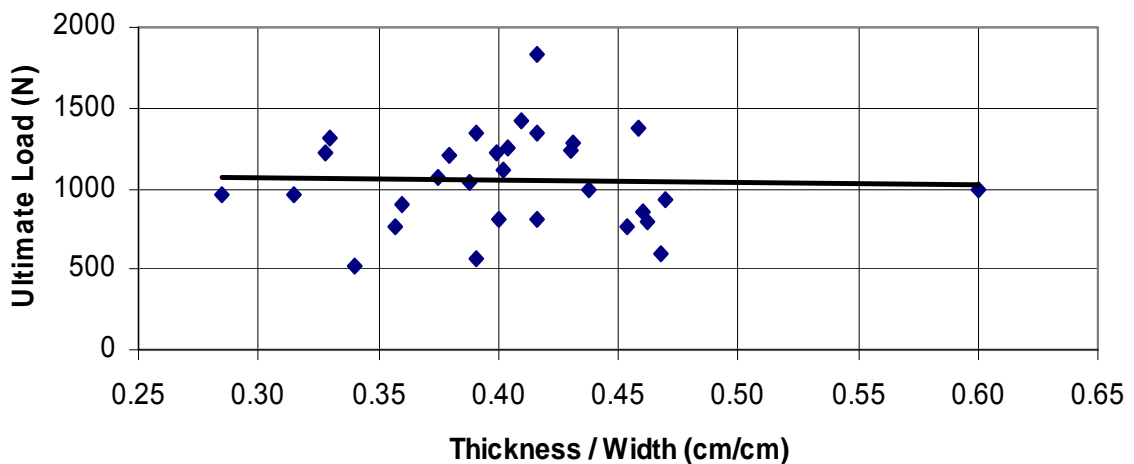


Figure 5.4: Ultimate Load versus the Ratio of Thickness to Width (Carapace 2)

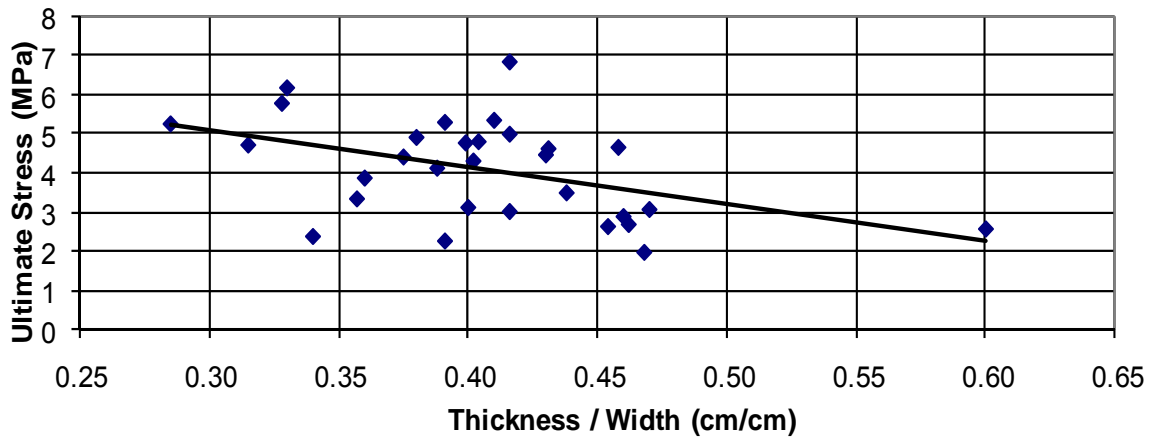


Figure 5.5: Ultimate Stress versus the Ratio of Thickness to Width (Carapace 2)

5.2 Effects of Sample Geometry on Strain at Failure

Additional trends were also observed when considering the effects of sample geometry on strain at failure. Figure 5.6 graphs the strain at failure versus the ratio of thickness to width. The plot suggests that as thickness of the coupon is increased the strain at failure increases.

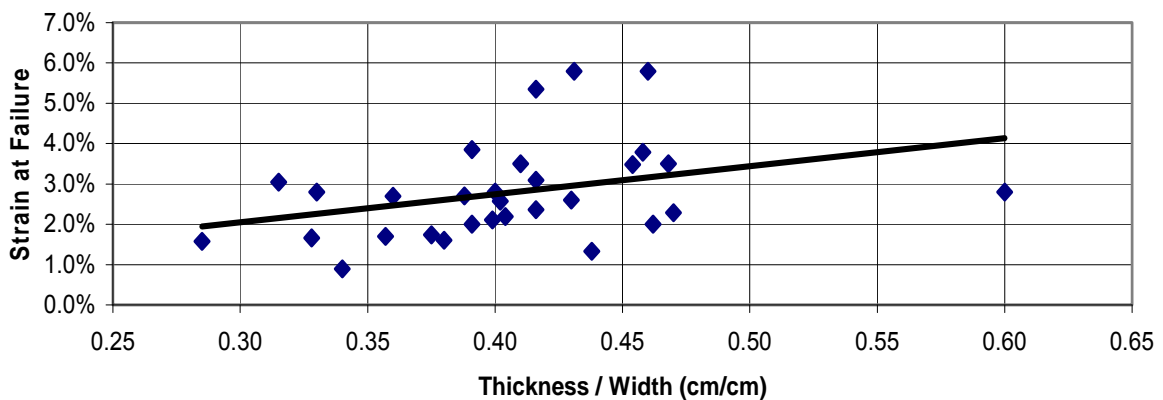


Figure 5.6: Strain at Failure versus the Ratio of Thickness to Width (Carapace 2)

Figure 5.7 is a plot of the strain at failure versus the ratio of gage length to thickness. The trend line clearly indicates that increases in this ratio decrease the strain at failure.

Figure 5.8 is a plot of strain at failure versus the ratio of gage length to width and suggests trends similar to the preceding graph. The plot implies that increases in gage length decrease the strain at failure.

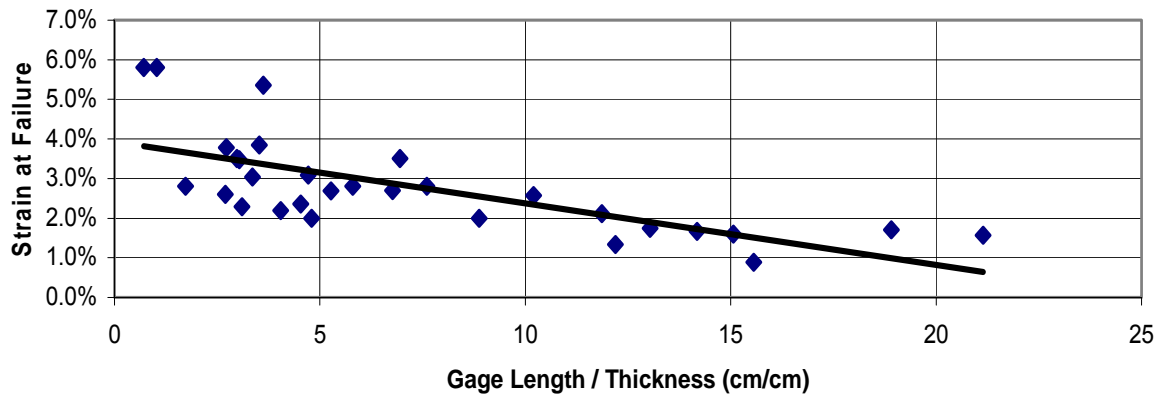


Figure 5.7: Strain at Failure versus the Ratio of Gage length to Thickness

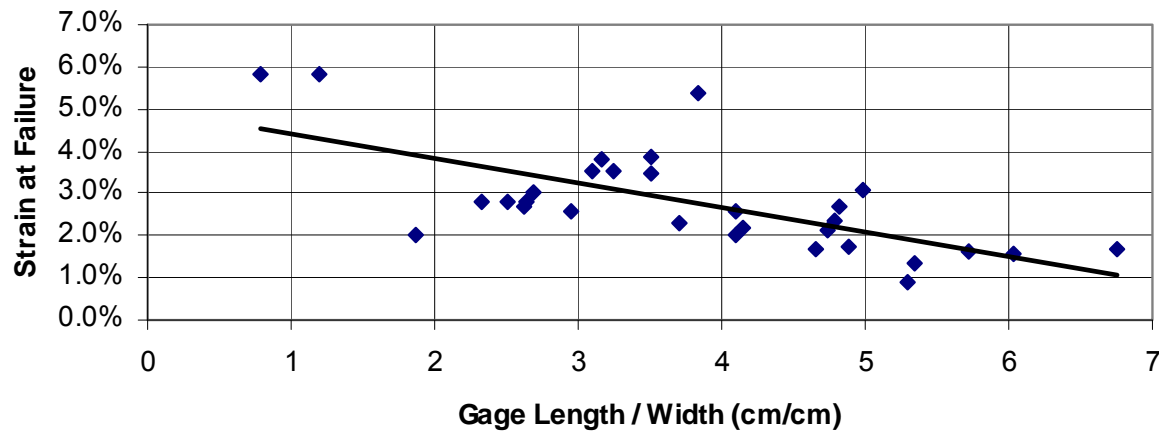


Figure 5.8: Strain at Failure and the Ratio of Gage Length to Width

5.3 Effects of Sample Geometry on Tensile Modulus

Figures 5.4 and 5.5 indicate that the thickness of the sample does not significantly affect the load capacity immediately prior to failure. It should also be noted that similar behavior was observed in the elastic region of the material. Figure 5.9 is a plot of

modulus versus the ratio of thickness to width for the samples harvested from Carapace

2. The graph clearly shows that as the thickness of the sample increases the modulus decreases. A similar trend can be observed in Figure 5.10, which is a plot of modulus versus the ratio of gage length to thickness. This relationship may also be directly influenced by the thickness of the coupon. Note that as the thickness decreases an increase in modulus is observed.

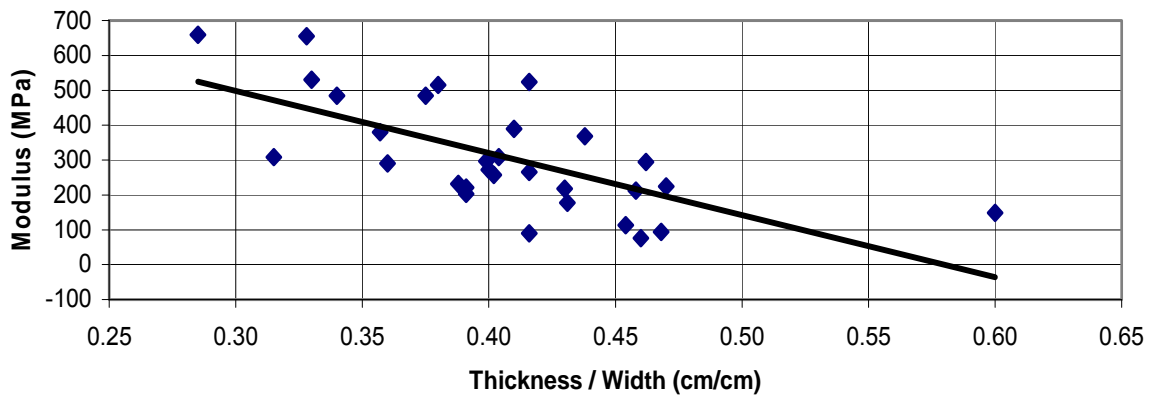


Figure 5.9: Modulus versus the Ratio of Thickness to Width (Carapace 2)

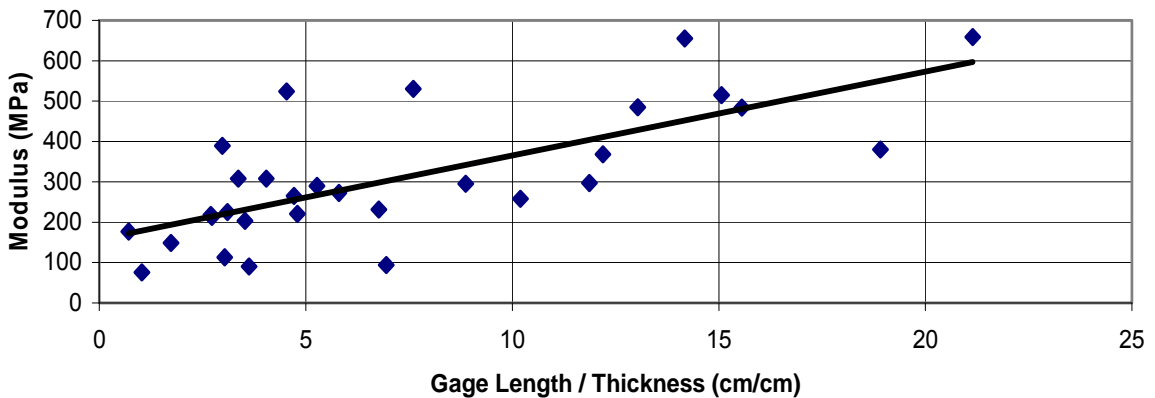


Figure 5.10: Modulus versus the Ratio of Gage Length to Thickness. (Carapace 2)

A final example of the effects of geometry on tensile modulus is given in Figure 5.11 where the property is plotted against the ratio of gage length to width. Noting that the

width was held relatively constant among samples, it may be observed that the modulus increases as the gage length is increased.

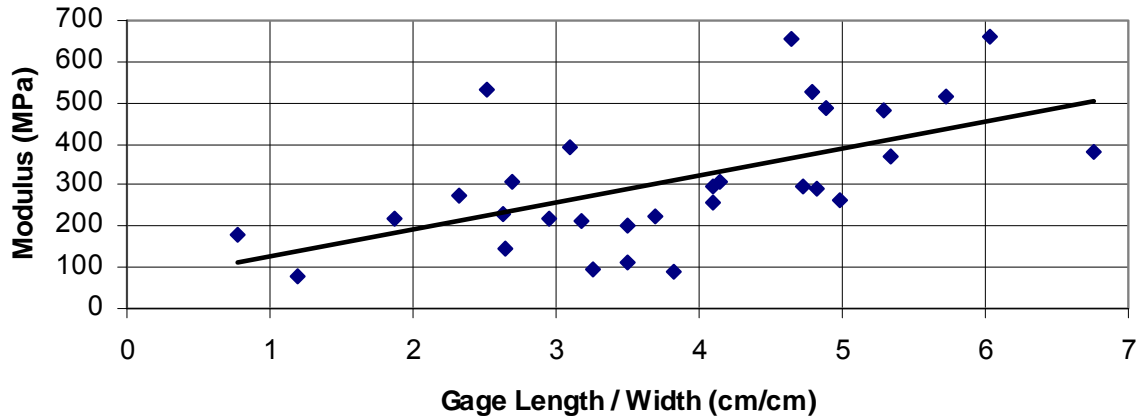


Figure 5.11: Modulus versus the Ratio of Gage Length to Width (Carapace 2)

5.4 Relationship between Sample Thickness and Tensile Load Capacity

Recalling Hooke's Law, Figures 5.9 and 5.10 indicate that as the thickness increases the stress required to induce a unit strain is reduced. This implies that the load deformation relationship is not significantly affected by the thickness of the coupon for the linear region. Similarly, Figures 5.4 and 5.5 reveal trends indicating that the thickness of the coupon does not have a significant impact on load capacity.

This phenomenon is counterintuitive but may be explained by again perceiving the carapace as a sandwich composite with the outer layers acting as the primary source of tensile strength. This model is further justified by the relatively large flexural modulus and ultimate flexural strength values observed when compared to the tensile properties.

In order to further investigate this relationship, the remaining Carapace 3 specimens were tested in tension. An identical analysis was conducted with the resulting data.

Figures 5.12 through 5.15 reaffirm the relationships between strength and specimen geometry observed in Carapace 2.

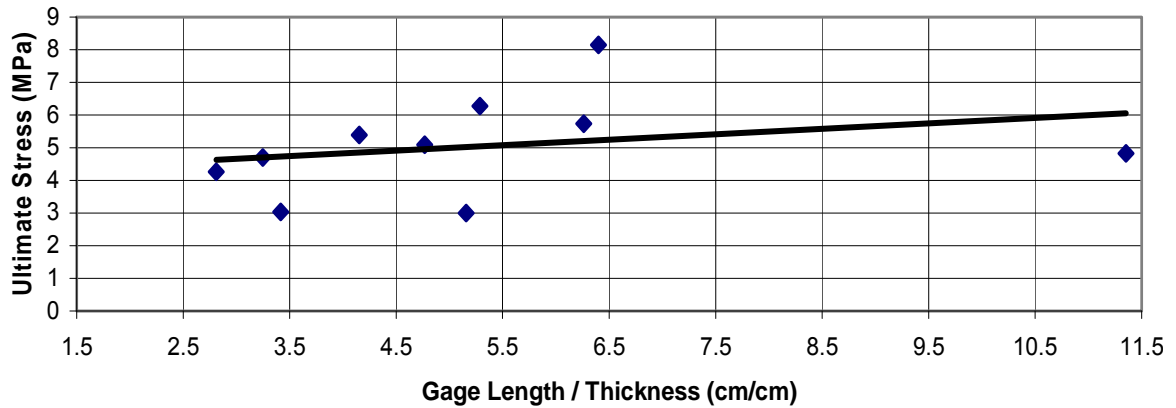


Figure 5.12: Ultimate Stress versus the ratio of Gage Length to Thickness (Carapace 3)

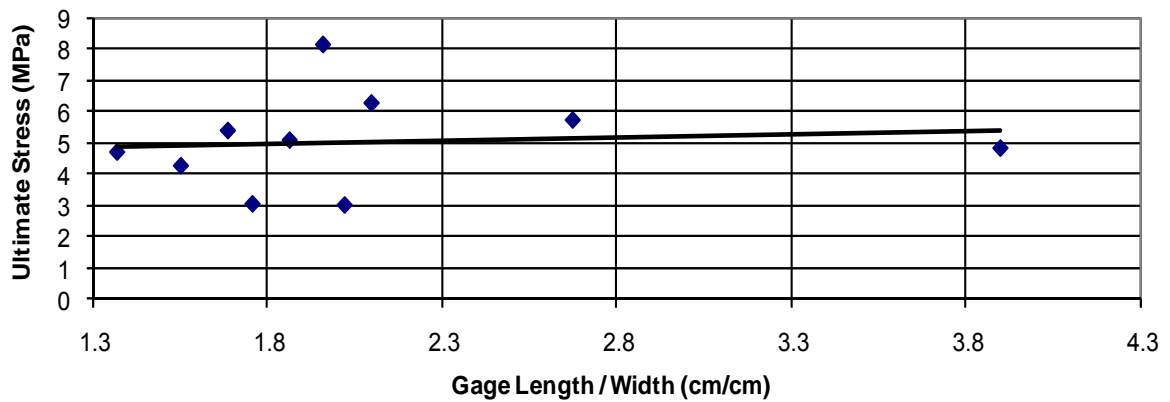


Figure 5.13: Ultimate Tensile Stress versus the ratio of Gage Length to Width (carapace 3)

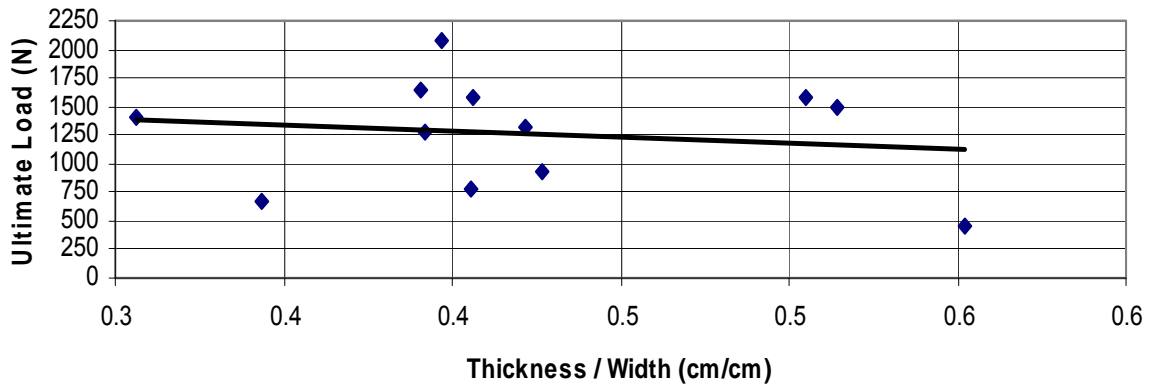


Figure 5.14: Ultimate Load versus Thickness to Width Ratio (Carapace 3)

Figure 5.14 shows that the thickness of the sample does not have significant impact on the load capacity. This phenomenon is again demonstrated in Figure 5.15 as an increase in the ratio of thickness to width results in a decrease in ultimate strength.

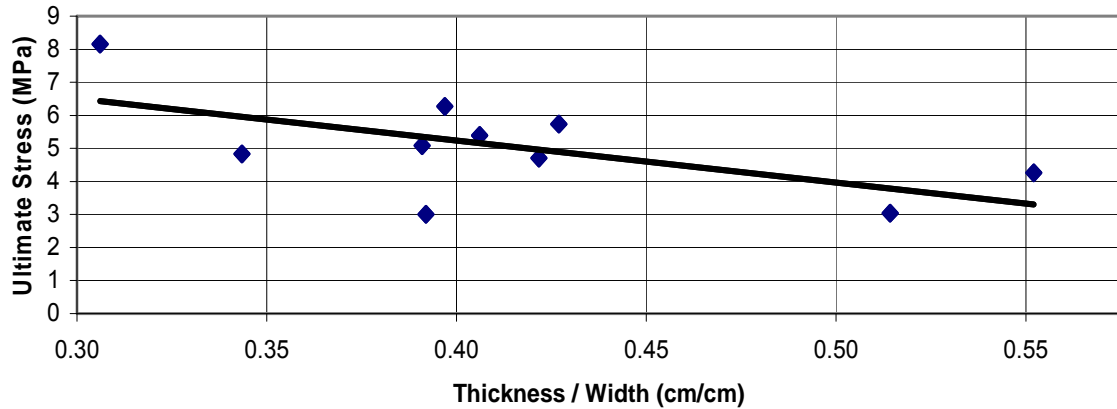


Figure 5.15: Ultimate Stress versus the ratio of Thickness to Width (Carapace 3)

The parametric study indicates that the load capacity of the turtle shell coupons is not dependent on thickness. Neglecting potential variations in biological composition, thickness is the primary parameter that would vary locally with shell growth. This suggests that the load per unit width required to fail the shell in tension may be independent of the age of the loggerhead, beyond some threshold value.

5.5 Determination of Target Properties

The tensile test results indicated that ultimate strength and modulus of elasticity varied significantly between Carapace 1 and Carapace 2. This may be attributed to the fact that Carapace 2 was preserved prior to testing and indicates the significant effect biological decay may have on the mechanical properties of the carapace. For this reason,

it was concluded that the material characteristics corresponding to Carapace 2 would more closely mimic the tensile properties of the living organic shell.

The results of the parametric study indicate that the thickness of the coupons does not significantly influence the tensile load capacity of the sample. For this reason, the target value used for simulating tensile failure of the shell will be force per unit width at failure rather than ultimate tensile strength. This value will be determined by multiplying the ultimate strength value recorded by the thickness of the sample. It should be noted that the width of the samples harvested from the biomimetic shell will be identical to that of the natural carapace. Similarly, the width of the intact biomimetic shell will simulate the width of the intact biological carapace. As a result, the load at failure of the biological shell will be simulated by equating force per unit width at failure of the artificial and natural shells.

The use of force per unit width in place of ultimate strength allows for varying the thickness of the synthetic specimens in order to replicate the tensile force required to rupture the real carapace. In effect, relatively high strength materials may be evaluated at minimal thickness in order to reduce the load capacity. Table 5.1 lists the target tensile properties obtained from the mean Carapace 2 test results.

Table 5.1: Target Tensile Material Properties

Orientation	Ult. Tensile Strength (kPa)	Modulus (MPa)	Strain at Failure	Ult. Force / Width (N/cm)
Longitudinal	3810	328	2.64%	359
Transverse	4340	295	2.91%	457
OVERALL	4080	312	2.76%	408

Once received, Carapace 3 was subjected to flexural testing immediately. Samples obtained from the middle region were taken from areas that did not contain segments of continuous rib bone. Due to the geometry of the front regions it was necessary to include significant sections of rib in the test coupons obtained from these areas. The properties of the rib and spine elements should be determined independently of the carapace as they may be dissimilar. For this reason, the averages of the middle longitudinal and transverse test results will be applied as the target flexural properties for the synthetic carapace. The target flexural properties are displayed in Table 5.2.

Table 5.2: Target Flexural Material Properties

Orientation	Max Flexural Stress (kPa)	Bending Modulus (MPa)	Flexural Strain at Failure
Longitudinal	9790	924	1.87%
Transverse	39400	3250	1.60%

Chapter 6

Prototype Fabrication and Evaluation

The process of determining suitable synthetic carapace constituents was conducted parallel to the testing of the natural shell. Consequently, the strength and elongation values for Carapace 1 were initially used to determine design properties. From these values many candidate materials and composite constituents were assessed in order to determine their potential for this application. Once the final target properties were determined, materials were selected and two prototype synthetic shells were fabricated and tested in axial tension. The average tensile properties found for the prototypes were then compared to the target properties given in Chapter 5.

6.1 Candidate Materials for Synthetic Shell Fabrication

Table 6.1 shows examples of matrix materials that were evaluated through mechanical testing. Table 6.2 lists various types of E-glass lay-ups examined for their applicability as fiber reinforcement. Furthermore, numerous combinations of these materials have been assessed through numerical analysis and experimentation.

Table 6.1: Matrix Candidate Materials for Prototype Fabrication

Common Name		Composition / Ingredient Information
Resin	D.E.R. 330	Reaction Product of Epichlorohydrin and Bisphenol-A
	D.E.R. 332	Diglycidyl Ether of Bisphenol-A
	D.E.R. 732	Polymer of Epichlorohydrin-Polyglycol
Curing Agent	D.E.H. 20 (% by wt.)	Diethylenetriamine / Aminoethylpiperazine
		(98.5%-99.9% / 0.1%-1.5%)
	D.E.H. 39 (% by wt.)	Aminoethylpiperazine / Diethylenetriamine / Aminoethylpiperazine
		(96.5%-99.5% / 0.1%-2% / 1%)

Table 6.2: Candidate Fiber Materials for Prototype Fabrication

Fiberglass Configuraton	Description
Mesh	2.12 oz/sq yd., 9x9 mesh/in, alkali resistant
	4.30 oz/sq yd., 6x6 mesh/in
	common window screen
Cloth	0.72 oz/sq yd., 36x36 thread count
	3.2 oz/sq yd., 24x22 thread count
	0.55 oz/sq yd, 60x52 thread count

The relatively low target properties obtained from the material characterization of the loggerhead carapace significantly reduced the number of potential materials for the fabrication of the synthetic shell. Upon completion of an in-depth material search, a polyester resin with discontinuous e-glass fiber mesh reinforcement was chosen for construction of the synthetic carapace. A single ply of the composite was fabricated and harvested into 2.54 cm wide by 20.3 cm long samples. Each specimen underwent tensile testing identical to the biological carapace. Figure 6.1 gives an example of the load-extension plot created for each sample in an effort to illustrate the target property of force per unit width at failure. Stress verse strain curves were also developed for each sample in order to determine the tensile modulus, strain at failure, and ultimate tensile strength.

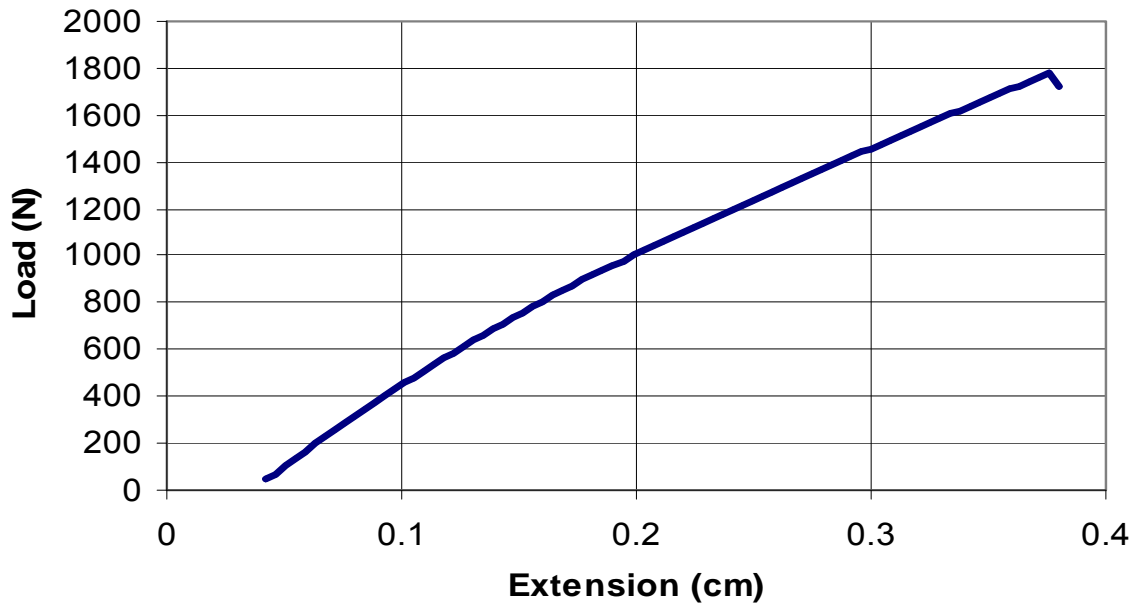


Figure 6.1: Load-Elongation Curve for Single-Ply Polyester / E-Glass Composite Sample

The average strain at failure of the composite samples was calculated to be 3.4%.

The average ultimate force per unit length of the single ply samples was determined to be 643 N/cm. This was significantly higher than the 408 N/cm mean corresponding to the organic carapace. However, it was necessary to test the synthetic samples in a manner identical to that of the real carapace in order to determine any geometrical and/or fabrication factors that may alter the tensile test results. Accomplishing this required the fabrication of a one-ply synthetic carapace prototype that was harvested for testing.

6.2 Evaluation of Prototype Fabrication Techniques

A variety of manufacturing techniques for fiber-reinforced polymer composite materials were reviewed including hand lay-up, injection molding, and vacuum bagging. The hand lay-up process, involving the manual application of resin, offers benefits associated with its adaptability by allowing for immediate design alterations. Conversely, it is time intensive as well as susceptible to irregularities and imperfections.

The injection molding process was also considered as a candidate for this application. One drawback to the process is the need for male and female tools to be constructed and fitted together during fabrication, eliminating the ability to adjust the thickness of the biomimetic shell. Upon completion of extensive experimentation with the vacuum bagging procedure, it was concluded that the process would be effective in producing high quality uniform results for the mass production of the finalized artificial carapace. However, the creation of numerous molds, required during the developmental phases, would be time consuming and expensive. Of the manufacturing procedures reviewed, hand layup was selected as the most advantageous for initial prototype fabrication. For this process, a mold must be fabricated in order to shape the prototype and mimic the geometry of the natural carapace.

6.3 Mold Fabrication

An additional biological shell was obtained from the Georgia Department of Natural Resources in order to be employed as a form for artificial shell fabrication. As seen in Figures 6.2 and 6.3, there was significant damage to the carapace. Consequently, the shell required repair prior to being used as the mold for shaping the composite material.



Figure 6.2: Initial Condition of the Carapace Employed as the Mold



Figure 6.3: Close-Up of Damage to Front Right Quadrant of the Shell

Before repairs could be performed, the layer of barnacles and decaying carapace had to be removed. The areas of the shell that were intact were feathered into the remainder of the carapace so as not to create an edge along the back of the shell. This was accomplished by sanding the edges until the back of the carapace was smooth. Once the

shell was prepared, several coats of fiberglass were applied to the damaged areas. The fiberglass strengthened the carapace and significantly decreased the likelihood of future damage. The patching can be seen in Figure 6.4.



Figure 6.4: Repair of Mold Top: Fiberglass mat and epoxy resin applied to repair the damaged carapace; Bottom: Close-up of repair

After the patching and preparatory work was completed, a commercially available automotive body filler was placed uniformly across the carapace. Nine intermediate coats were applied and sanded smooth. This created a uniform surface across the shell ideal for producing the carapace mold. The final mold can be seen in Figure 6.5.

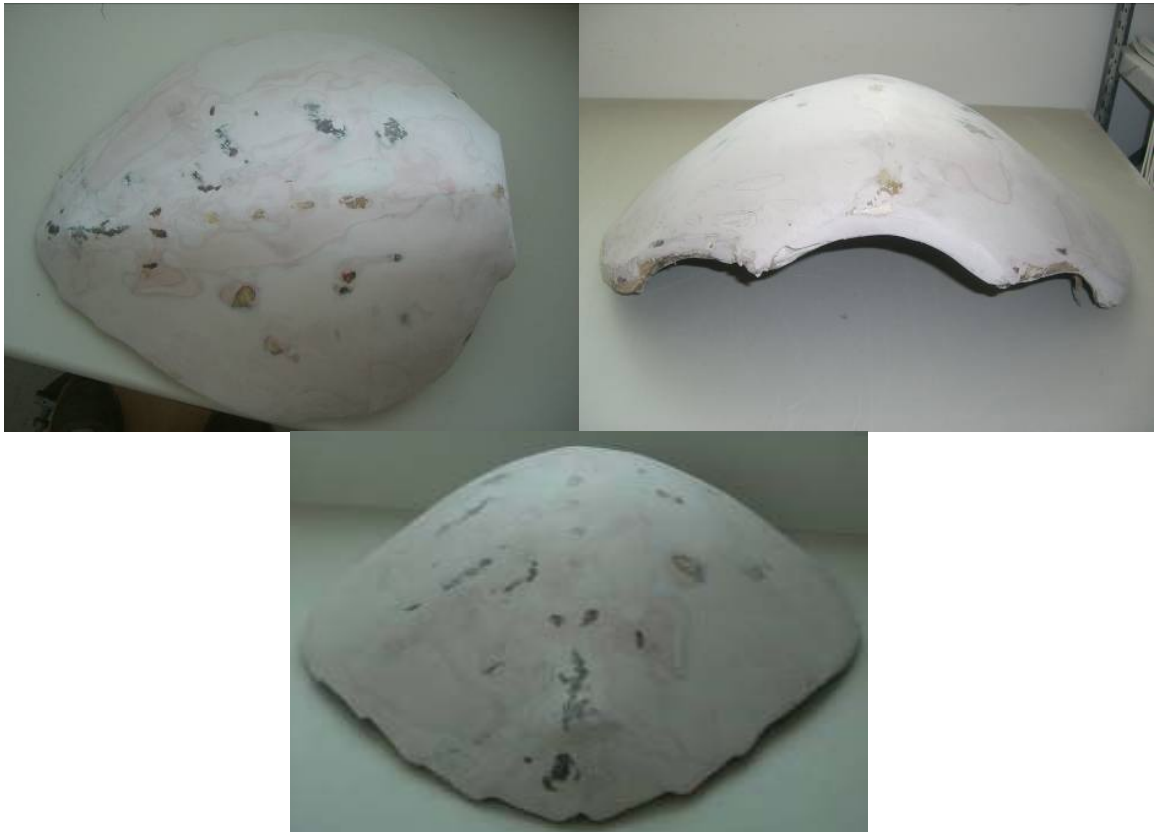


Figure 6.5: Completed Mold with Surface Leveling

6.4 Fabrication and Evaluation of Synthetic Carapace 1

The primary purpose for the creation of Synthetic Carapace 1 was to confirm that it was possible to construct a one-ply composite shell composed of a polyester resin matrix with discontinuous e-glass fiber mat reinforcement. In addition, coupon samples were harvested from the artificial shell in order to determine the tensile properties in an identical manner to that of the organic shell. The first step in fabrication is to cut the

fiberglass mat to match the geometry of the mold. The polyester resin is then mixed with a hardener and applied through brush and roller to the glass mat. Care was taken to ensure that no resin came into direct contact with the form in an effort to preserve it for future use. Once the glass fibers were saturated, the natural slope of the form allows for excess resin to drain from the edges of the mold. The composite was allowed to cure for 24 hours prior to painting. The paint was applied to illuminate the contours and any imperfections in the shell. Figure 6.6 shows the completed outer shell of Synthetic 1. For comparison, Figure 6.7 displays the shell adjacent to the biological mold.



Figure 6.6: Synthetic Carapace 1 (top view)



Figure 6.7: Comparison of Synthetic Carapace 1 and the Biological Mold

It was then necessary to fabricate a support structure that would increase the global rigidity of the artificial shell. The support system was designed to qualitatively model the ribs and spine of the organic carapace and gain insight into the additional rigidity these elements provided. In order to accomplish this, one inch wide strips of cardboard were inlaid into the synthetic shell, simulating the geometry of the biological rib system. The first cardboard strip was located at the center of the shell in the longitudinal direction. The following two strips spanning the carapace width were placed perpendicular to the first and equidistant from the center of the shell. It should be noted that the cardboard is only employed to form the shape of the composite and is assumed to have no impact on the flexural capacity of the prototype. Fiberglass mat was then cut to fit over the cardboard elements. Finally, the two part polyester resin was applied and allowed to solidify. Figure 6.8 shows the completed global support system attached to the synthetic shell.



Figure 6.8: Underside of Synthetic Carapace 1

Synthetic Carapace 1 was harvested into 2.54 cm wide samples in a manner identical to that of the biological shell. Excluding the effects of sample geometry, the longitudinal and transverse orientations of the composite material should not differ in tensile properties. For this reason, it was not deemed necessary to test the alternate directions separately. The tensile tests were performed utilizing the screw-type load frame as with previous testing. An example of the load-deformation curve produced for one sample is shown in Figure 6.9 and the remaining plots are given in Appendix H. A summary of the test results is given in Table 6.3. Stress versus strain curves were also developed for each sample in order to determine the tensile modulus, strain at failure, and ultimate tensile strength.

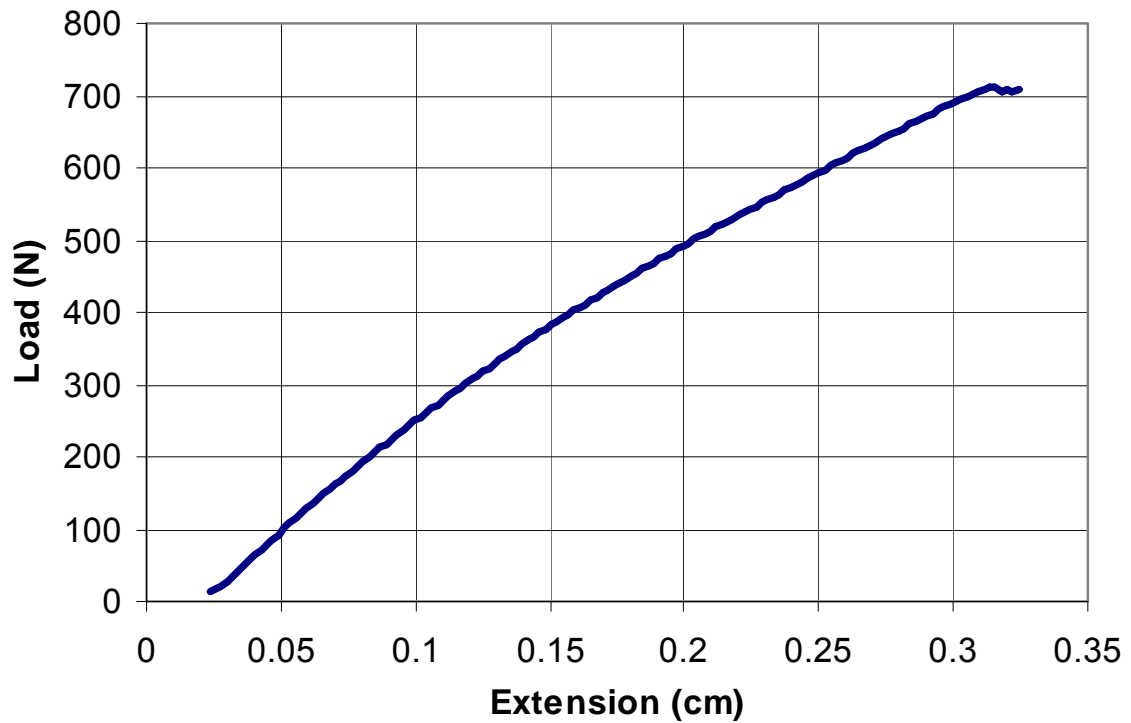


Figure 6.9: Load-Extension Curve for Sample 3, Synthetic Carapace 1

Table 6.3: Summary of Synthetic Carapace 1 Tensile Testing

Sample Designation	Ult Tensile Strength (kPa)	Modulus (MPa)	Strain at Failure	Ult. Force / Width (N/cm)
Synthetic 1	21200	1400	2.10%	215
Synthetic 2	24300	1480	2.45%	247
Synthetic 3	27600	1460	2.90%	280
Synthetic 4	27100	1580	2.90%	275
Synthetic 5	27500	1770	2.41%	279
Mean	25500	1540	2.55%	259
STD	2780	145	0.345%	28.3
COV	10.9%	9.41%	13.5%	10.9%

The properties of the artificial carapace and the target properties for the organic shell are displayed in Table 6.4 for comparison. It should be noted that the mean strain at failure of the synthetic carapace was within 10% of the biological samples. The force per unit width capacity, determined for the synthetic coupons, was found to be lower than the values obtained from the initial candidate material tests. This may be attributed to the

fact that the preliminary composite samples were formed on a flat plate, allowing the highly viscous polyester resin to collect on top of the glass fibers and increase the load capacity of the samples. In contrast, the excess matrix material applied to the steep sloping mold was permitted to flow off of the edges of the form. This indicates that no more resin than required to saturate the fibers was contained in each sample. A decrease in matrix material per unit area would result in a reduction of the force per unit length at failure. In addition, changes in geometry may have also contributed to the strength differences. However, the low rigidity of the samples did mitigate premature failure caused by curvature-induced moments.

Table 6.4: Comparison of Synthetic Carapace 1 Mean Properties and the Target Properties

Carapace	Ult. Force / Width (N/cm)	Strain at Failure	Modulus (MPa)
Biological	408	2.76%	312
Synthetic	259	2.55%	1540
% Error	36.5%	7.61%	79.7%

6.5 Fabrication and Evaluation of Synthetic Carapace 2

The test results of Synthetic Carapace 1 indicated that it would be necessary to increase the force per unit length capacity of the artificial carapace by 58%. An increase in the number of plies would result in excessive strength. Therefore, geometric alterations were mandatory in order to achieve the desired properties. In an effort to increase the strength in the longitudinal direction, elements with semicircular cross-sections were placed onto the mold. Each element possesses an arc length of approximately 4.00 cm over a width of 2.54 cm. The semicircular sections were constructed by bisecting a PVC pipe, with an inner diameter of 2.54 cm, through an angle

of 180°. The bisected pipe was then filled with modeling clay. Once shaped, the molded clay was removed from the pipe and placed parallel to the longitudinal direction of the carapace. Complications associated with forming the fiber mat to the intricate shape made it necessary to separate the clay elements by 1.3 cm increments. Once the mold retrofit was complete, the glass fiber mat and polyester resin were applied in the manner described for the fabrication of Synthetic Carapace 1. This is shown in Figure 6.10. Once the resin cured, the composite outer shell was removed from the mold. The isolated synthetic shell is shown in Figure 6.11.



Figure 6.10: Synthetic Carapace 2 Fabrication Process



Figure 6.11: Synthetic Carapace 2 Fully Cured and Removed from the Mold

In order to increase the transverse tensile strength and the global bending capacity of the carapace without altering the force necessary to penetrate the shell, a support system was constructed. The structure was qualitatively designed to closely mimic the natural geometry of the rib and spine members of the biological carapace. This was accomplished through the application of modeling clay. The clay was formed and inlaid into the concave side of the synthetic shell. Fiberglass mat was formed into strips and placed over the clay elements. The polyester resin was then applied and allowed to cure. Synthetic Carapace 2 is shown in Figure 6.12 with the support structure adhered to the underside of the shell.



Figure 6.12: Synthetic Carapace 2 with the Addition of the Faux Ribs

This manufacturing process requires the modeling clay to be contained within the finished carapace. The clay offers a negligible increase in bending and flexural strength and should not be considered as part of the structural system. However, due to the geometry of the sample and the inability of the clay to resist compressive loading, tensile testing of the harvested samples may result in an exaggerated elongation at failure. Finally, the composite shell was painted in order to enhance the visibility of the carapace in water (Figure 6.13). Figure 6.14 compares the underside of Synthetic Carapace 2 to that of the organic carapace.



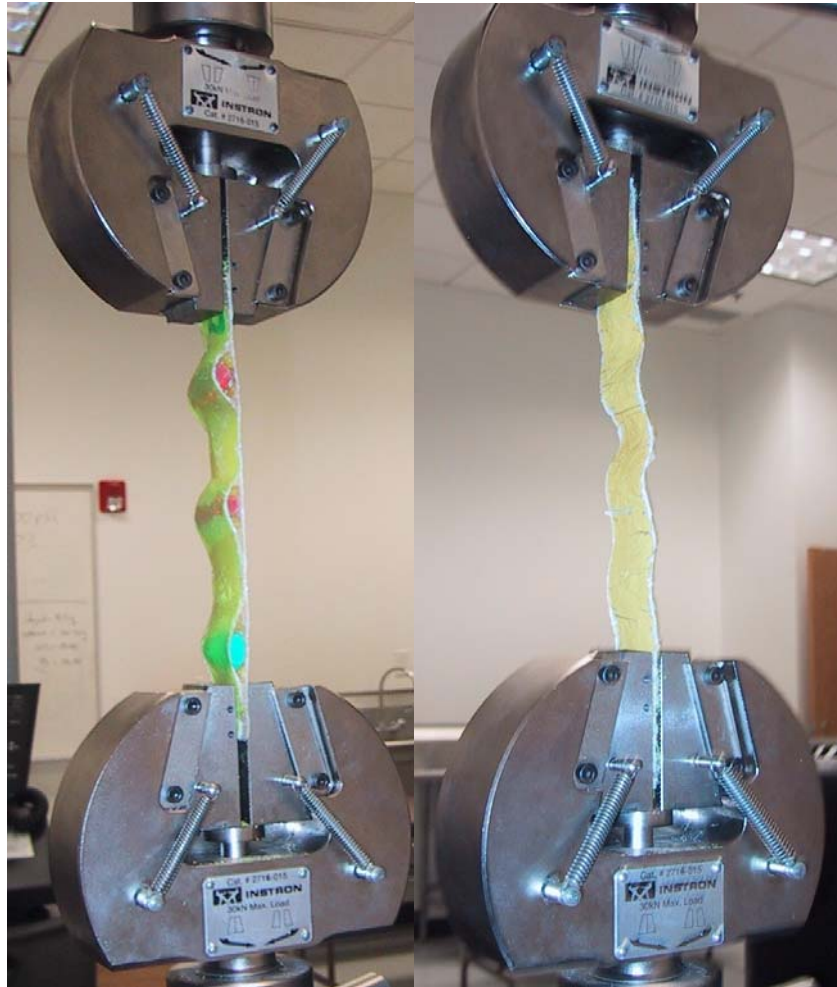
Figure 6.13: Completed Synthetic Carapace 2



Figure 6.14: Comparison of the Underside of the Natural and Synthetic Shell

The clay elements used to create the fluted surface of Synthetic Carapace 2 were oriented in the longitudinal direction only. Therefore, the tensile properties in the longitudinal and transverse directions will vary and must be tested separately. The

artificial carapace was harvested in a manner identical to the biological shell resulting in 2.54 cm wide samples for both orientations. It should be noted that the thickness of the samples varied due to the additional composite material at locations adjacent to the faux ribs. Figure 6.15 shows the testing of typical longitudinal and transverse samples.



**Figures 6.15: Tensile Testing of Synthetic Carapace 2 Coupons;
The left and right photographs show the testing of typical longitudinal
and transverse samples respectively**

The irregular geometry observed in the longitudinal specimen is due to the presence of artificial rib segments. The sinusoidal curvature associated with the transverse sample is due to the fluted sections oriented orthogonal to their length.

Each sample harvested was subjected to a tension test following the procedures outlined for the organic carapace. As with previous testing, load versus extension and stress versus strain plots were generated for each specimen. Figure 6.16 displays results from the testing of a longitudinal sample. Similarly, Figure 6.17 shows results from a sample harvested in the transverse direction.

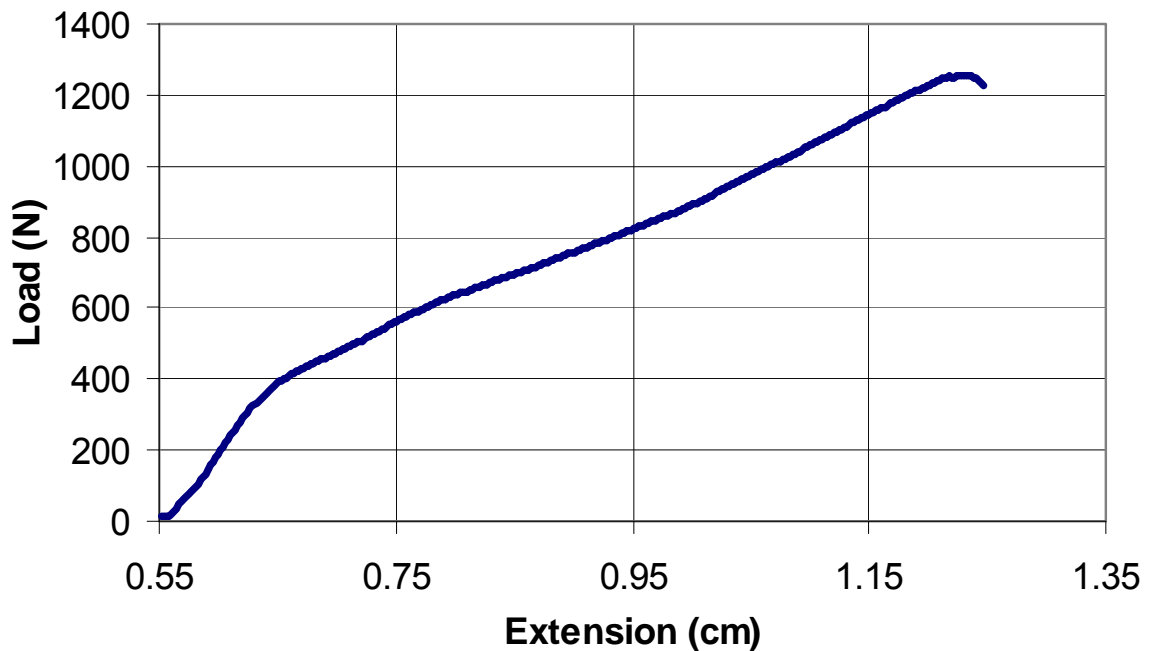


Figure 6.16: Load-Extension Curve for Longitudinal Sample 4, Synthetic Carapace 2

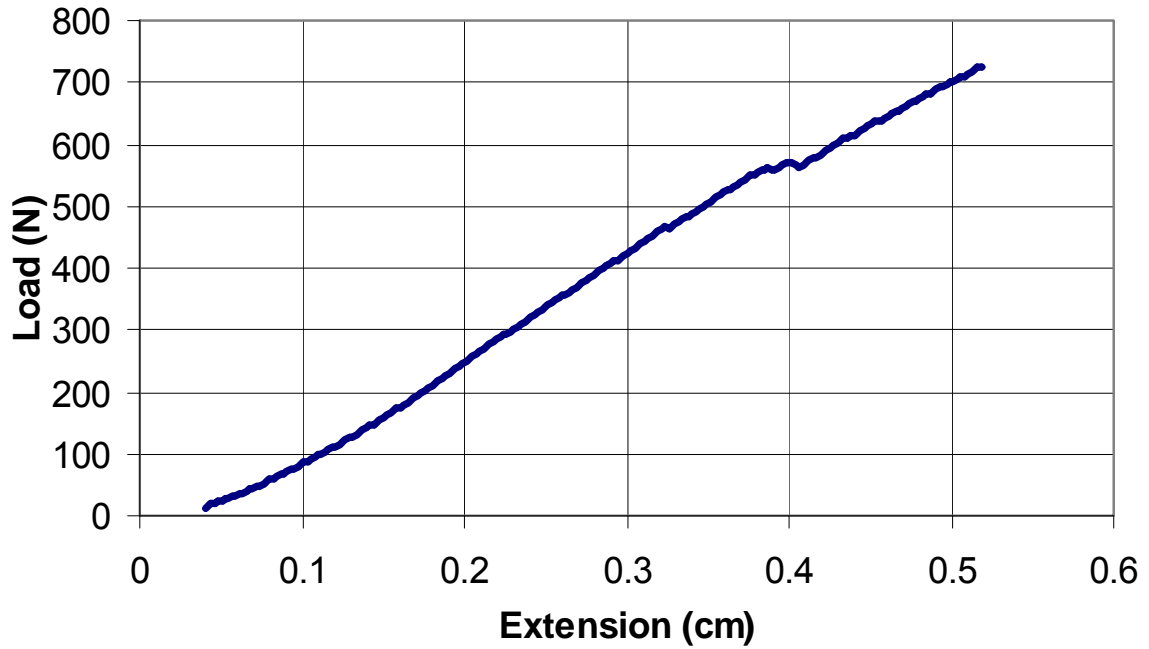


Figure 6.17: Load-Extension Curve for Transverse Sample 1, Synthetic Carapace 2

Load versus extension plots for each of the samples harvested from Synthetic Carapace 2 are given in Appendix I. A summary of the tensile test results for the longitudinal samples obtained from Synthetic Carapace 2 are given in Table 6.5. This is followed by Table 6.6 which summarizes the test results for the transversely harvested coupons.

Table 6.5: Summary of Synthetic Carapace 2 Longitudinal Tensile Testing

Sample Designation	Ult Tensile Strength (kPa)	Modulus (MPa)	Strain at Failure	Ult. Force / Width (N/cm)
Synthetic 1	39600	1250	6.52%	403
Synthetic 2	23100	1250	4.51%	470
Synthetic 3	25400	1780	4.30%	463
Synthetic 4	24300	1290	8.21%	494
Synthetic 5	42200	2560	2.69%	429
Mean	30900	1630	5.25%	452
STD	9190	568	2.14%	35.9
COV	29.7%	34.9%	40.9%	7.94%

Table 6.6: Summary of Synthetic Carapace 2 Transverse Tensile Testing

Sample Designation	Ult Tensile Strength (kPa)	Modulus (MPa)	Strain at Failure	Ult. Force / Width (N/cm)
Synthetic 1	14100	509	3.50%	286
Synthetic 2	20600	550	5.31%	303
Synthetic 3	22800	532	6.85%	232
Synthetic 4	12600	390	4.20%	256
Synthetic 5	33100	490	9.25%	336
Mean	20600	494	5.82%	283
STD	8160	62.5	2.30%	40.5
COV	39.6%	12.7%	39.4%	14.3%

The mean material properties obtained from Synthetic Carapace 2 for the longitudinal direction are displayed along side the target tensile material properties in Table 6.7 for comparison. This is repeated for the transverse direction in Table 6.8.

Table 6.7: Comparison of Synthetic Carapace 2 Mean Longitudinal Properties and the Target Tensile Properties

Carapace	Ult. Force / Width (N/cm)	Strain at Failure	Modulus (MPa)
Biological	408	2.76%	312
Synthetic Longitudinal	452	5.25%	1620
% Error	9.73%	47.4%	80.7%

Table 6.8: Comparison of Synthetic Carapace 2 Mean Transverse Properties and the Target Tensile Properties

Carapace	Ult. Force / Width (N/cm)	Strain at Failure	Modulus (MPa)
Biological	408	2.76%	312
Synthetic Transverse	283	5.82%	494
% Error	30.6%	52.6%	36.8%

The longitudinal ultimate force per unit width of Synthetic Carapace 2 is within 10% of the target material property. Conversely, strain at failure for both orientations deviated

significantly from the desired value when compared to Synthetic Carapace 1. This can be attributed to geometrical effects and inaccurately represents the localized properties of the material. The sinusoidal curvature of the transverse samples and the rib elements located in the longitudinal specimens allowed for increased elongation under relatively low stresses. In effect, stress and strain values were altered. Analysis of global properties will be necessary to evaluate the effects of the local curvature on the elongation at failure of the intact shell.

6.6 Production Methodology

In order to fabricate a sufficient quantity of artificial carapaces to effectively evaluate all relevant mortality mitigation options, multiple forms would be constructed from the organic mold utilized in prototype fabrication. The hand lay-up process will be implemented to create multi-ply composite shells identical in geometry to the organic carapace. The forms will have sufficient rigidity to prevent deformation during the fabrication process. To facilitate the construction of the spine and rib support structure, composite female molds would be made in a manner similar to that of the outer shell. The female molds would be formed by employing modeling clay to construct the desired shape of the composite cast. The resulting mold will then be used as a press to quickly shape the clay and accurately cut the fiber glass mat. It would be possible to fabricate multiple carapaces simultaneously over a forty-eight hour period. Processes similar to those utilized in prototype construction will be employed. The outer shells of the carapace will be created on the first day and permitted to cure overnight. This process

would be repeated for the support structure inside the freshly produced shell on the second day. The synthetic shells would be suitable for testing on day 3.

Chapter 7

Conclusions

This research was conducted in order to aid the development of an artificial biomimetic carapace capable of simulating the material properties of the loggerhead carapace in the event of a boat strike. The goals of this study included the development of experimental testing procedures designed to evaluate pertinent material properties of the loggerhead shell and the fabrication, and evaluation of a prototype artificial carapace. This section outlines the conclusions developed throughout the duration of this research and offers recommendations for continuing studies.

7.1 Conclusions

Through the review of the photographic database supplied by the Georgia Department of Natural Resources, the primary impact locations and failure mechanisms of loggerhead sea turtles subjected to boat strikes were categorized. The most common mode of injury was determined to be skeg impact, with 44% of the sea turtles reviewed displaying signs of this form of damage. In addition, it was determined that the majority of injuries occur along the center third of the carapace length, measured parallel to the spine, with a frequency of 74%. This information was used to determine the primary regions of concern for the material characterization. In addition, understanding the principal sources and types of damage will aid in the future development of effective mortality mitigation options.

It was necessary to develop test methods for evaluating the tensile and flexural properties of the loggerhead carapace as no accepted standards existed. The flexural testing was similar to the ASTM standards employed as references. However, the tensile test required the development of specialized tabs in order to obtain reproducible results while mitigating premature failure due to the irregular geometry of the coupons. This procedure is outlined in Appendix G and is the result of knowledge acquired during the review of previous work, experience obtained while evaluating the loggerhead carapace, and post-processing of the measured data. Although the test method is specific to the sea turtle carapace, it may offer insight into procedures for evaluating alternate forms of rigid and/or curved biological materials. The specialized tabs were successful in reducing the curvature-induced moments at the grips. However, they do not completely remove the effects of bending on the sample.

The results of the tensile testing of the biological shell revealed that the material properties were similar in the longitudinal and transverse directions with a 12.2% difference in tensile strength, a 10.7% difference in strain at failure, and a 10.1% difference in the modulus of elasticity. Conversely, the three-point bending test results indicated that the flexural properties differed significantly in the longitudinal and transverse orientations due to localized regions of weak tissue running transversely through the shell. The modulus of rupture and the bending modulus for the middle transverse samples were determined to be approximately four times greater than those found for the middle longitudinal samples. This increases the intricacy of the biomimetic shell design by forcing the two directions to be addressed separately.

For this investigation, prototype shells were fabricated to simulate the tensile properties of the biological shell. Selecting constituents suitable for replicating the tensile properties of the loggerhead carapace proved complex due to the low strength and strain at failure of the organic material. Upon completion of a parametric study comparing the ultimate strength to various geometric ratios, it was concluded that the thickness of the coupons did not have a significant impact on the strength of the sample. This permitted the use of force per unit length at failure as a target property in place of ultimate strength. As a result, high strength materials may be evaluated at minimal thickness in order to reduce the force required to induce failure.

After the review of numerous constituents at varying proportions, a polyester resin with discontinuous E-glass fiber mesh reinforcement was selected for the synthetic shell fabrication. Synthetic Carapace 1 simulated the strain at failure of the organic shell to within 8%. However, force per unit length at failure differed by 37%. Localized geometric modifications were employed for Synthetic Carapace 2 resulting in successful replication of force per unit length to within 10% of the organic shell. This was accomplished without modifying the constituent proportions or ply thickness of the composite. This study represents the initial steps toward the creation of a synthetic shell that will successfully mimic the relevant properties of the loggerhead carapace during boat strike incidents.

7.2 Recommendations for Continuing Testing

Additional research is required in order to fully develop a functional biomimetic loggerhead carapace. At present, two loggerhead shells have been harvested and tested in

order to determine target tensile properties for the prototype biomimetic shell and only one carapace has been evaluated in flexure. A continuation of this study is recommended. Further tensile and flexural testing is required in order to refine the target material properties and reduce the coefficients of variation for each data set. In addition, there is uncertainty associated with the effects of biological decay, diet, and age on the material properties of the carapace. Associating time of death, food sources, and age to each carapace tested may offer insight into how these factors alter the mechanical behavior of the shell.

Faux rib and spine elements were aesthetically designed for the artificial shells. These elements significantly increased the global rigidity of the prototypes. This indicates that the ribs and spine of the loggerhead have a significant impact on the global behavior of the shell and their properties should be determined and simulated in order to ensure that the global behavior of the intact carapace is mimicked.

Impact testing is also critical for the development of an effective biomimetic shell. A drop weight impact tester with traditional blunt impact tips would be ideal for evaluating biological coupons and prototype candidate materials. In addition, the test may be conducted on intact synthetic and biological shells with modified impact tips that simulate the geometry of a skeg. This would aid in determining efficacy of the biomimetic shell to simulate the global properties of the loggerhead carapace in the event of a boat strike.

Once the relevant material properties are simulated, field testing with the completed biomimetic shell may be conducted in riverine and estuary environments. Various mortality mitigation options should be investigated. Prop guards, prop cages, and ring

props are a few of the commercially available products that may prove effective in minimizing the number of loggerhead deaths attributed to boat strikes. Various boat speeds should also be studied in combination with each of the mortality mitigation options.

Appendix A

Tensile Stress-Strain Plots – Carapace 1

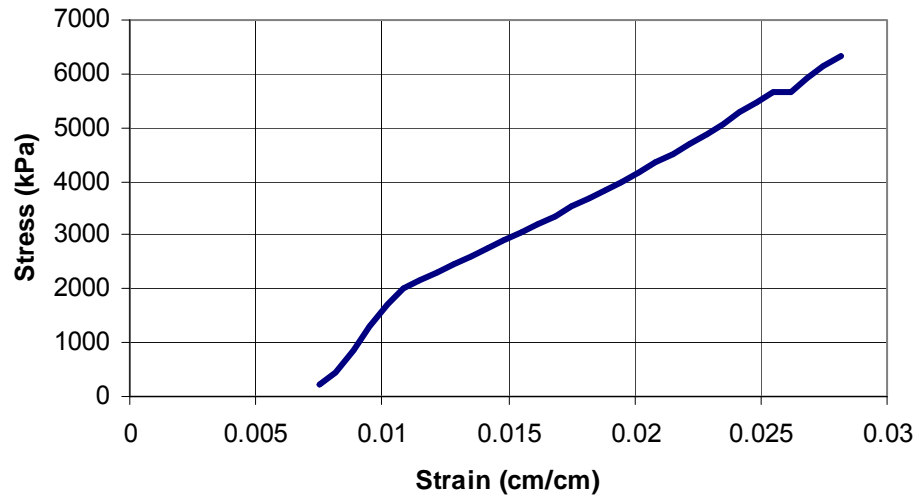


Figure A.1: Stress vs. Strain Plot of Sample ML1 Obtained from Carapace 1

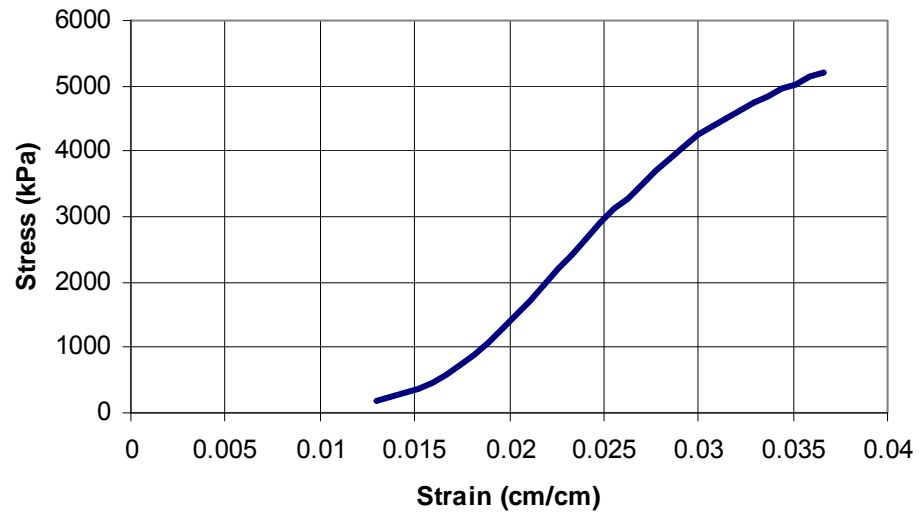


Figure A.2: Stress vs. Strain Plot of Sample ML2 Obtained from Carapace 1

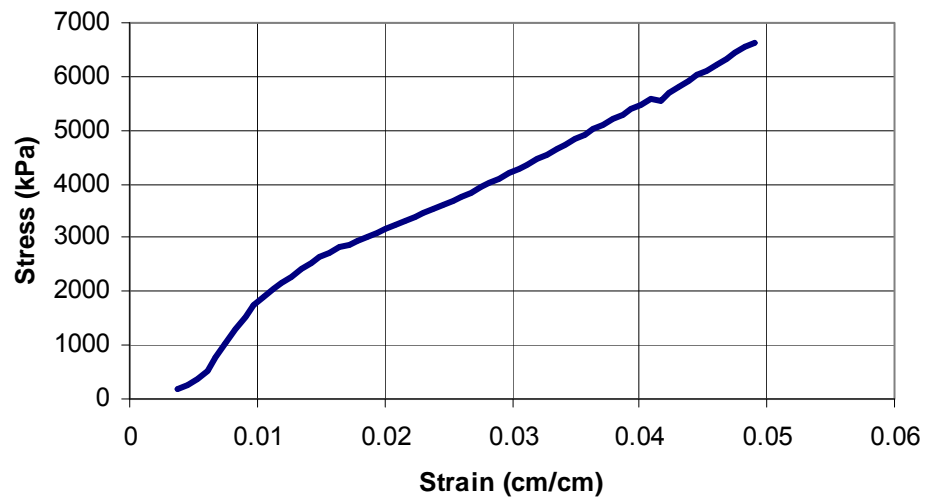


Figure A.3: Stress vs. Strain Plot of Sample ML5 Obtained from Carapace 1

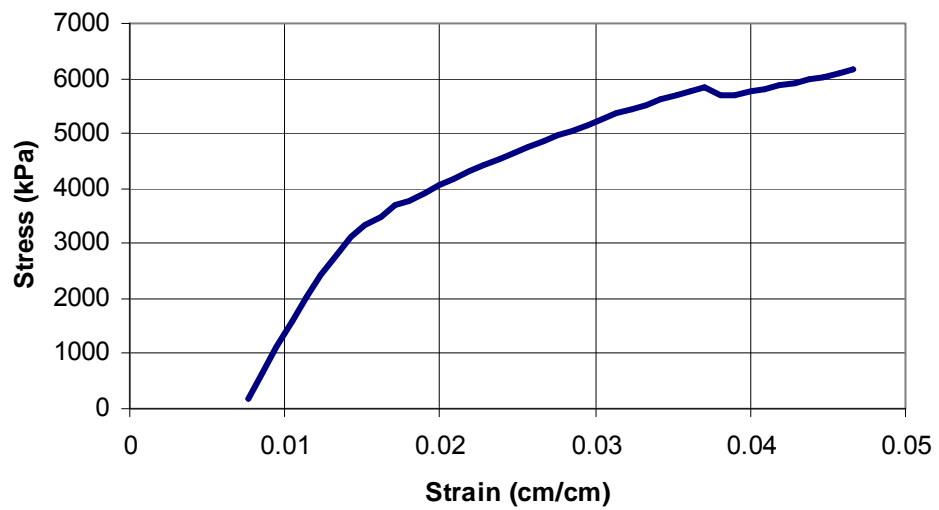


Figure A.4: Stress vs. Strain Plot of Sample ML6 Obtained from Carapace 1

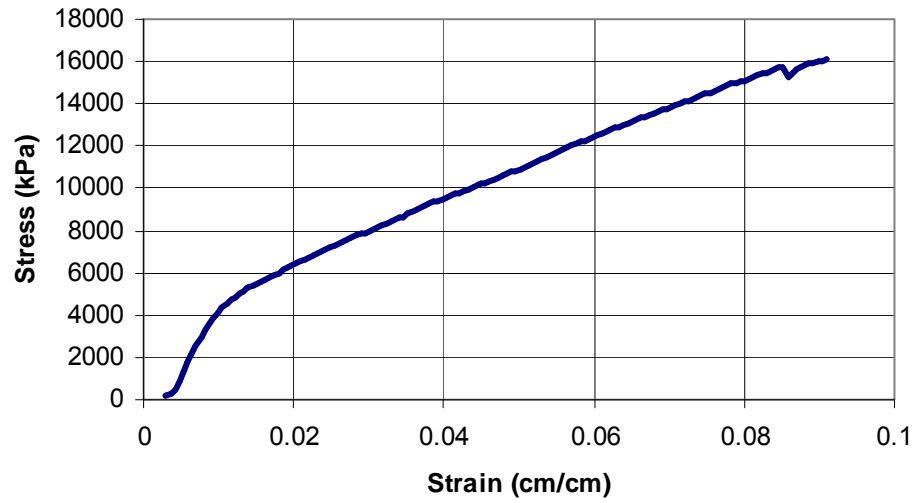


Figure A.5: Stress vs. Strain Plot of Sample MT1 Obtained from Carapace 1

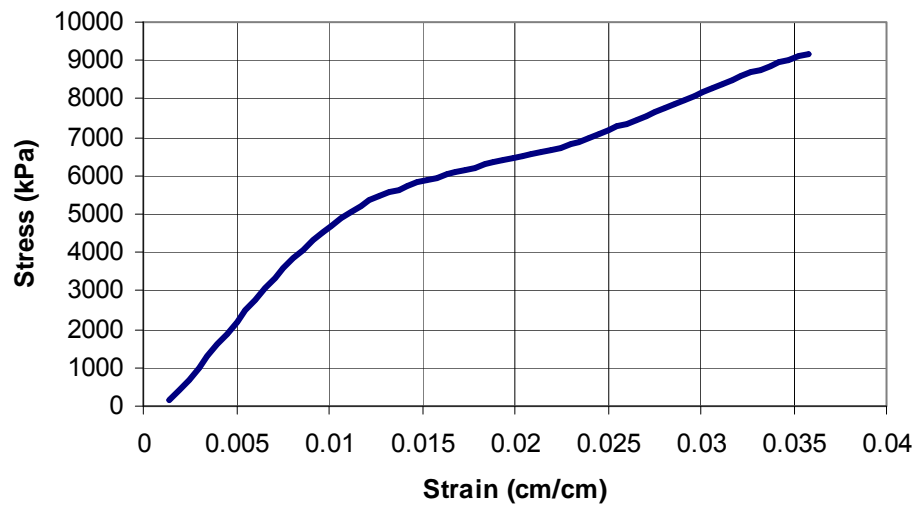


Figure A.6: Stress vs. Strain Plot of Sample MT2 Obtained from Carapace 1

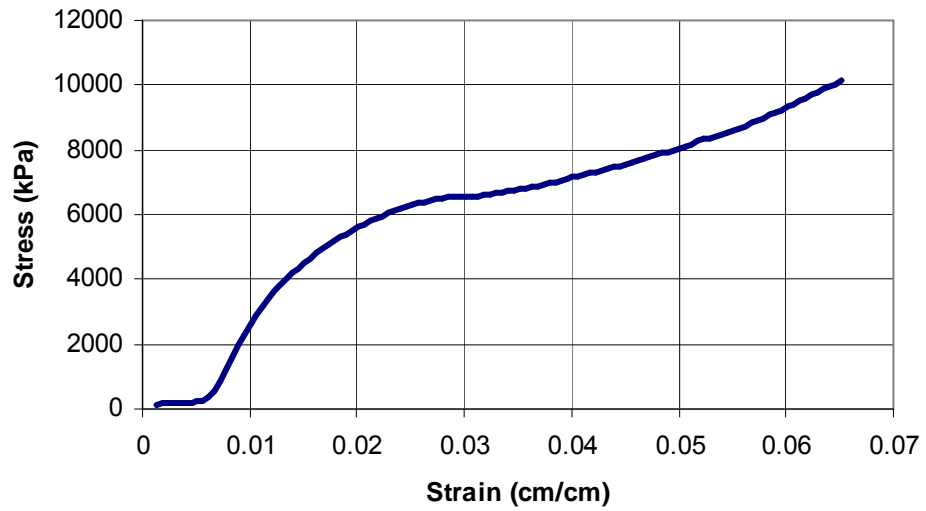


Figure A.7: Stress vs. Strain Plot of Sample MT3 Obtained from Carapace 1

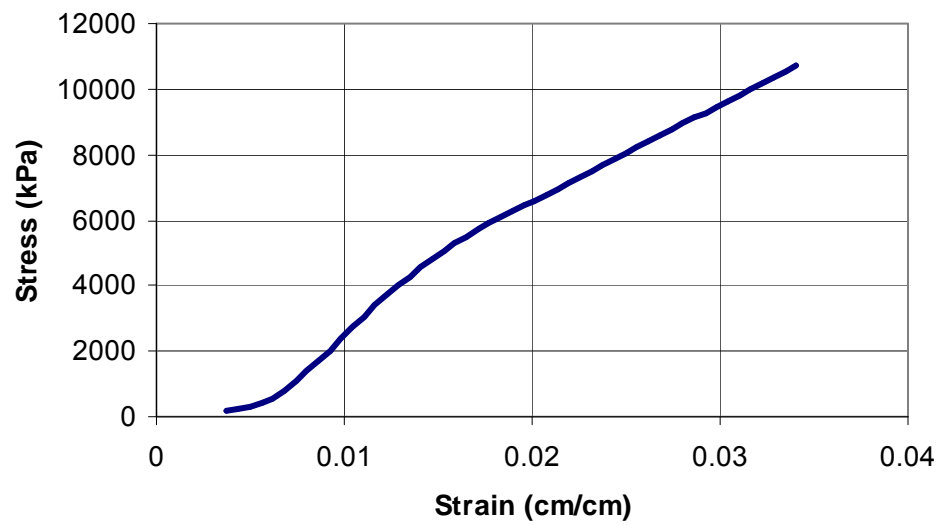


Figure A.8: Stress vs. Strain Plot of Sample MT4 Obtained from Carapace 1

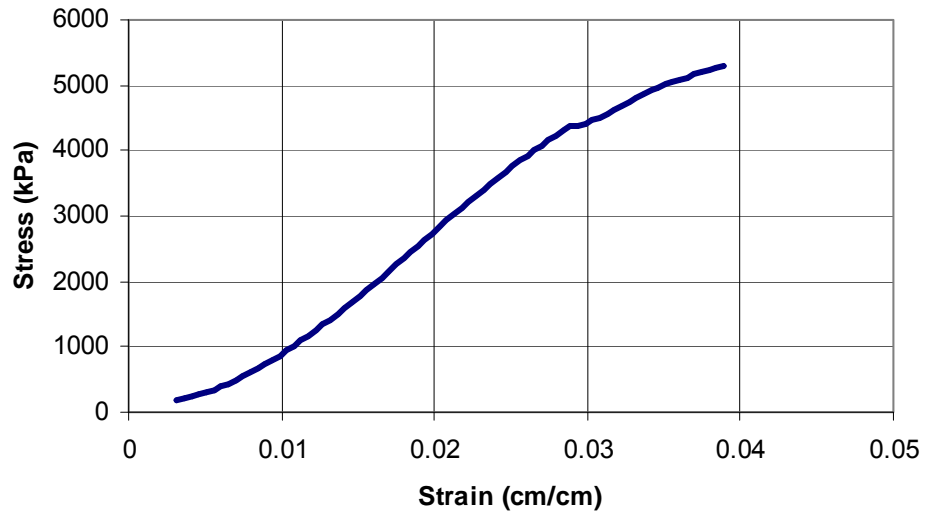


Figure A.9: Stress vs. Strain Plot of Sample MT5 Obtained from Carapace 1

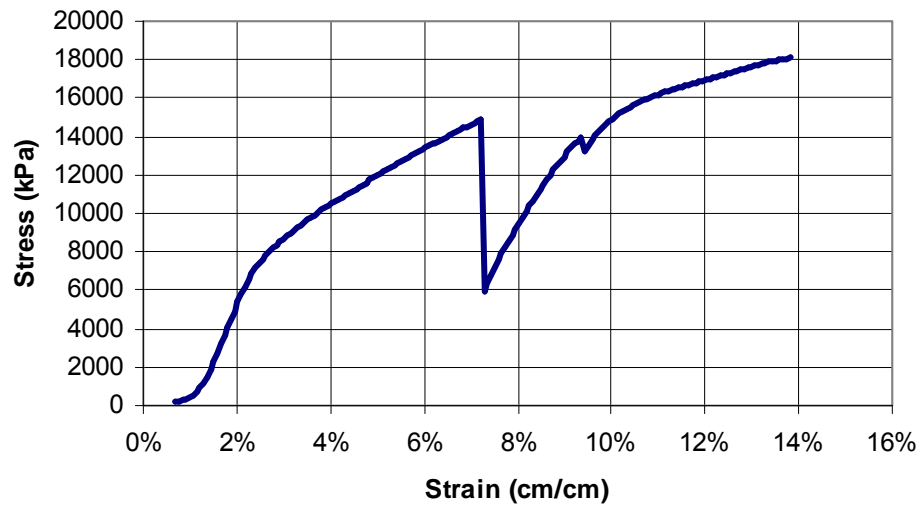


Figure A.10: Stress vs. Strain Plot of Sample FT1 Obtained from Carapace 1
The sample was not included in average property calculations due to the outlying strain value and abnormal reaction to loading.

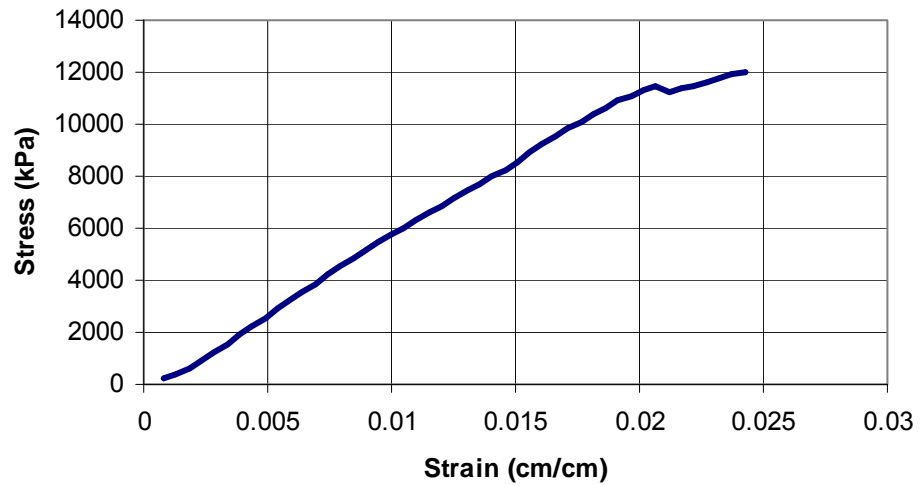


Figure A.11: Stress vs. Strain Plot of Sample FT2 Obtained from Carapace 1.

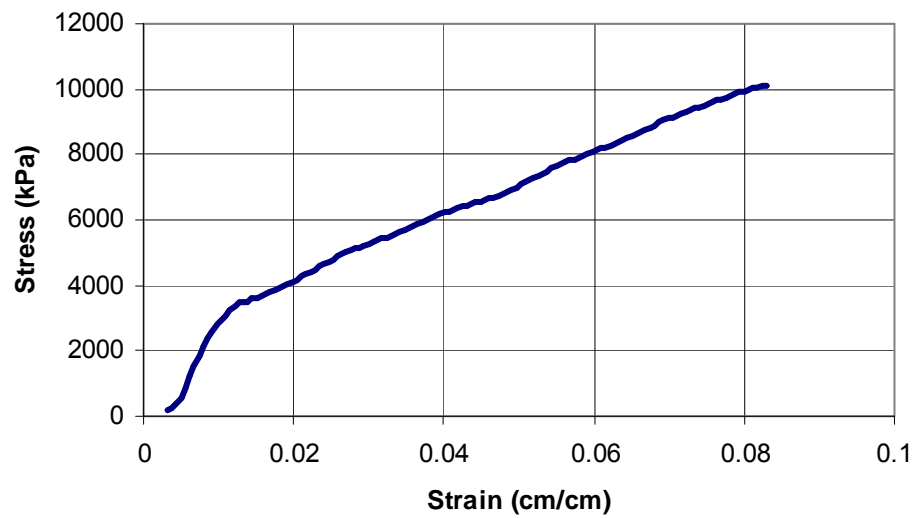


Figure A.12: Stress vs. Strain Plot of Sample FT3 Obtained from Carapace 1

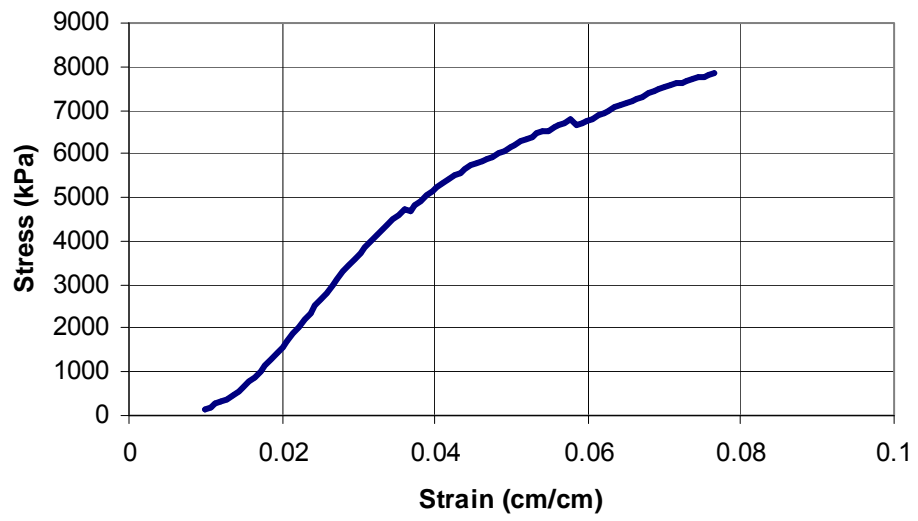


Figure A.13: Stress vs. Strain Plot of Sample FT4 Obtained from Carapace 1

Appendix B

Tensile Stress-Strain Plots – Carapace 2

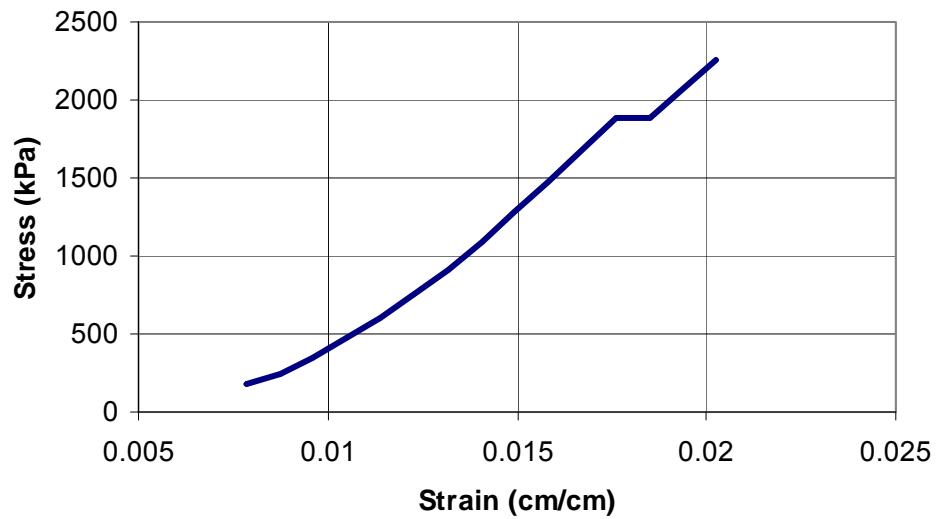


Figure B.1: Stress vs. Strain Plot of Sample FL1 Obtained from Carapace 2

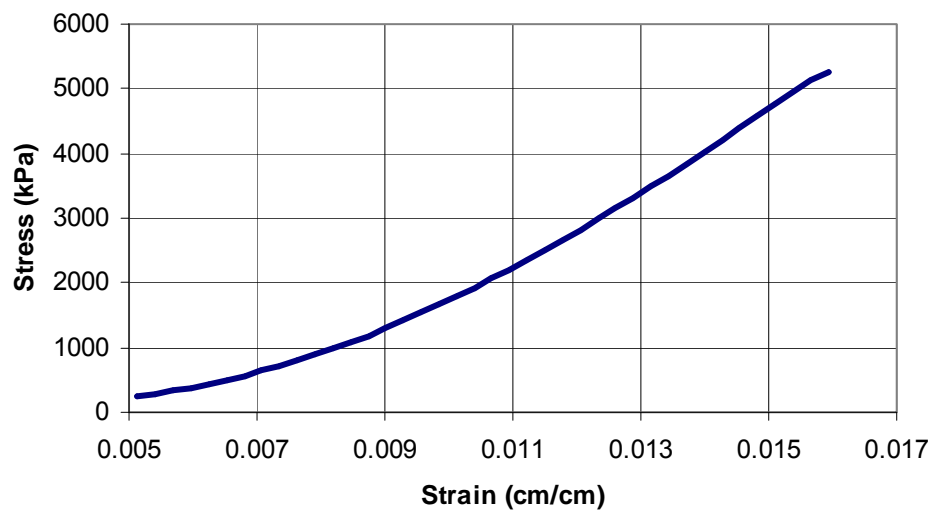


Figure B.2: Stress vs. Strain Plot of Sample FL3 Obtained from Carapace 2

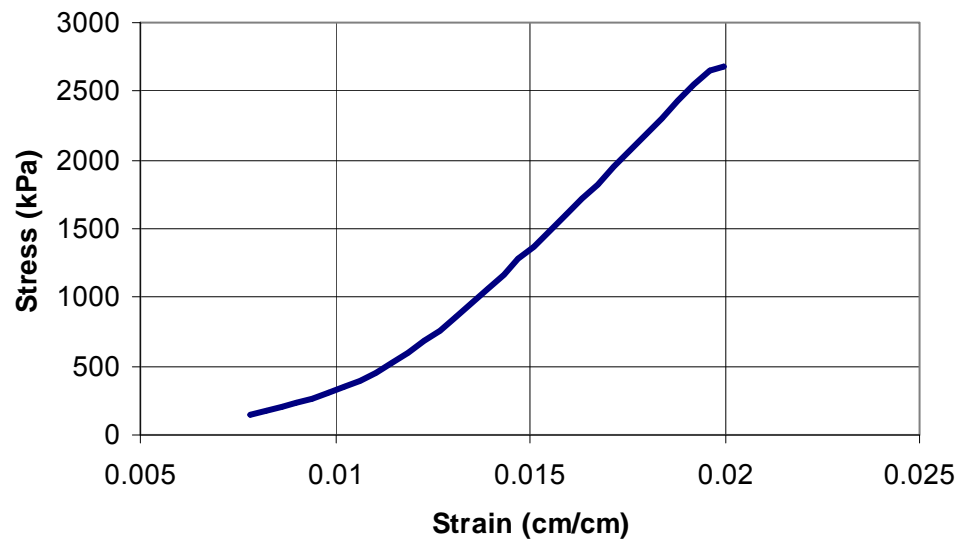


Figure B.3: Stress vs. Strain Plot of Sample FL4 Obtained from Carapace 2

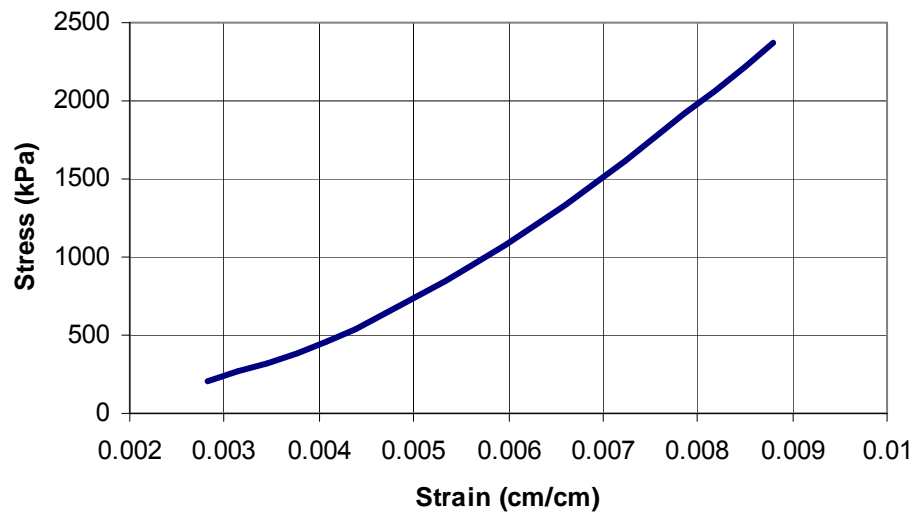


Figure B.4: Stress vs. Strain Plot of Sample FL5 Obtained from Carapace 2

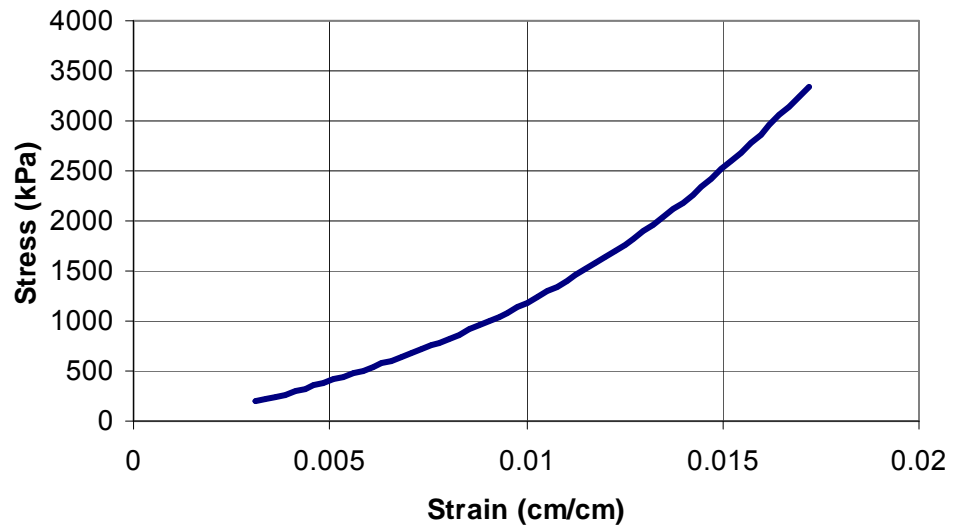


Figure B.5: Stress vs. Strain Plot of Sample FT3 Obtained from Carapace 2

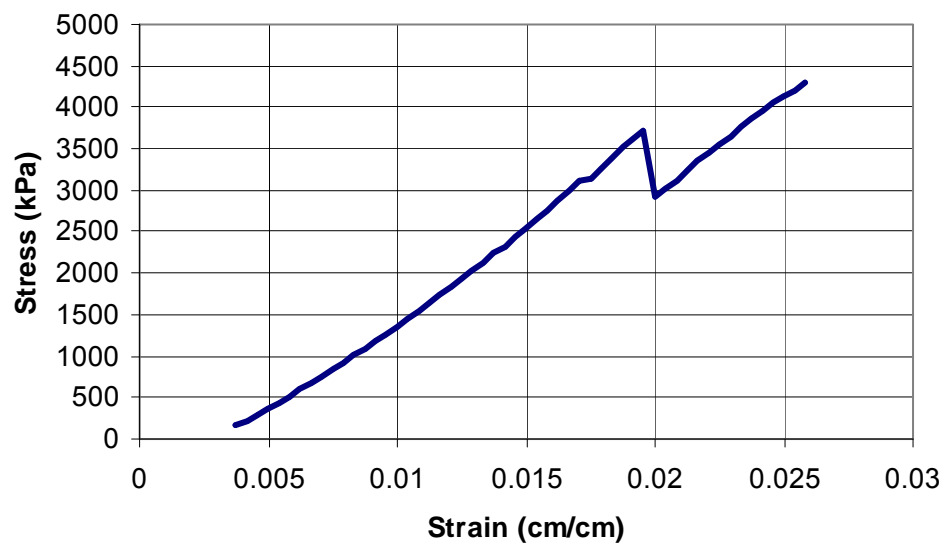


Figure B.6: Stress vs. Strain Plot of Sample FT5 Obtained from Carapace 2

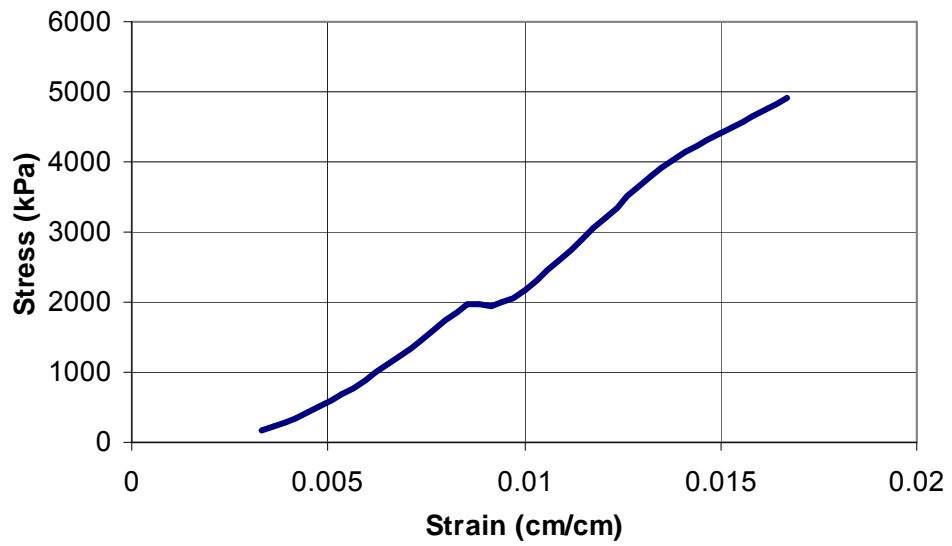


Figure B.7: Stress vs. Strain Plot of Sample FT6 Obtained from Carapace 2

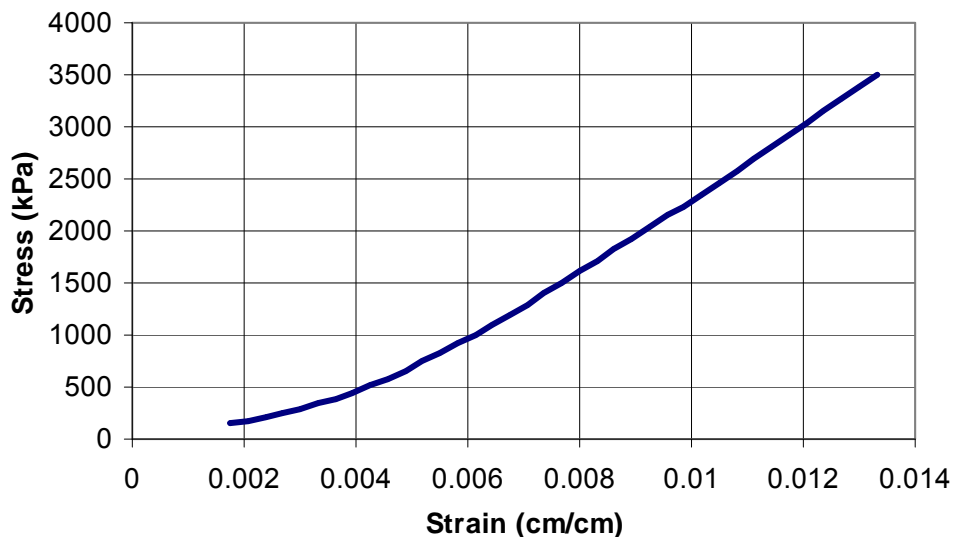


Figure B.8: Stress vs. Strain Plot of Sample FT8 Obtained from Carapace 2

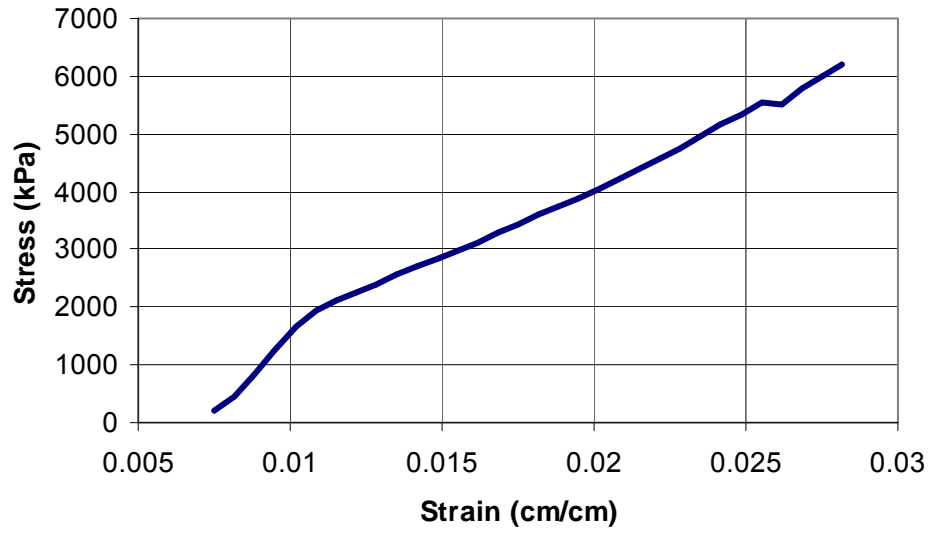


Figure B.9: Stress vs. Strain Plot of Sample ML1 Obtained from Carapace 2

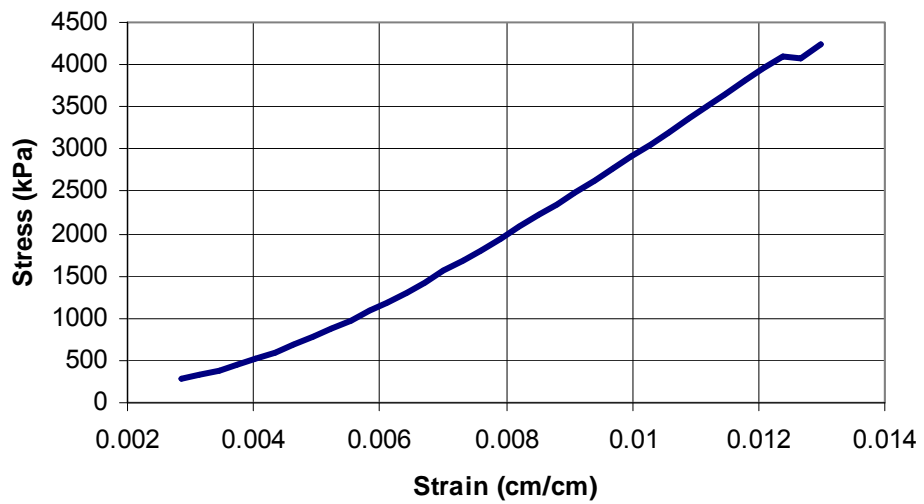


Figure B.10: Stress vs. Strain Plot of Sample ML2 Obtained from Carapace 2

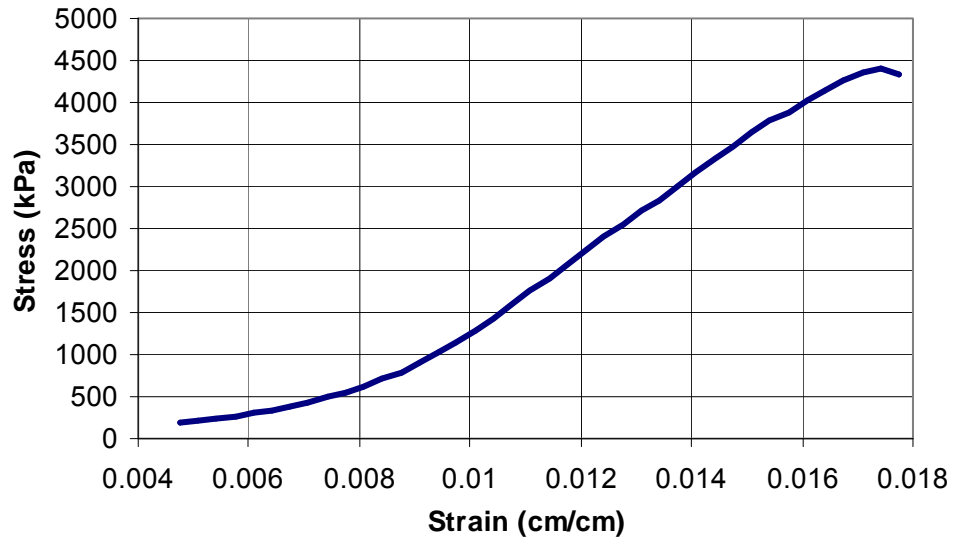


Figure B.11: Stress vs. Strain Plot of Sample ML4 Obtained from Carapace 2

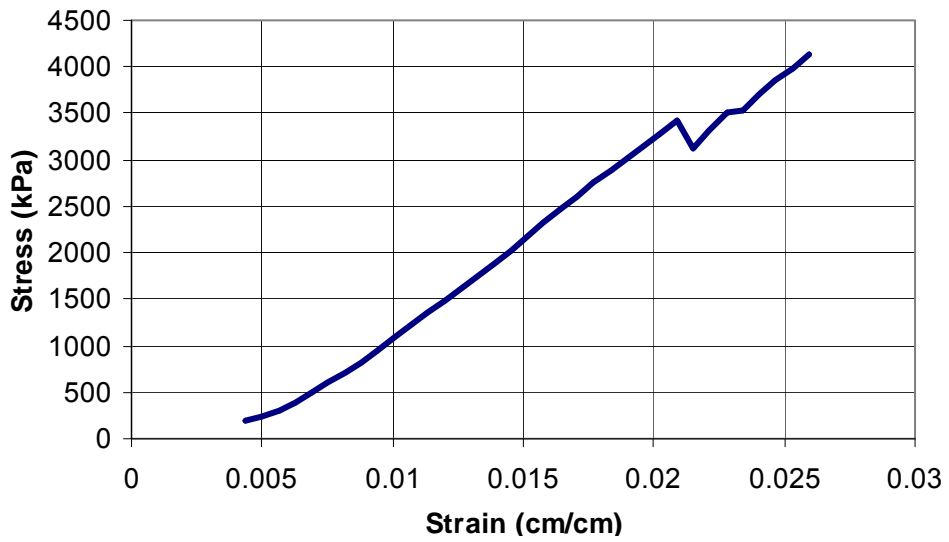


Figure B.12: Stress vs. Strain Plot of Sample ML5 Obtained from Carapace 2

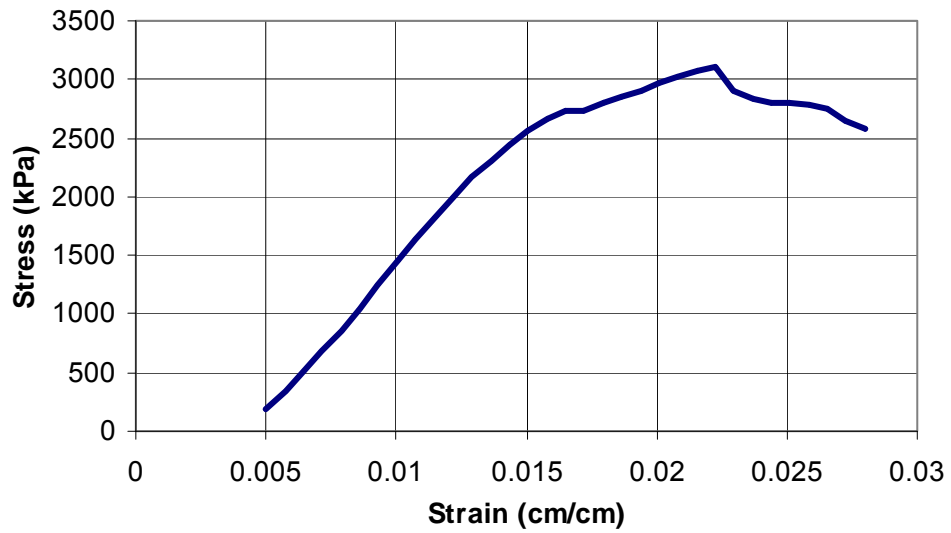


Figure B.13: Stress vs. Strain Plot of Sample ML6 Obtained from Carapace 2

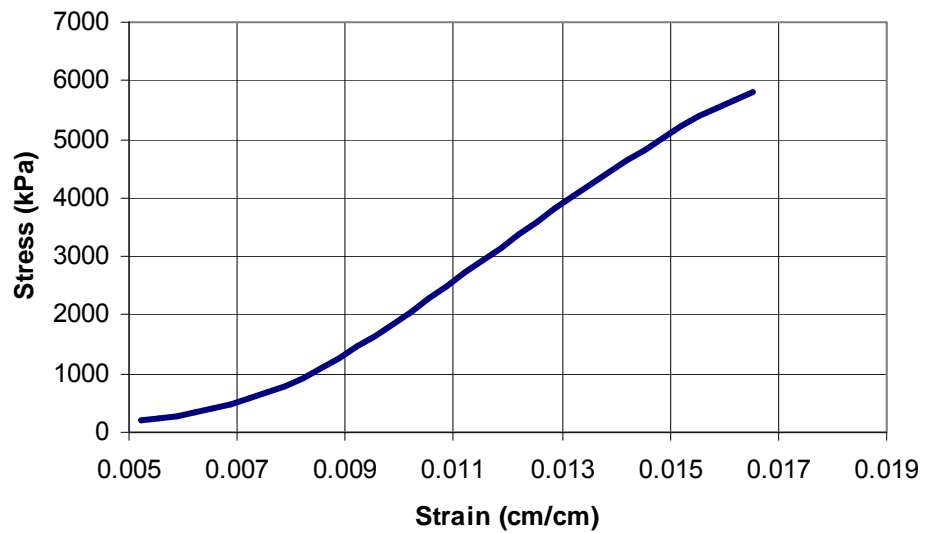


Figure B.14: Stress vs. Strain Plot of Sample ML7 Obtained from Carapace 2

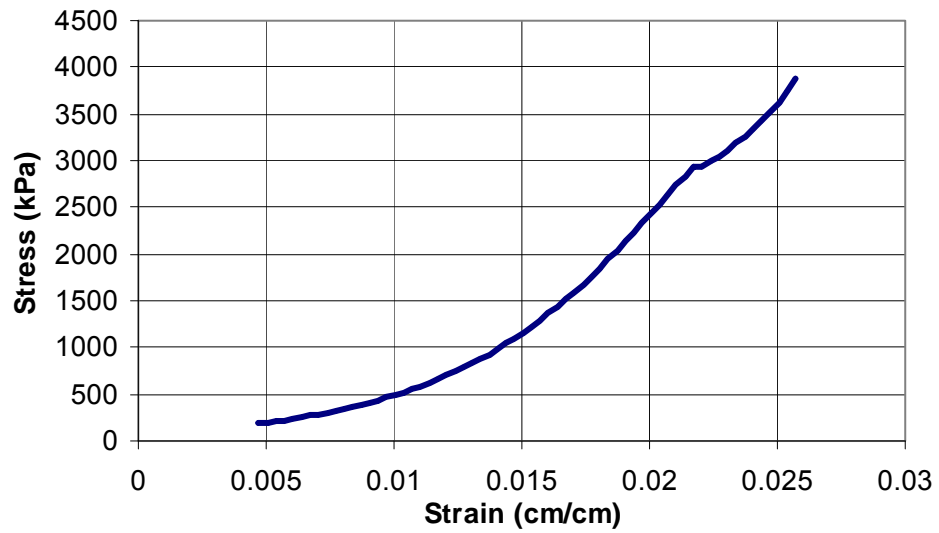


Figure B.15: Stress vs. Strain Plot of Sample MT1 Obtained from Carapace 2

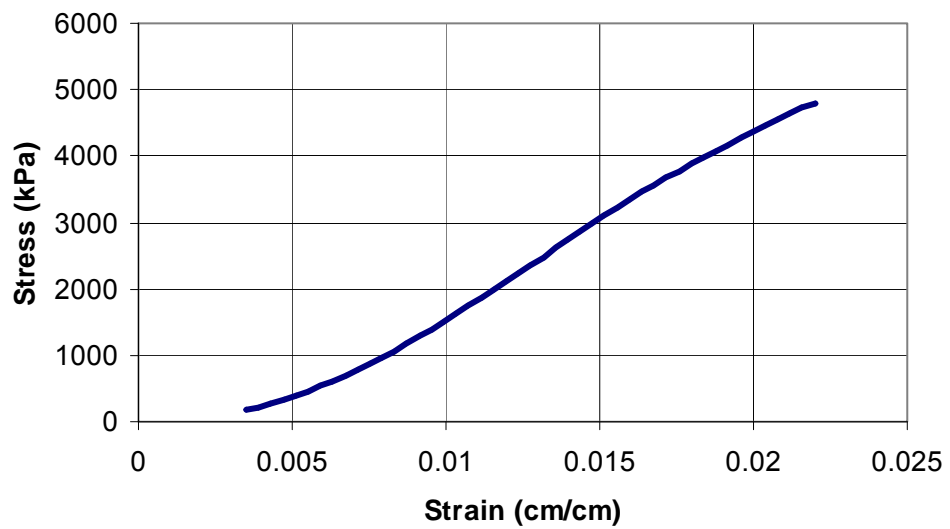


Figure B.16: Stress vs. Strain Plot of Sample MT3 Obtained from Carapace 2

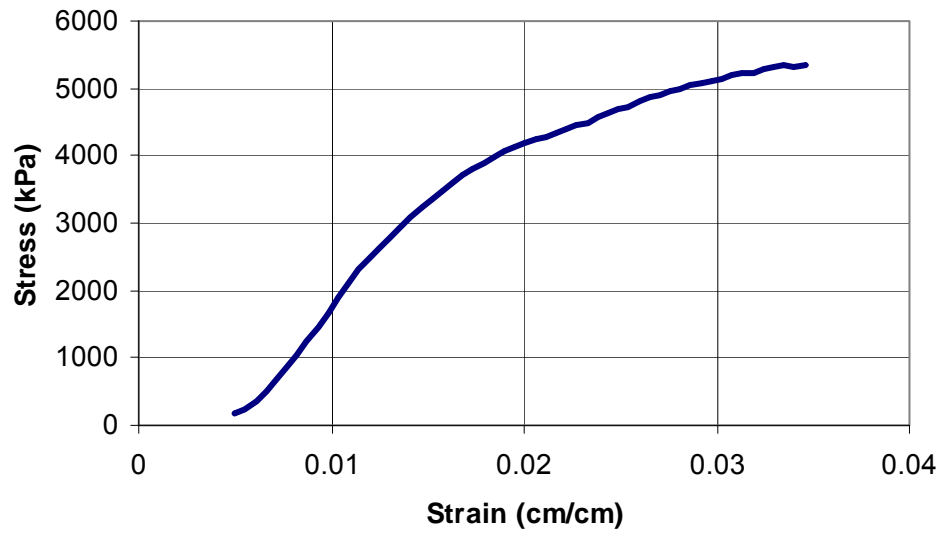


Figure B.17: Stress vs. Strain Plot of Sample MT4 Obtained from Carapace 2

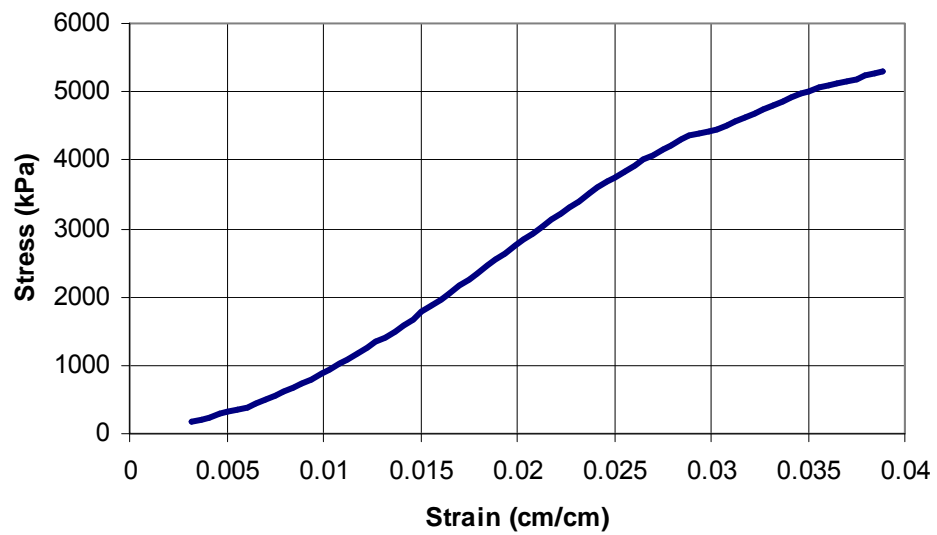


Figure B.18: Stress vs. Strain Plot of Sample MT5 Obtained from Carapace 2

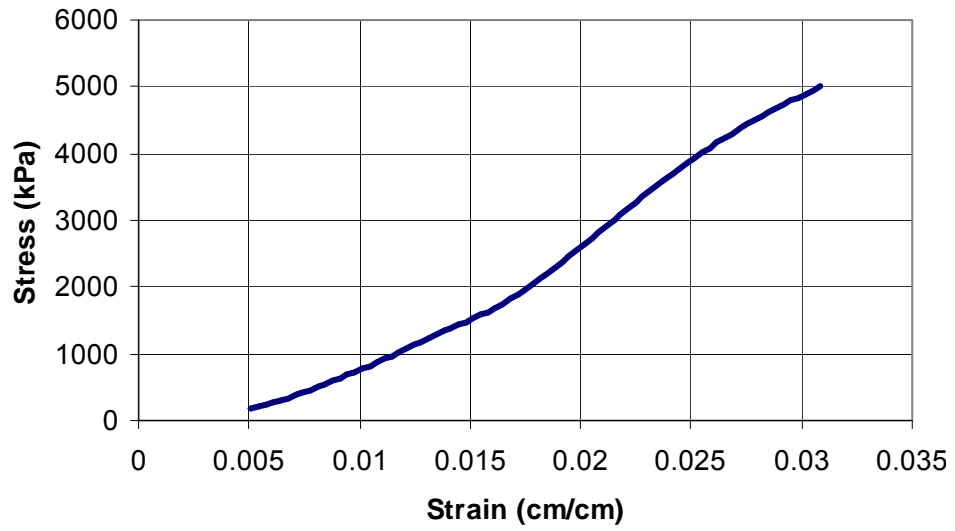


Figure B.19: Stress vs. Strain Plot of Sample MT10 Obtained from Carapace 2

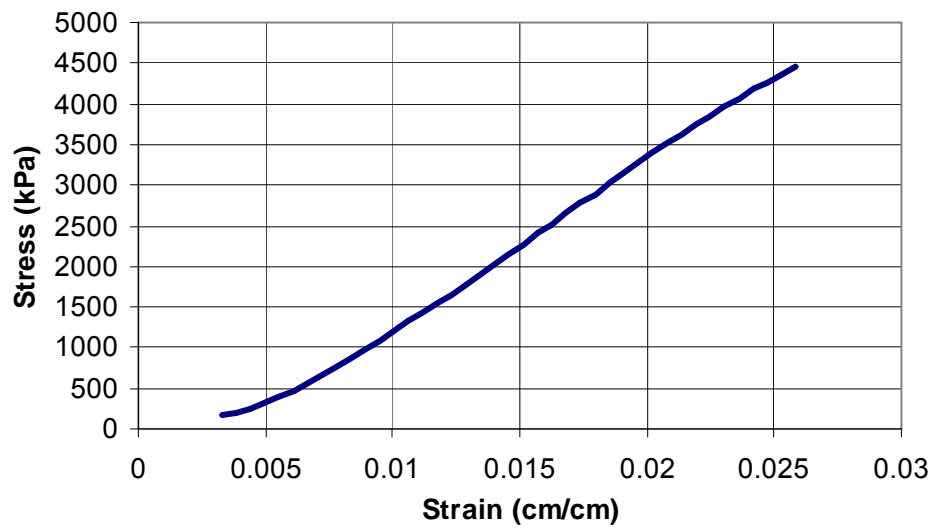


Figure B.20: Stress vs. Strain Plot of Sample RL1 Obtained from Carapace 2

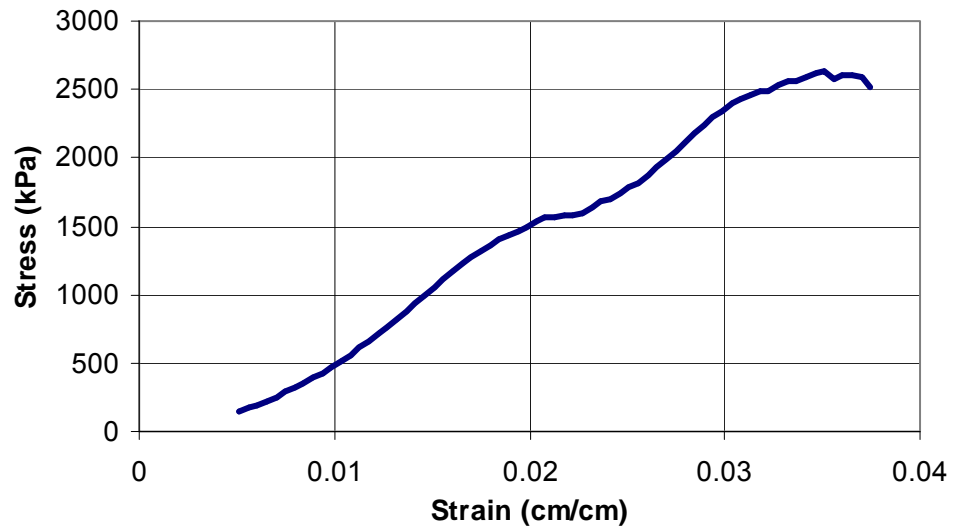


Figure B.21: Stress vs. Strain Plot of Sample RL2 Obtained from Carapace 2

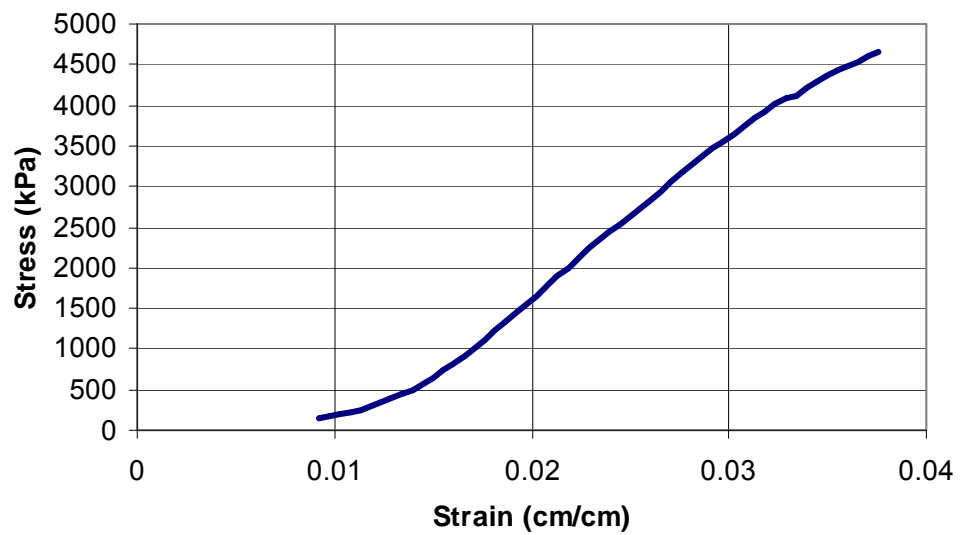


Figure B.22: Stress vs. Strain Plot of Sample RL3 Obtained from Carapace 2

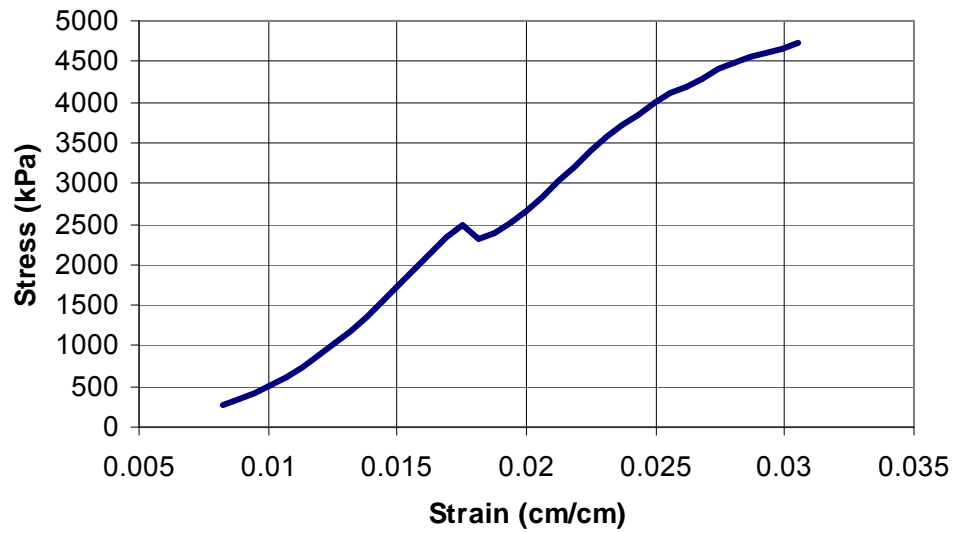


Figure B.23: Stress vs. Strain Plot of Sample RL4 Obtained from Carapace 2

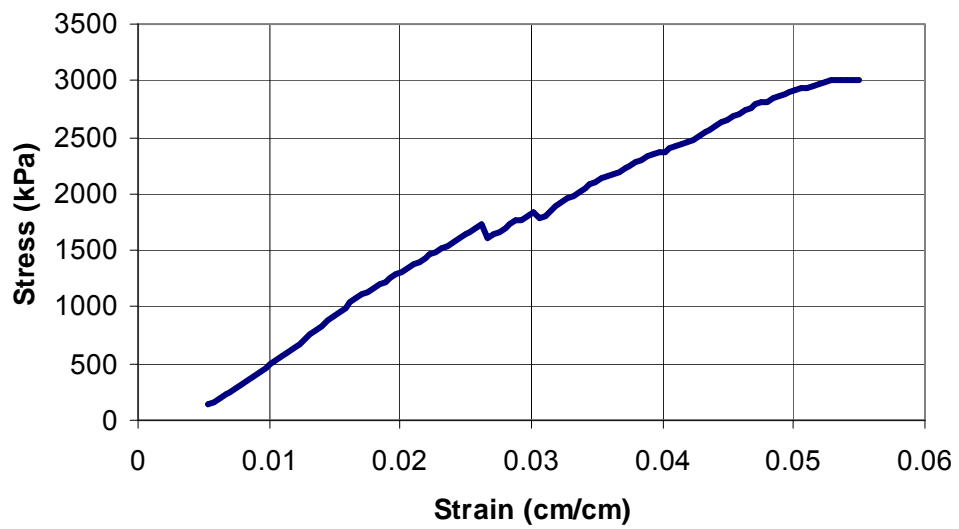


Figure B.24: Stress vs. Strain Plot of Sample RL5 Obtained from Carapace 2

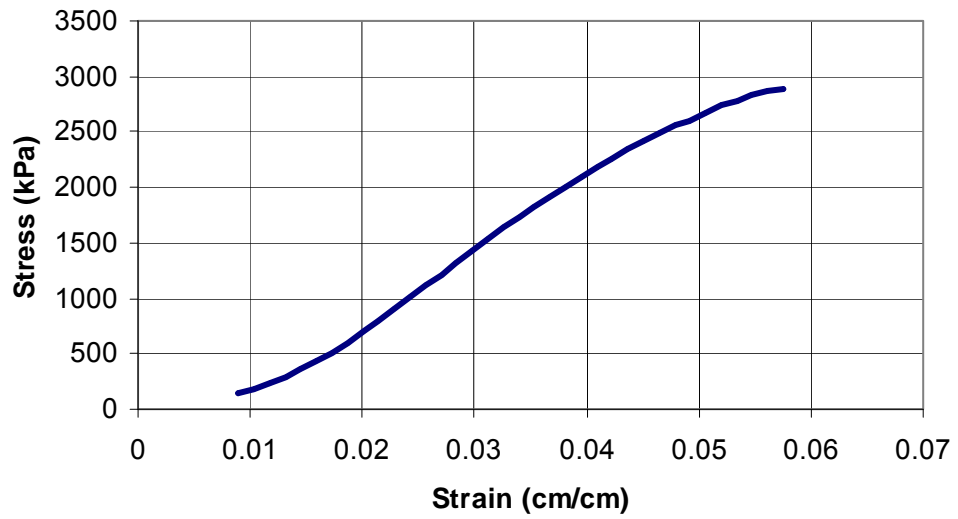


Figure B.25: Stress vs. Strain Plot of Sample RT2 Obtained from Carapace 2

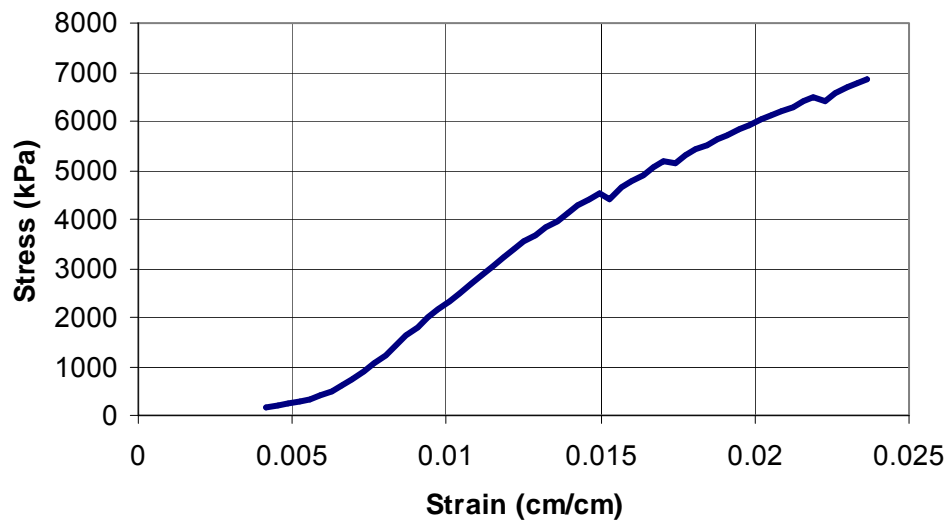


Figure B.26: Stress vs. Strain Plot of Sample RT5 Obtained from Carapace 2

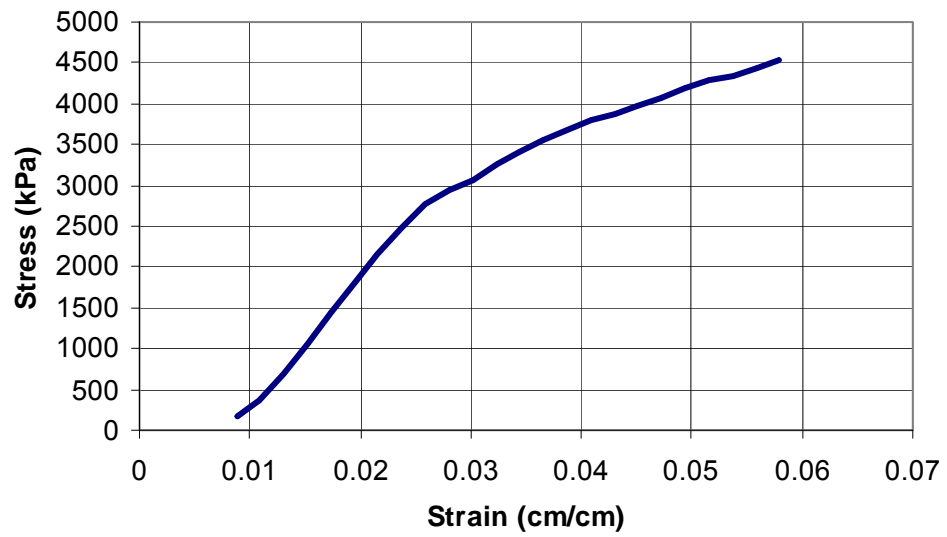


Figure B.27: Stress vs. Strain Plot of Sample RT7 Obtained from Carapace 2

Appendix C

Tensile Stress-Strain Plots – Carapace 3

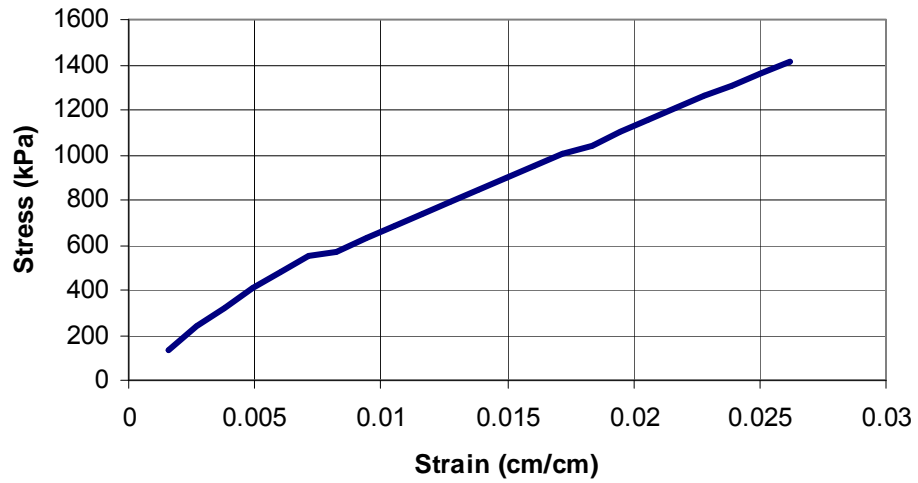


Figure C.1: Stress vs. Strain Plot of Sample FL1 Obtained from Carapace 3

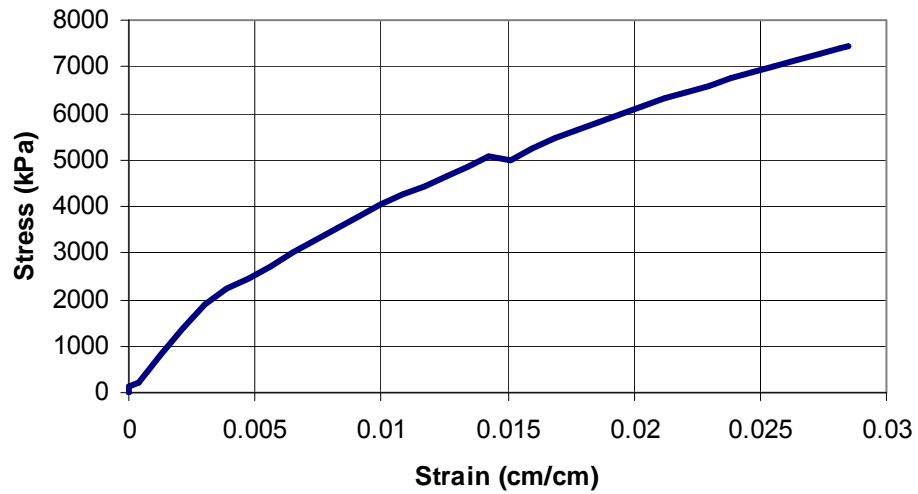


Figure C.2: Stress vs. Strain Plot of Sample FL3 Obtained from Carapace 3

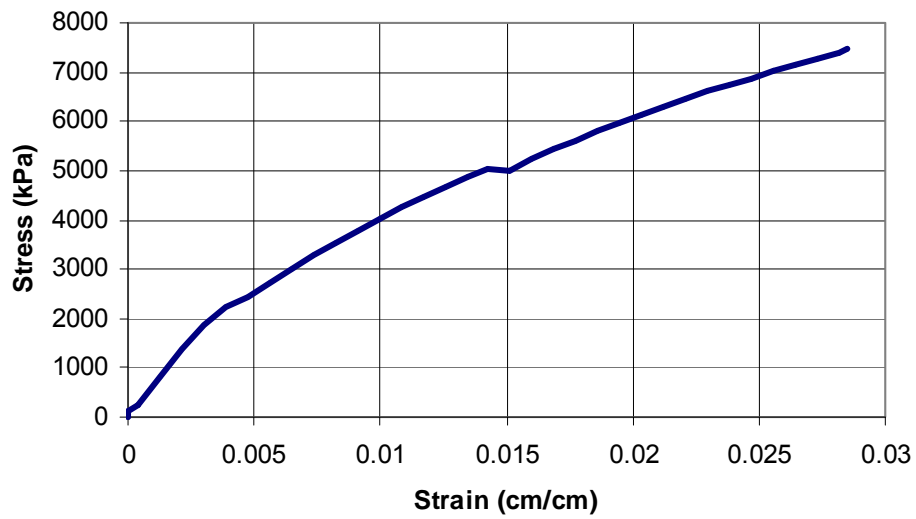


Figure C.3: Stress vs. Strain Plot of Sample ML7 Obtained from Carapace 3

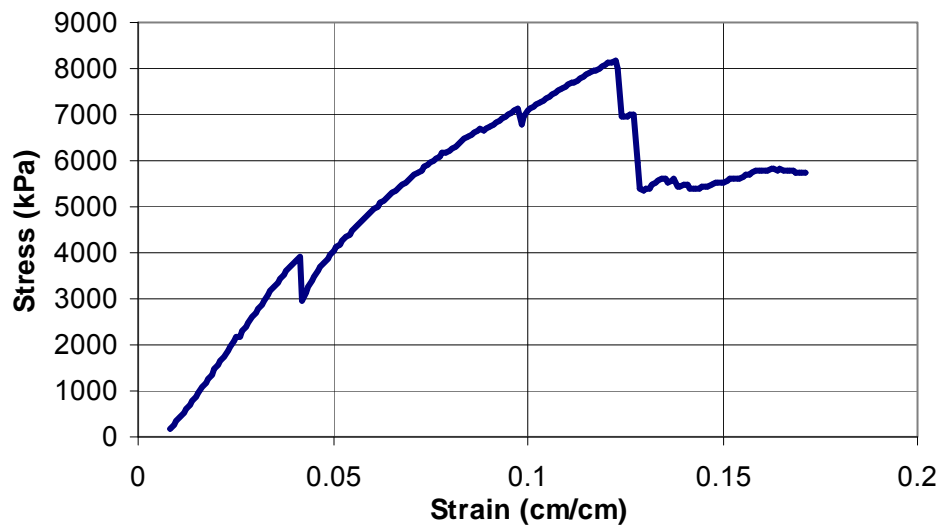


Figure C.4: Stress vs. Strain Plot of Sample ML8 Obtained from Carapace 3

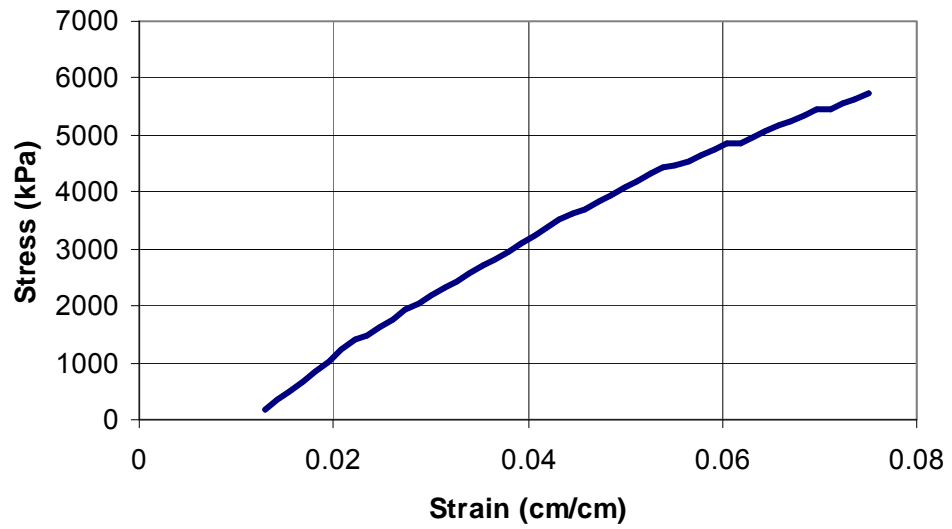


Figure C.5: Stress vs. Strain Plot of Sample ML9 Obtained From Carapace 3

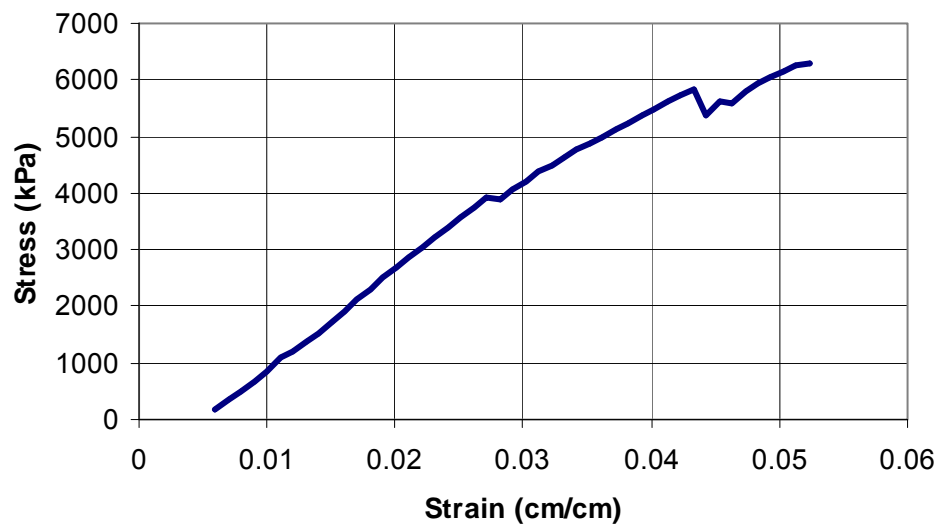


Figure C.6: Stress vs. Strain Plot of Sample MT7 Obtained from Carapace 3

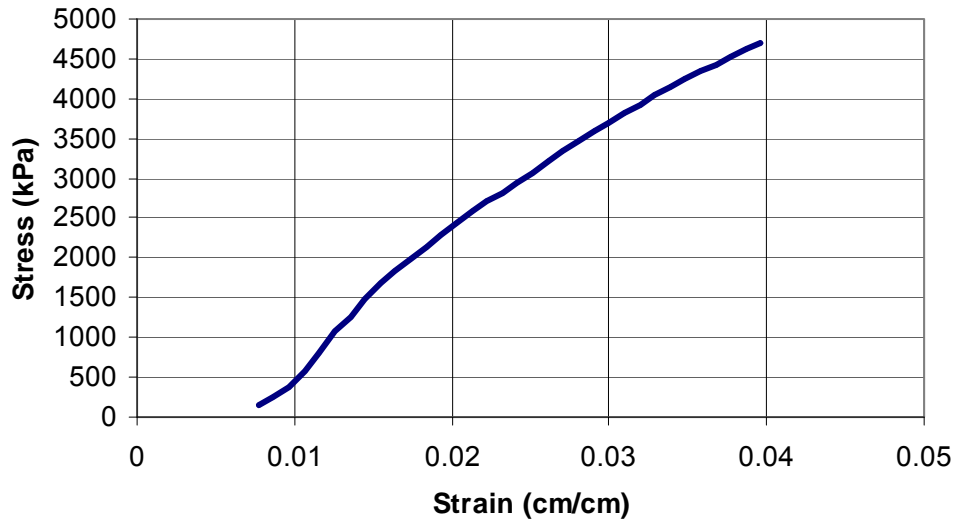


Figure C.7: Stress vs. Strain Plot of Sample MT8 Obtained from Carapace 3

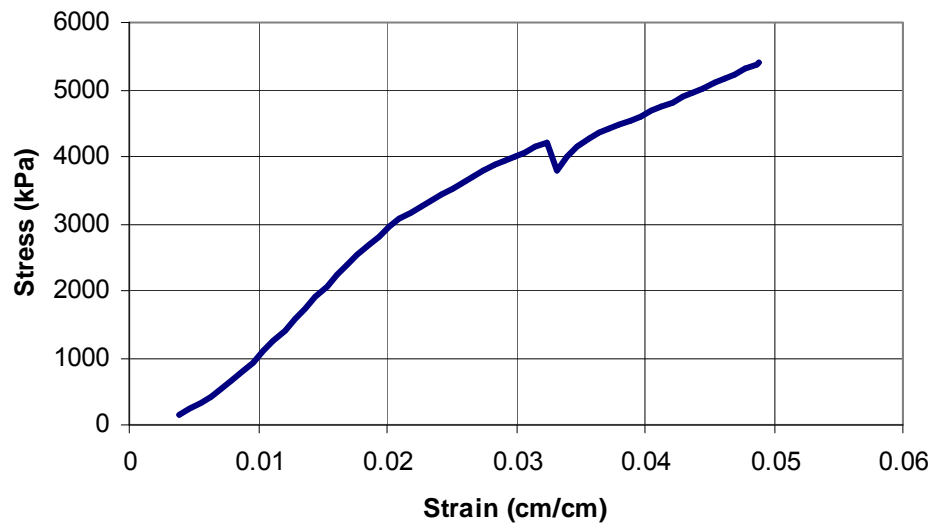


Figure C.8: Stress vs. Strain Plot of Sample MT9 Obtained from Carapace 3

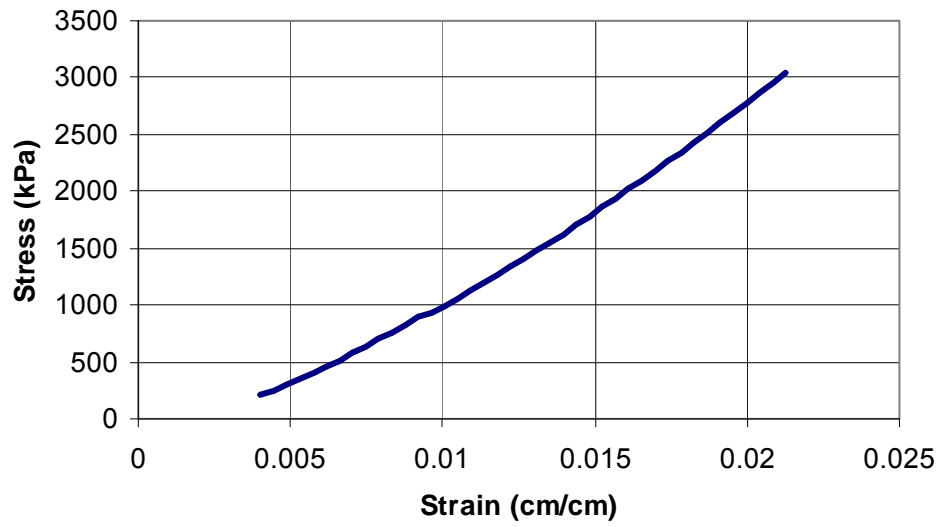


Figure C.9: Stress vs. Strain Plot of Sample MT10 Obtained from Carapace 3

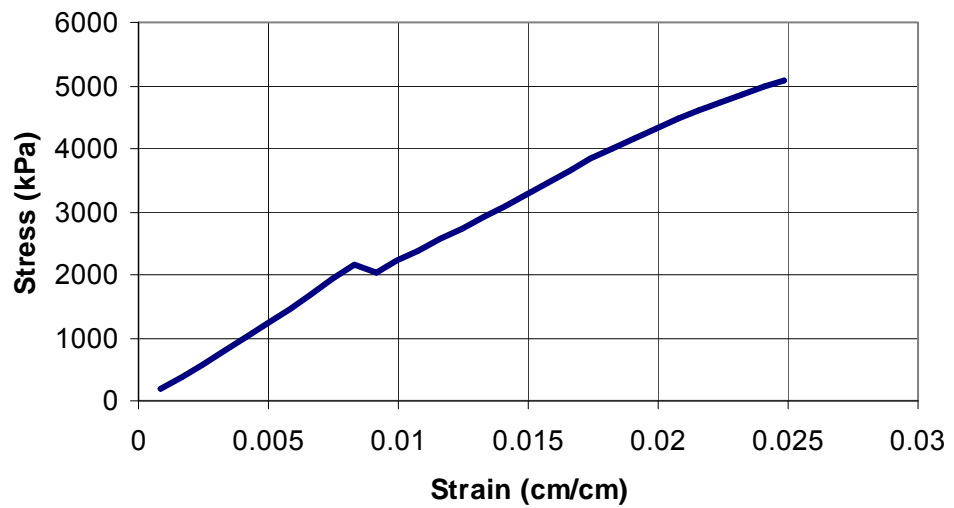


Figure C.10: Stress vs. Strain Plot of Sample RL1 Obtained from Carapace 3

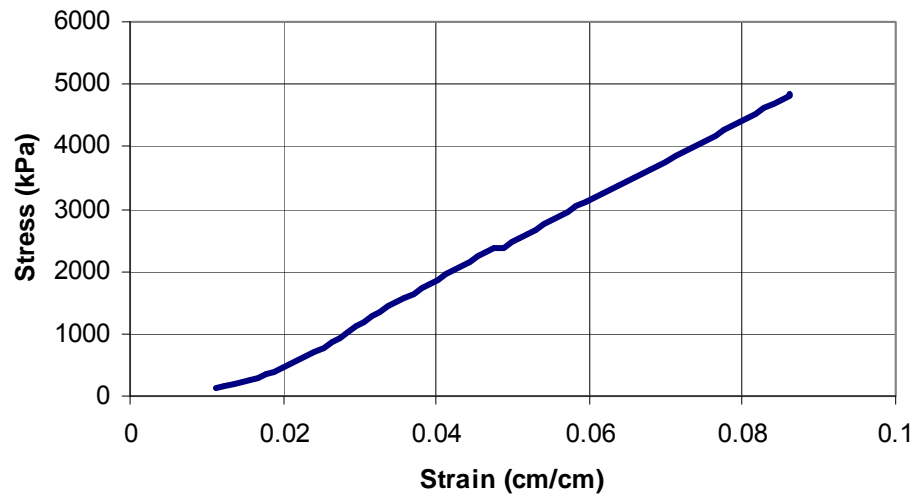


Figure C.11: Stress vs. Strain plot of Sample RT7 Obtained from Carapace 3

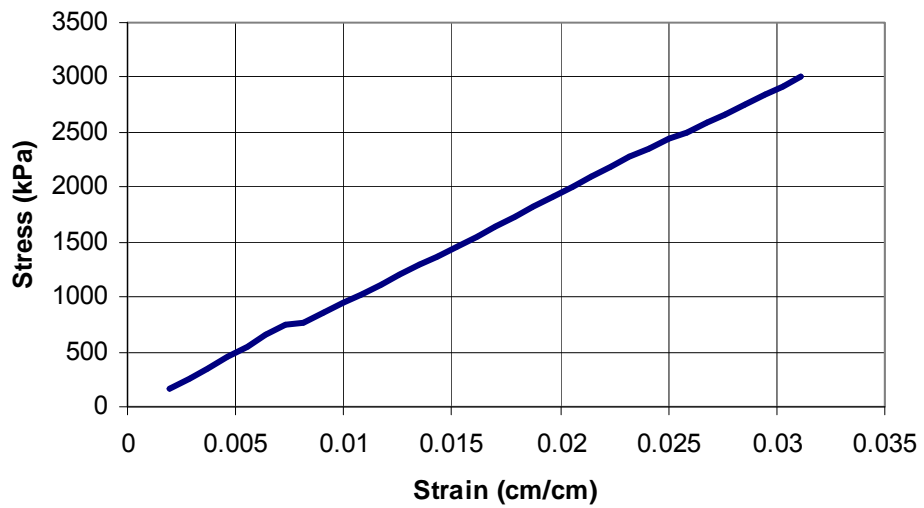


Figure C.12: Stress vs. Strain Plot of Sample RT8 Obtained from Carapace 3

Appendix D

Three-Point Bending Load-Deformation Plots – Carapace 3

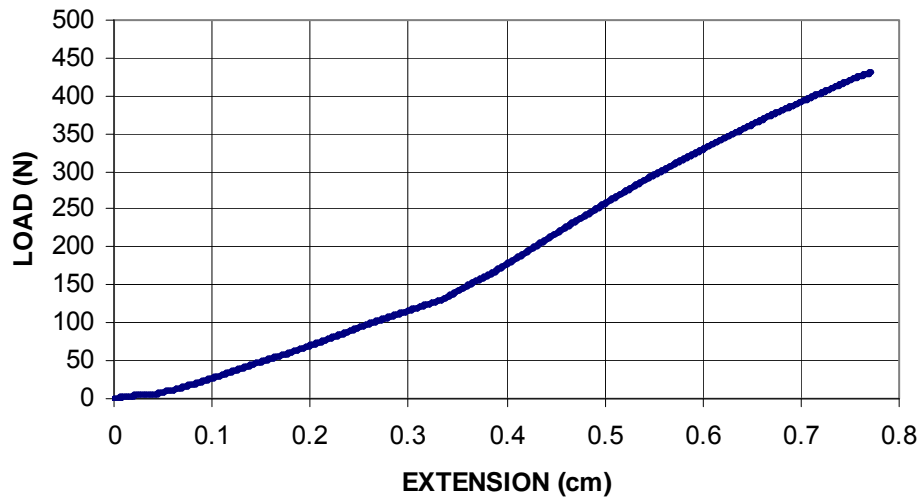


Figure D.1: Load vs. Extension Plot of Sample FT1 Obtained from Carapace 3

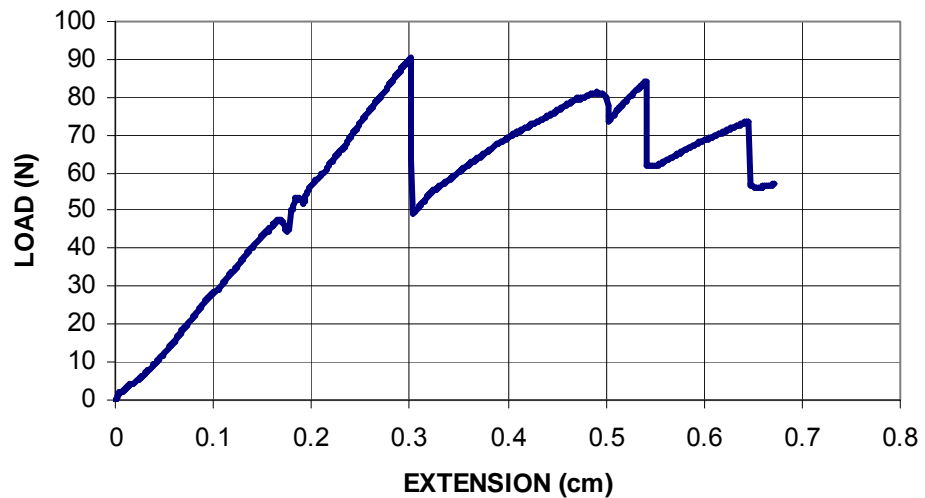


Figure D.2: Load vs. Extension Plot of Sample FT2 Obtained from Carapace 3

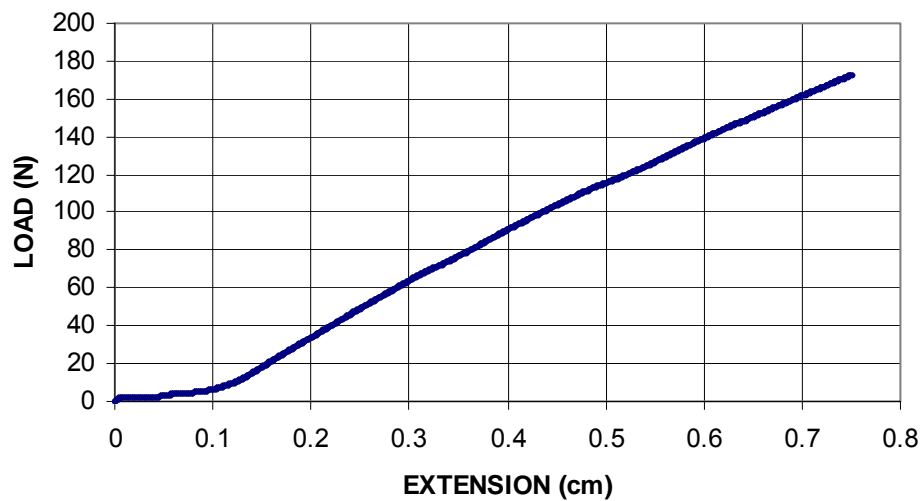


Figure D.3: Load vs. Extension Plot of Sample FT3 Obtained from Carapace 3

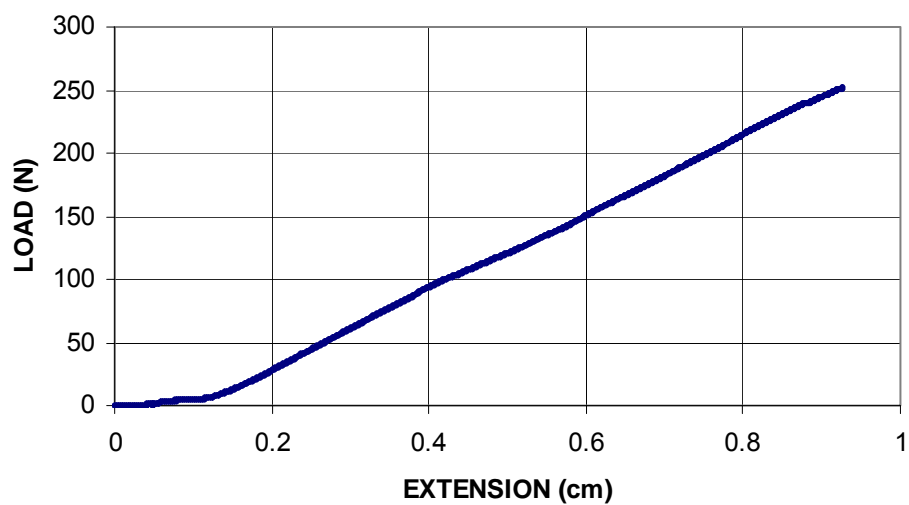


Figure D.4: Load vs. Extension Plot of Sample FT4 Obtained from Carapace 3

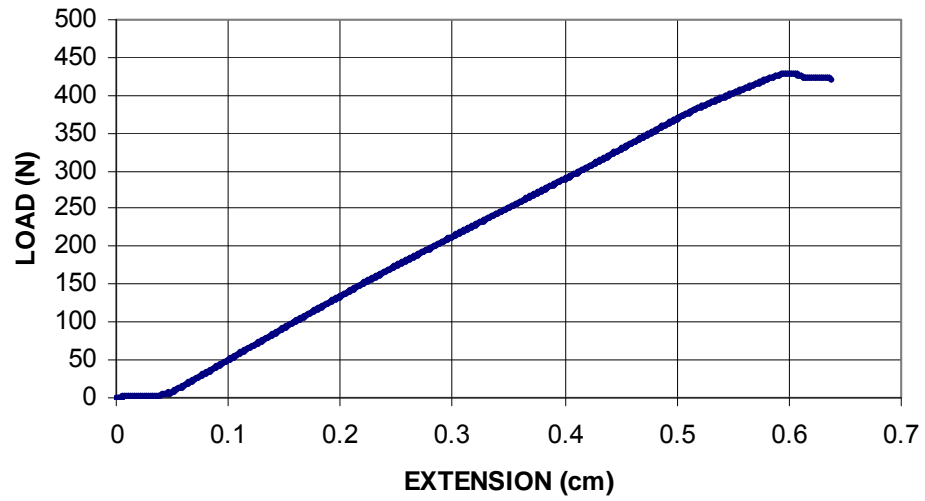


Figure D.5: Load vs. Extension Plot of Sample FT5 Obtained from Carapace 3

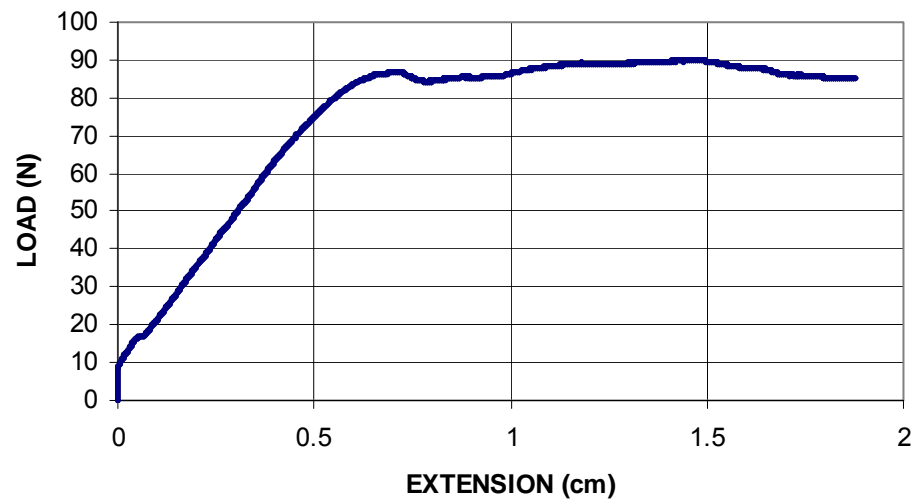


Figure D.6: Load vs. Extension Plot of Sample ML1 Obtained from Carapace 3

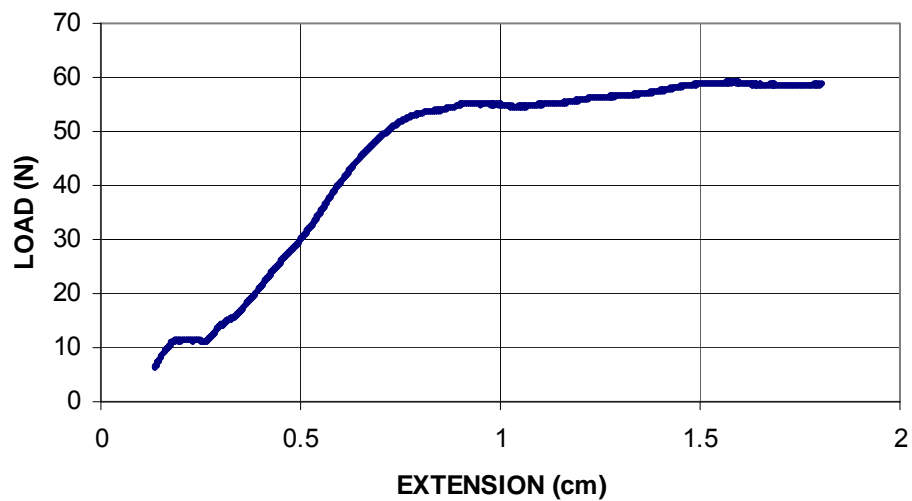


Figure D.7: Load vs. Extension Plot of Sample ML2 Obtained from Carapace 3

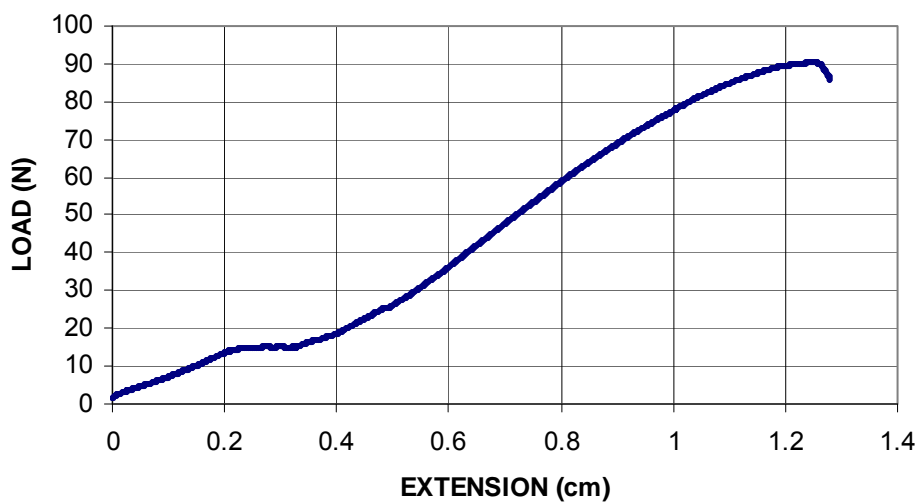


Figure D.8: Load vs. Extension Plot of Sample ML3 Obtained from Carapace 3

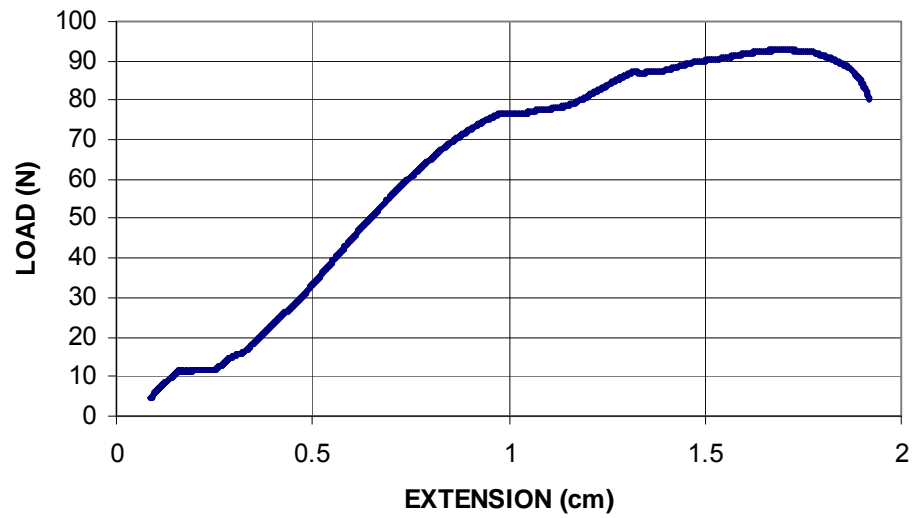


Figure D.9: Load vs. Extension Plot of Sample ML4 Obtained from Carapace 3

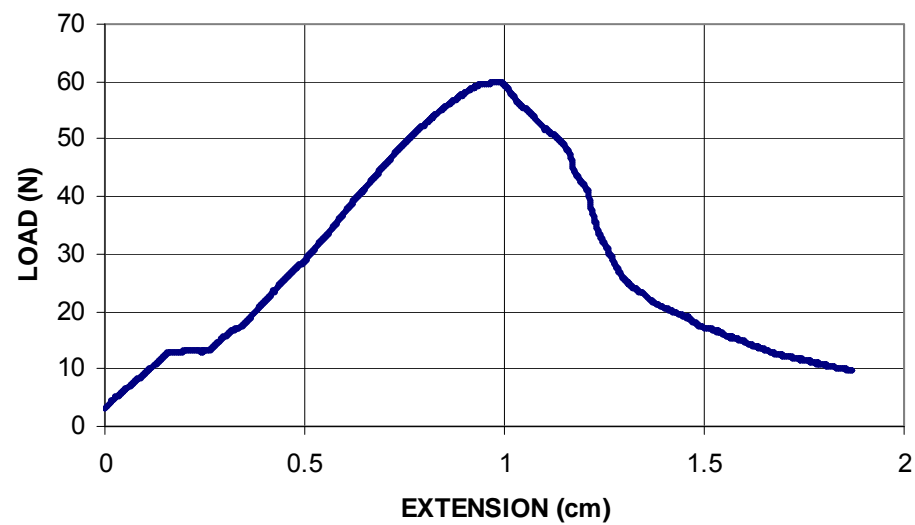


Figure D.10: Load vs. Extension Plot of Sample ML5 Obtained from Carapace 3

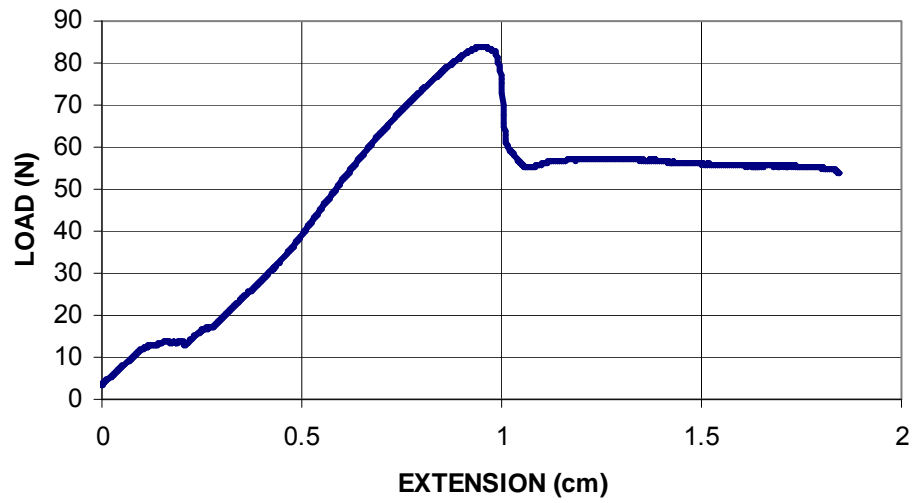


Figure D.11: Load vs. Extension Plot of Sample ML6 Obtained from Carapace 3

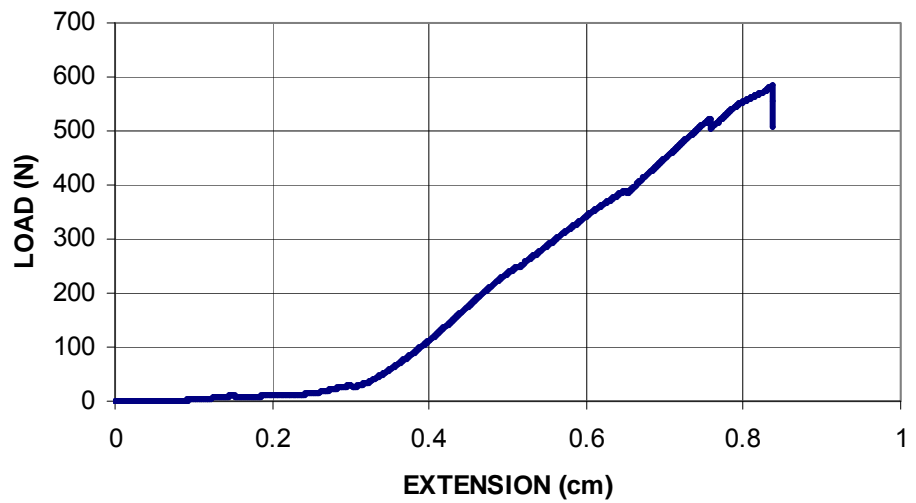


Figure D.12: Load vs. Extension Plot of Sample MT1 Obtained from Carapace 3

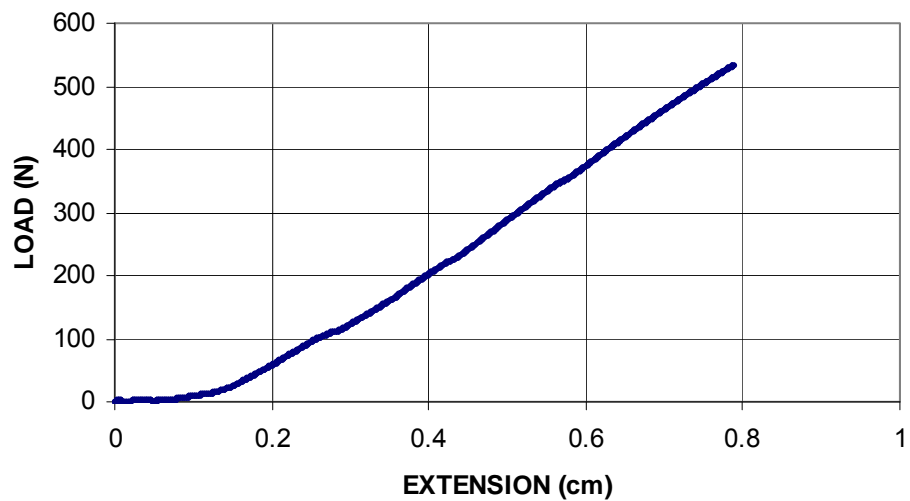


Figure D.13: Load vs. Extension Plot of Sample MT2 Obtained from Carapace 3

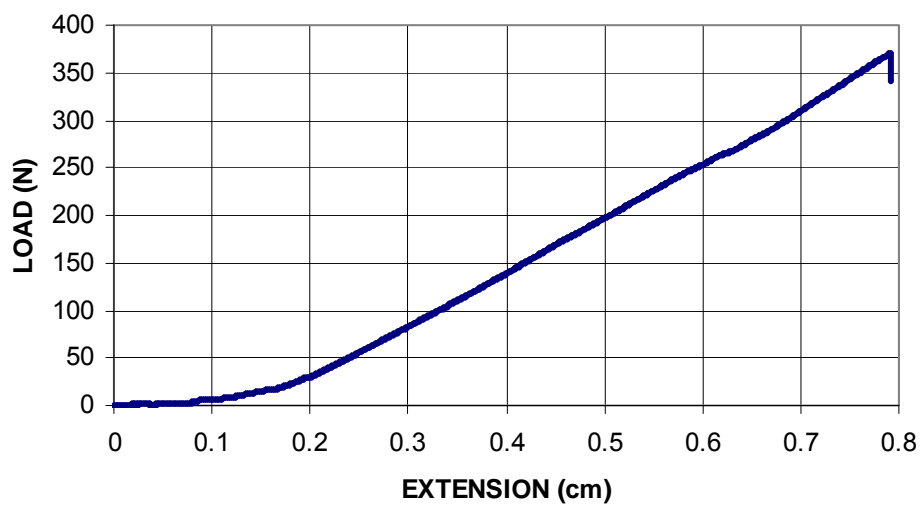


Figure D.14: Load vs. Extension Plot of Sample MT3 Obtained from Carapace 3

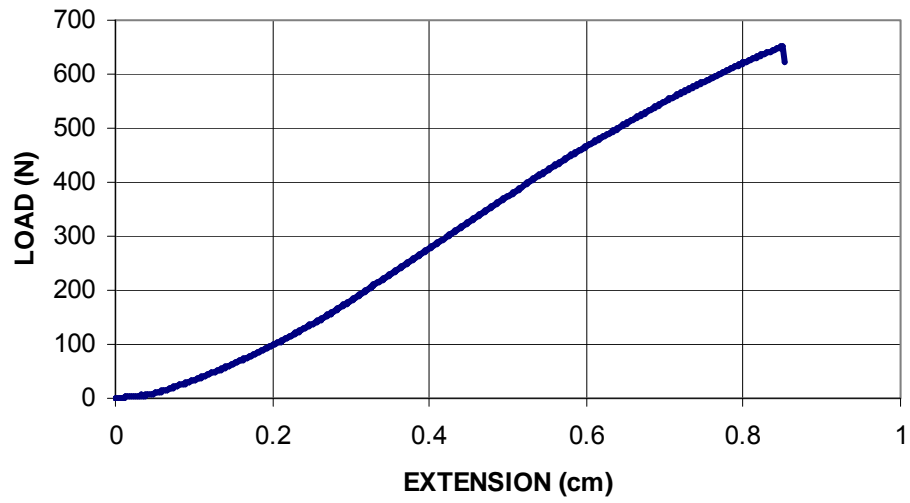


Figure D.15: Load vs. Extension Plot of Sample MT4 Obtained from Carapace 3

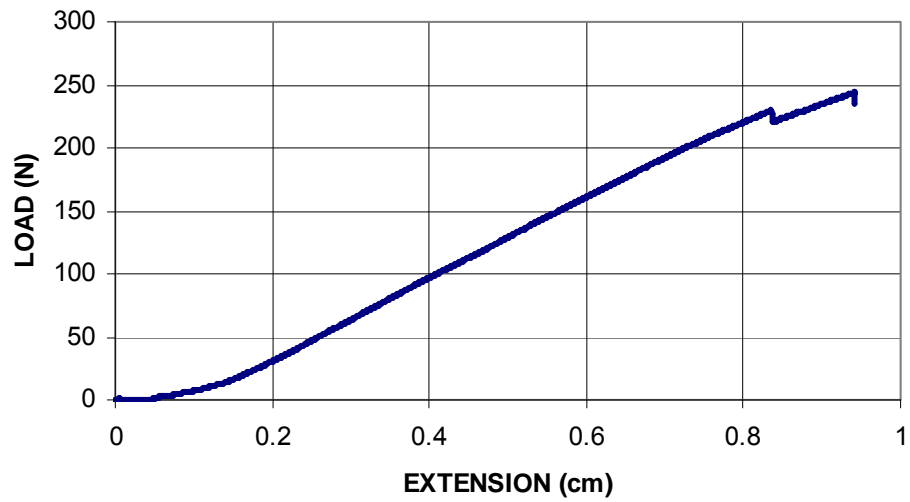


Figure D.16: Load vs. Extension Plot of Sample MT5 Obtained from Carapace 3

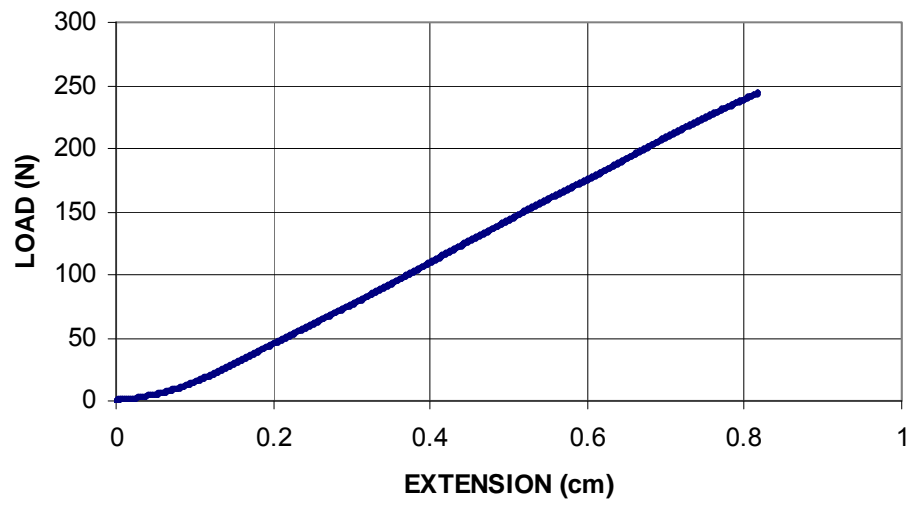


Figure D.17: Load vs. Extension Plot of Sample MT6 Obtained from Carapace 3

Appendix E

Sample Dimensions

Table E.1: Dimensions of Samples Utilized in Carapace 1 Tensile Testing

Sample Designation	Width (cm)	Thickness (cm)	Gage Length (cm)
FT1	2.46	0.99	5.72
FT2	2.54	0.97	6.60
FT3	2.57	1.14	7.11
FT4	2.51	1.12	5.84
ML1	2.49	0.83	6.35
ML2	2.54	0.92	5.72
ML5	2.44	0.99	5.77
ML6	2.62	0.94	4.45
MT1	2.54	1.06	7.37
MT2	2.57	1.02	8.26
MT3	2.49	1.14	7.67
MT6	2.51	0.99	8.89

Table E.2: Dimensions of Samples Utilized in Carapace 2 Tensile Testing

Sample Designation	Width (cm)	Thickness (cm)	Gage Length (cm)
FL1	2.59	0.99	4.78
FL3	2.51	0.74	15.32
FL4	2.54	1.17	10.41
FL6	2.57	1.19	8.26
FL9	2.46	0.86	13.44
FT1	2.49	1.02	12.01
FT3	2.62	0.91	17.15
FT5	2.41	1.02	10.41
FT6	2.69	0.97	14.55
FT8	2.57	1.12	13.56
ML1	2.44	0.84	6.38
ML4	2.54	0.97	12.42
ML5	2.59	0.99	6.68
ML6	2.67	1.02	5.89
ML7	2.49	0.84	11.81
MT1	2.51	0.91	12.24
MT3	2.64	1.02	10.54
MT4	2.51	1.04	7.87
MT5	2.59	0.99	8.89
MT10	2.46	1.07	12.65
RL1	2.62	1.09	7.49
RL4	2.51	0.81	6.83
RL2	2.44	1.14	8.89
RL5	2.39	1.07	9.73
RL3	2.57	1.17	8.05
RT2	2.51	1.17	3.05
RT4	2.49	1.52	6.71
RT5	2.57	1.19	9.40
RT3	2.46	1.07	12.17
RT7	2.57	1.09	1.98

Table E.3: Dimensions of Samples Utilized in Carapace 3 Flexural Testing

Sample Designation	Width (cm)	Depth (cm)	Span Length (cm)
ML1	2.59	0.97	20.3
ML2	2.59	0.99	20.3
ML3	2.51	1.37	20.3
ML4	2.54	0.84	20.3
ML5	2.57	0.84	20.3
ML6	2.62	1.09	20.3
MT1	2.49	1.14	17.8
MT2	2.51	1.14	20.3
MT3	2.59	1.27	20.3
MT4	2.54	1.12	22.9
MT5	2.44	1.07	17.8
MT6	2.57	1.14	17.8
FT1	2.51	1.17	17.8
FT2	2.62	1.14	17.8
FT3	2.57	1.02	17.8
FT4	2.51	1.14	17.8
FT5	2.46	1.42	17.8

Table E.4: Dimensions of Samples Utilized in Carapace 3 Tensile Testing

Sample Designation	Width (cm)	Thickness (cm)	Gage Length (cm)
FL1	2.44	1.35	3.78
FL3	2.44	0.76	4.88
ML7	2.26	0.97	6.05
ML8	2.51	0.99	5.28
ML9	2.34	0.99	3.20
MT7	2.49	1.02	4.19
MT8	2.49	1.27	4.37
MT9	2.79	1.09	5.21
MT10	2.51	0.86	9.80
RL1	2.51	0.99	5.11
RT7	2.57	1.30	3.96
RT8	2.51	1.02	4.78

Appendix F

Calculations for Comparison of Rigid and Specialized Tabs

All dimensions and properties were obtained from the tensile testing of coupon FT3 harvested from Carapace 2. The moments and axial loads were determined by the SAP2000 nonlinear frame analysis.

Sectional Properties

$$t = 2.62 \text{ cm} \quad h = 0.91 \text{ cm} \quad c = h / 2 = 0.46 \text{ cm}$$

$$I = \frac{t \cdot h^3}{12} = 0.16 \text{ cm}^4 \quad A = t \cdot h = 2.38 \text{ cm}^2$$

Fixed-Fixed Case

$$M_{ult} = 234.26 \text{ N} \cdot \text{cm} \quad P_{ult} = 758.55 \text{ N}$$

Stress due to Axial Force

Stress due to Bending Moment

$$\sigma_p = \frac{P_{ult}}{A}$$

$$\sigma_M = \frac{M_{ult} \cdot c}{I}$$

$$\sigma_{ult} = \sigma_p + \sigma_M = 9659.93 \text{ kPa}$$

Percent Stress due to Bending

$$PSB = \frac{\sigma_M}{\sigma_{ult}} = 67.06 \%$$

Pinned-Pinned Case

$$M_{ult} = 99.89 \text{ N} \cdot \text{cm} \quad P_{ult} = 768.00 \text{ N}$$

Stress due to Axial Force

$$\sigma_p = \frac{P_{ult}}{A}$$

Stress due to Bending Moment

$$\sigma_M = \frac{M_{ult} \cdot c}{I}$$

$$\sigma_{ult} = \sigma_p + \sigma_M = 5983.62 \text{ kPa}$$

Percent Stress due to Bending

$$PSB = \frac{\sigma_M}{\sigma_{ult}} = 46.17 \%$$

Appendix G

Proposed Test Method for Tensile Properties of Sea Turtle Carapace

This proposed test method is primarily designed to obtain properties that will aid in the development of a biomimetic sea turtle carapace comprised of synthetic materials. The procedure may be employed to estimate the ultimate tensile stress, tensile modulus, and strain at failure of the shell. The stresses due to curvature are minimized by the implementation of specialized tabs, but neglected in the computations. Consequently, the properties will not be exact and the synthetic materials selected for mimicry must be verified under identical test conditions. However, a procedure for determining the ultimate normal stress has been included that accounts for the curvature-induced bending. The following procedure assumes that the carapace has been previously cleaned and is free of all connective tissue.

G.1 Summary of Method

A coupon having constant width is mounted in the grips of a mechanical testing device. The crosshead of the device is set to automatically displace at a constant rate while the axial force and elongation are recorded at regular intervals. The properties of ultimate strength, modulus, and strain at failure may be determined from the load-deformation data. In addition, the force per unit width at failure may be computed with no additional apparatus. However, the transverse displacement must be measured at the time the maximum load is attained in order to compute the ultimate normal stress.

G.2 Essential Apparatus and Materials

The following equipment and materials will be required for the successful completion of this test procedure. The quantity of the materials is dependent upon the size of the carapace and the number of samples harvested.

Apparatus:

1. Universal testing machine with grips (Accuracy ± 1.00 lb)
2. Digital caliper (Accuracy ± 0.0127 mm)
3. Linear variable differential transformer (LVDT)*
4. Masonry saw with water-cooled blade

*Only required if the transverse displacement is to be recorded.

Materials:

1. Intact and cleaned sea turtle carapace
2. Gauze and solution of 50% saline solution and 50% alcohol
3. 3.18 cm diameter PVC pipes and caps
4. Commercially available two-part epoxy
5. 2.20 cm x 10.0 cm x 0.100 cm steel plate
6. Commercially available plumbers putty

G.3 Coupon Harvesting and Preservation

Coupon harvesting and cutting must be conducted under constant irrigation in order to avoid burning, which may greatly alter the measured material properties. Water-

cooled masonry saws are ideal for this application. In order to determine any variation in tensile properties associated with sample location, the carapace should be divided into six regions. This may be accomplished by bisecting the shell along the spine and then sectioning the two halves into segments of equal length measured along the length of the carapace. A minimum of six samples should be harvested from each region with equivalent quantities parallel and transverse to the spine. The six regions are shown in Figure G.1 with the harvested coupons and their orientations depicted as white rectangular spaces. It should be noted that coupons should not be harvested from regions displaying signs of damage as the measured material properties may be affected.

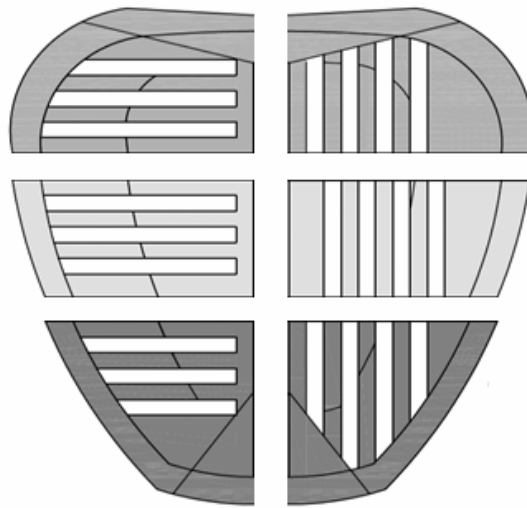


Figure G.1: Carapace Harvesting Regions and Coupon Orientations

The samples should be formed to a constant width of 2.54 cm where possible. The thickness of the material must not be altered as any composite behavior associated with the cross-section may be distorted. Similarly, the gage length of the sample will be influenced by the geometry of the carapace. However, care should be taken to prevent

the presence of rib, spine, and connective tissue in the samples as inconsistent results may be observed.

For preservation, coupons should be wrapped in gauze and stored in a solution of 50% saline solution and 50% alcohol. For periods less than three months, the samples may be stored at room temperature (20-25 °C). However, long-term preservation requires the coupons to be stored at temperatures below freezing (0 °C).

G.4 Fabrication of Bonded Tabs

Specialized tabs are required to mitigate curvature induced fixed-end moments and prevent damage from clamping force at the grips. The tabs will be constructed of a 3.18 cm diameter PVC pipe and cap, commercially available two-part epoxy, and a 2.20 cm x 10 cm x 0.1 cm steel plate. Plumbers putty will also be required to stabilize the epoxy prior to curing. The stages for the fabrication of one tab are as follows:

1. A 2.5 cm opening must be cut in the top center of the PVC cap. This may be accomplished using a thin grinding wheel or circular saw.
2. Bend the steel tab to form a J-hook at one end. The steel should be thin enough to allow for this to be accomplished manually or with a pair of pliers. Next, insert the tab through the void cut in the PVC cap so that the J-hook is on the inside (Figure G.2).
3. Apply the commercially available plumber's putty to the outside of the cap ensuring that no fluid may flow through the void space.
4. Cut a segment of the PVC pipe to a length of approximately 6.35 cm. Insert the segment of pipe into the cap and place the object into a 3.81 cm to 3.81 cm rubber

pipe coupler. This should be done in a manner that allows for the PVC pipe to contain the epoxy. The coupler is only used to support the tab while the epoxy is curing.

5. Combine the constituents of the two part epoxy and mix as specified. Then, fill the PVC pipe with epoxy until it is full.
6. Place one end of the thoroughly dried coupon into the PVC pipe permitting a minimum of 2.50 cm of the sample to be submerged in the epoxy. The coupon must be balanced in place. This may be accomplished using small clamps as shown in Figure 4.3.
7. Allow the epoxy to cure as specified by the manufacturer. Once the epoxy has fully hardened, repeat this process for the alternate end of the coupon.

A schematic showing the cross-section of the completed tab is given in Figure G.2

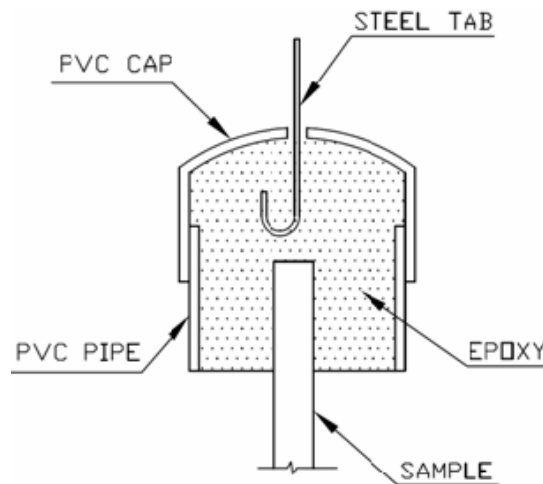


Figure G.2: Cross-Section of Completed Bonded Tab

G.5 Tensile Test Procedure

The minimum width (b), minimum depth (d), and initial gage length (L_o) of the sample should be measured and recorded using a digital caliper prior to testing. The gage length shall be determined by the length of exposed bone between the two bonded tabs. In order to ensure that the full stress-strain response of the sample is captured, the displacement rate of the cross-heads should be set to a maximum of 2.54 mm/min. The test specimen may then be loaded into the grips of the mechanical testing device with the clamping force applied to the steel plate protruding from the PVC cap. A minimum of 6.40 mm of the steel plate should remain exposed between the PVC cap and the grips. Once the load and cross-head extension measurement devices are balanced the test may be initiated. Load and crosshead extension values should be automatically recorded at one second intervals until a successful failure of the sample occurs. Successful failure is defined as tensile rupture perpendicular to the direction of loading that occurs along the gage length of the sample with no slipping detected at the bone-epoxy interface. If the ultimate normal stress is to be determined, the transverse displacement at the location of maximum initial eccentricity must also be measured during testing. This may be accomplished through the use of a linear variable differential transformer (LVDT) or equivalent displacement measuring device.

G.6 Determination of Tensile Properties

The ultimate tensile stress will be determined using Equation (G.1). In addition, the tensile stress for each data point must be computed. This will be accomplished through Equation (G.2).

$$F_{ult}^p = \frac{P_{\max}}{b \cdot d} \quad (G.1)$$

$$\sigma_i = \frac{P_i}{b \cdot d} \quad (G.2)$$

Where

F_{ult}^p = ultimate tensile strength (MPa)

σ_i = tensile stress at *ith* data point (MPa)

P_{\max} = maximum tensile load (N)

P_i = load at *ith* data point (N)

b = width of cross - section (mm)

d = minimum thickness of cross - section (mm)

The engineering strain at failure and the engineering strain for each data point will be determined using equations (G.3) and (G.4) respectively.

$$\varepsilon_f^p = \frac{\delta_f}{L_o} \quad (G.3)$$

$$\varepsilon_i = \frac{\delta_i}{L_o} \quad (G.4)$$

Where

ε_f^p = strain at failure (mm/mm)

ε_i = strain at the *ith* data point (mm/mm)

δ_f = crosshead extension at failure (mm)

δ_i = crosshead extension at the *ith* data point (mm)

L_o = initial gage length of the sample (mm)

The tensile modulus of elasticity may now be determined by plotting the stress versus the strain data points (σ_i vs. ϵ_i). The modulus will be computed as the slope of the initial linear portion of the stress-strain curve as shown in Equation (G.5). The data points employed for this calculation must be contained within the initial linear region of the stress-strain curve.

$$E^p = \left(\frac{\sigma_{i+n} - \sigma_i}{\epsilon_{i+n} - \epsilon_i} \right)_{Lin} \quad (G.5)$$

Where

E^p = tensile modulus of elasticity (MPa)

σ_{i+n} = tensile stress at the i th plus n data point (MPa)

ϵ_{i+n} = tensile strain at the i th plus n data point (mm/mm)

For many applications the ultimate force per unit width of the sample may be useful. This value is determined by multiplying the ultimate tensile strength by the thickness of the sample as shown in Equation (G.6).

$$FUW = F_{ult}^p \cdot d \quad (G.6)$$

Where

FUW = ultimate force per unit width (N/mm)

If the transverse displacement of the coupon was recorded, the ultimate normal stress may be determined by Equation (G.7). This computation accounts for the second order effects induced by sample elongation and the resulting reduction in curvature.

$$\sigma_{ult}^N = \frac{P_{max}}{b \cdot d} \left(1 + \frac{6 \cdot (e - \Delta_t)}{d} \right) \quad (10.7)$$

Where

σ_{ult}^N = ultimate normal stress (Mpa)

e = initial maximum eccentricity of tensile loading (mm)

Δ_t = transverse displacement at time of maximum loading (mm)

The following schematic (Figure G.3) illustrates the manner at which the initial eccentricity and transverse displacement shall be measured.

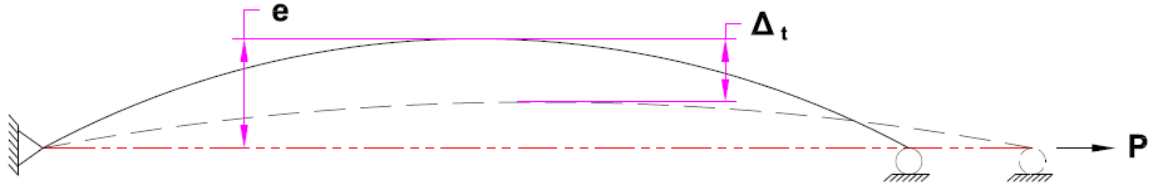


Figure G.3: Initial Eccentricity and Transverse Displacement

G.7 Report

The report should include the following items:

1. The names of the test operators and the dates on which the testing was conducted.
2. All apparatus and the associated precision.
3. Where applicable, the age of the loggerhead, time since death, and period and type of preservation should be noted.

4. Any variations in the test method, equipment malfunctions, or anomalies must be reported in detail.
5. The individual values for ultimate strength, strain at failure, and tensile modulus. Each must be presented in a manner that allows for identification of the coupon location and orientation.
6. The stress-strain curve generated for each sample.
7. If determined, the ultimate normal strength and ultimate load per unit width for each coupon tested.
8. The average, standard deviation, and coefficient of variation for each property determined for the six alternate combinations of region and orientation.
9. The collective average, standard deviation, and coefficient of variation for each property independent of sample location or orientation.
10. Any trends observed in the results should be identified and explicated in detail.

Appendix H

Tensile Load-Extension Plots – Synthetic Carapace 1

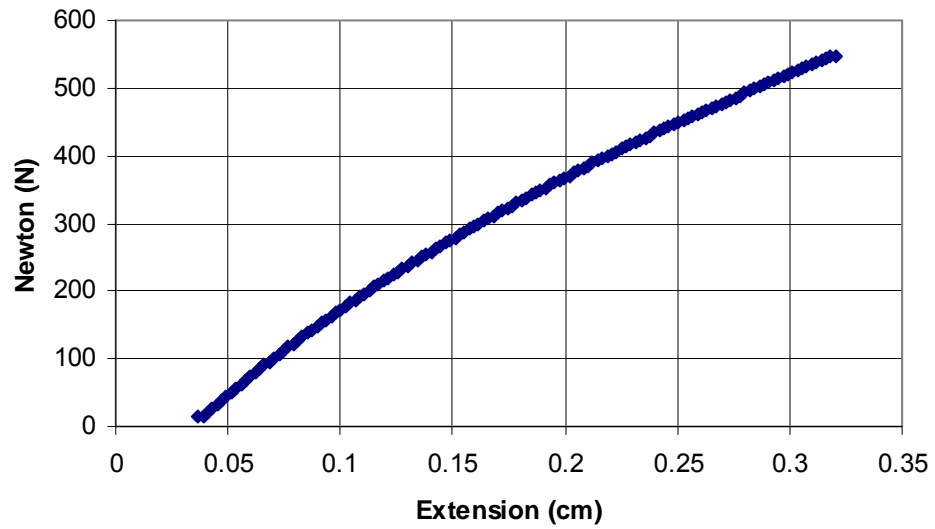


Figure H.1: Load-Extension Curve for Sample 1, Synthetic Carapace 1

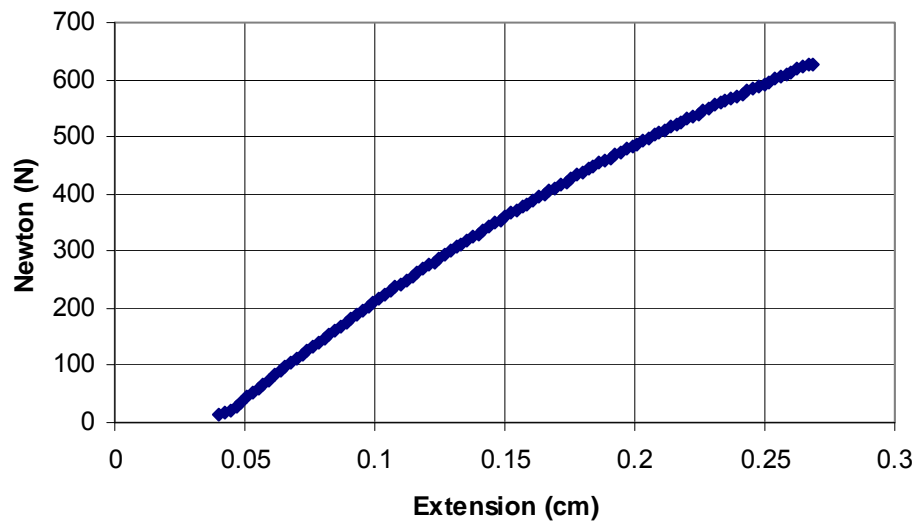


Figure H.2: Load-Extension Curve for Sample 2, Synthetic Carapace 1

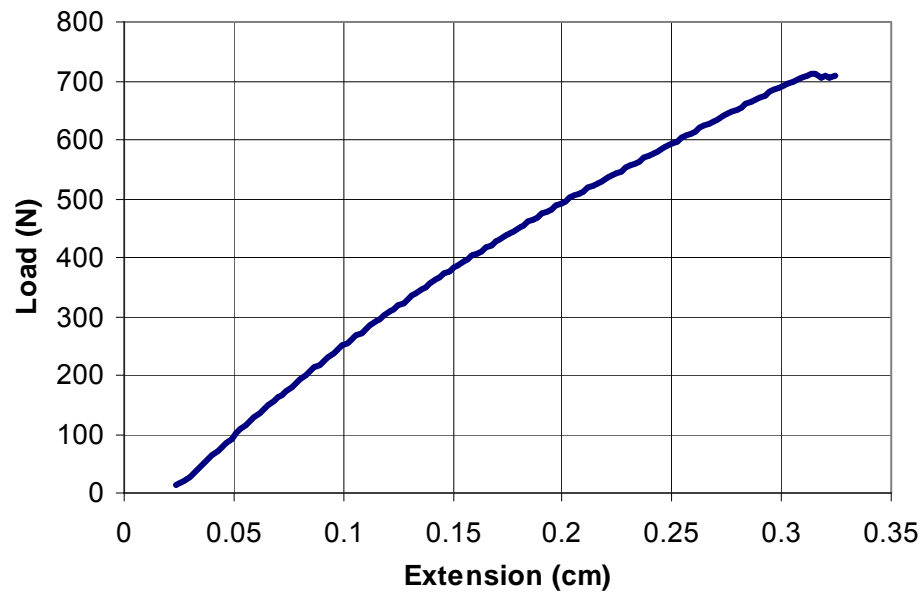


Figure H.3: Load-Extension Curve for Sample 3, Synthetic Carapace 1

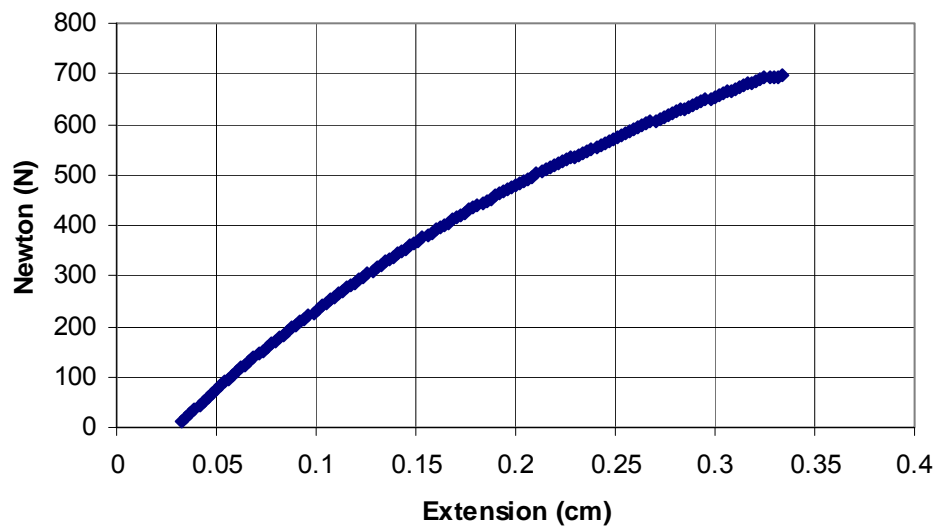


Figure H.4: Load-Extension Curve for Sample 4, Synthetic Carapace 1

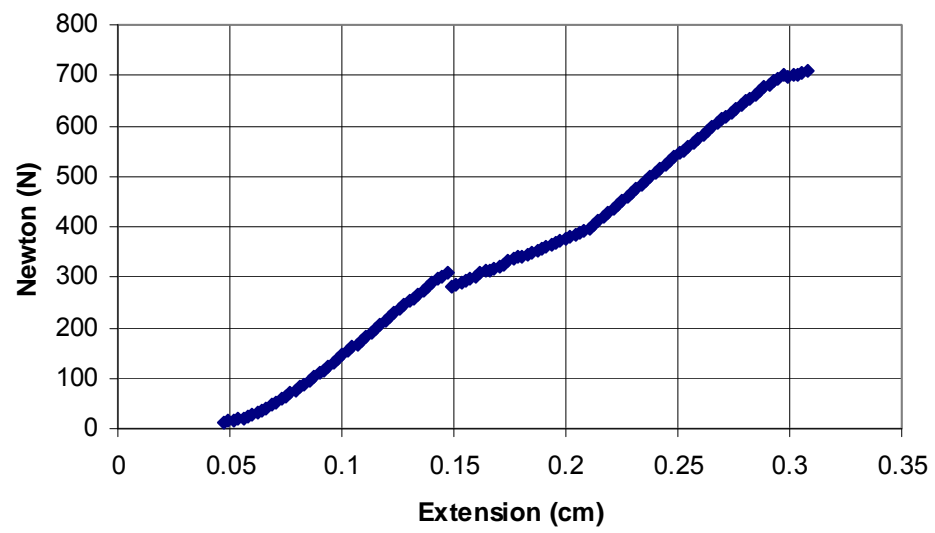


Figure H.5: Load-Extension Curve for Sample 5, Synthetic Carapace 1

Appendix I

Tensile Load-Extension Plots – Synthetic Carapace 2

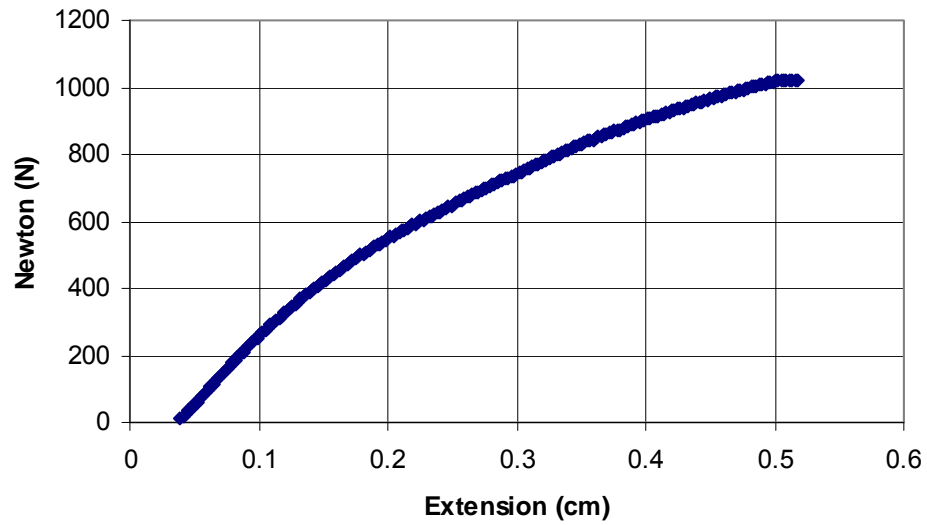


Figure I.1: Load-Extension Curve for Longitudinal Sample 1, Synthetic Carapace 2

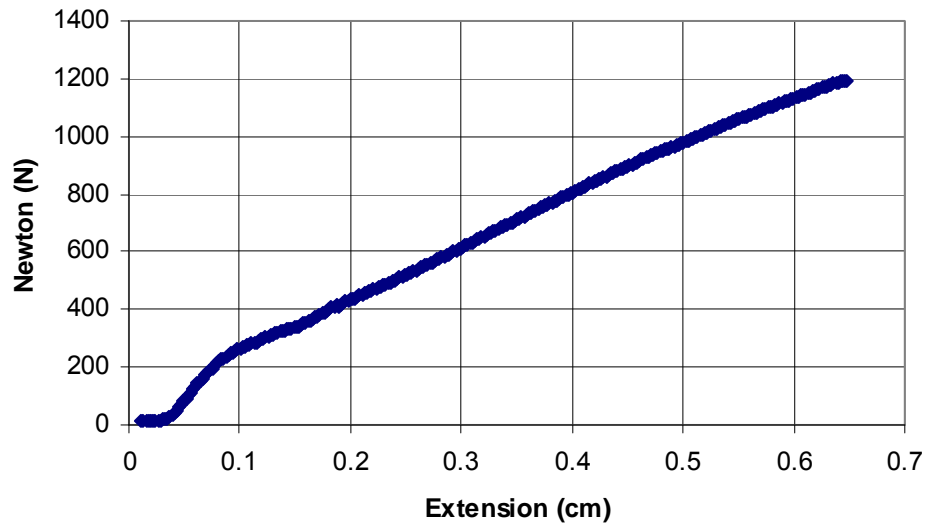


Figure I.2: Load-Extension Curve for Longitudinal Sample 1, Synthetic Carapace 2

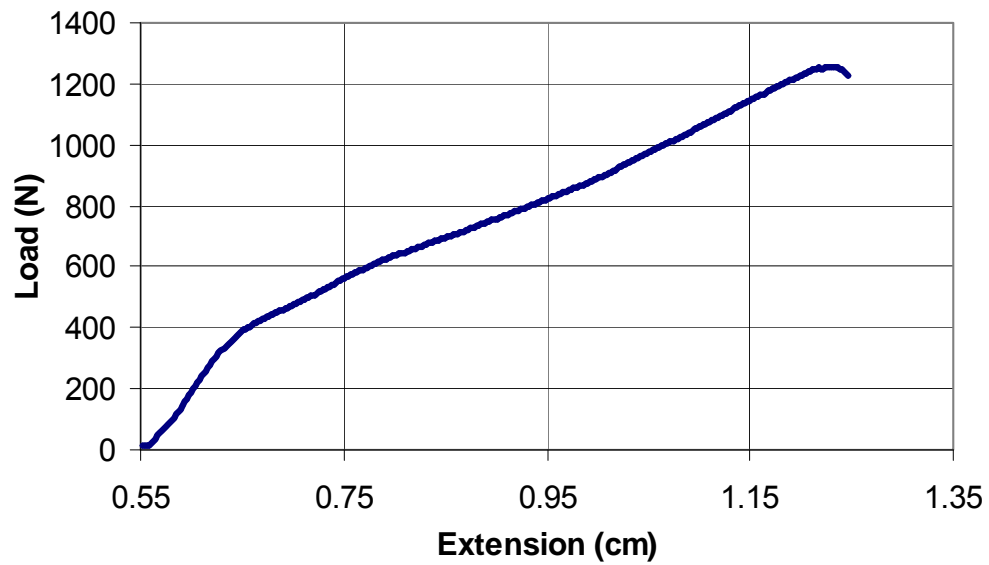


Figure I.4: Load-Extension Curve for Longitudinal Sample 4, Synthetic Carapace 2

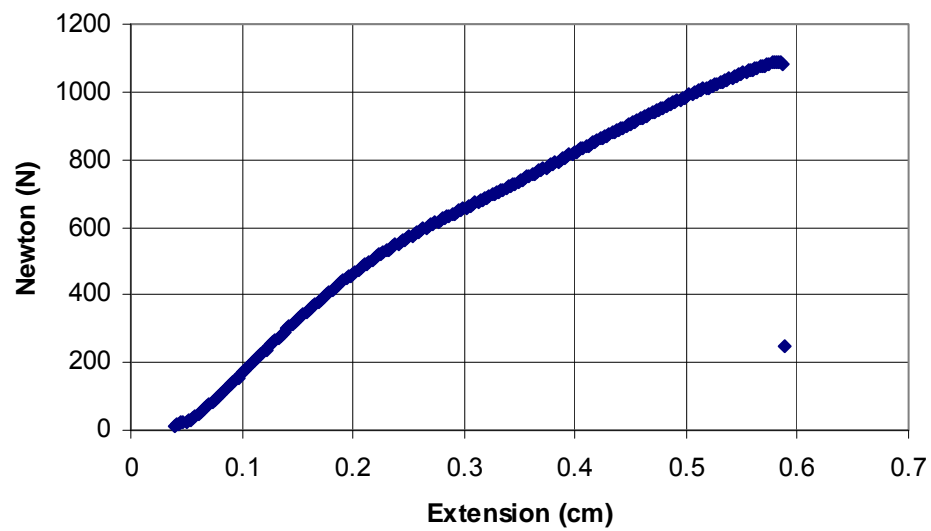


Figure I.5: Load-Extension Curve for Longitudinal Sample 5, Synthetic Carapace 2

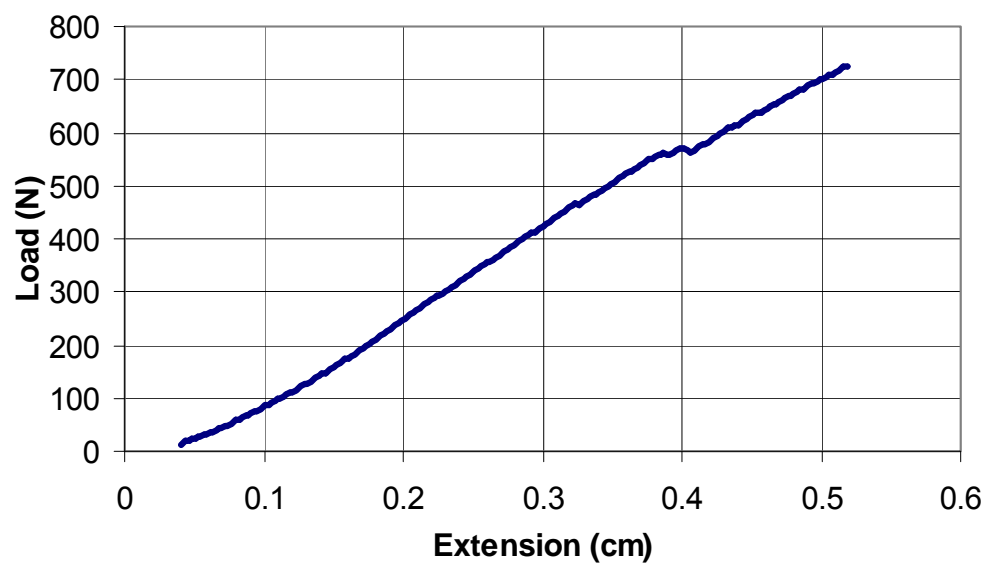


Figure I.6: Load-Extension Curve for Transverse Sample 1, Synthetic Carapace 2

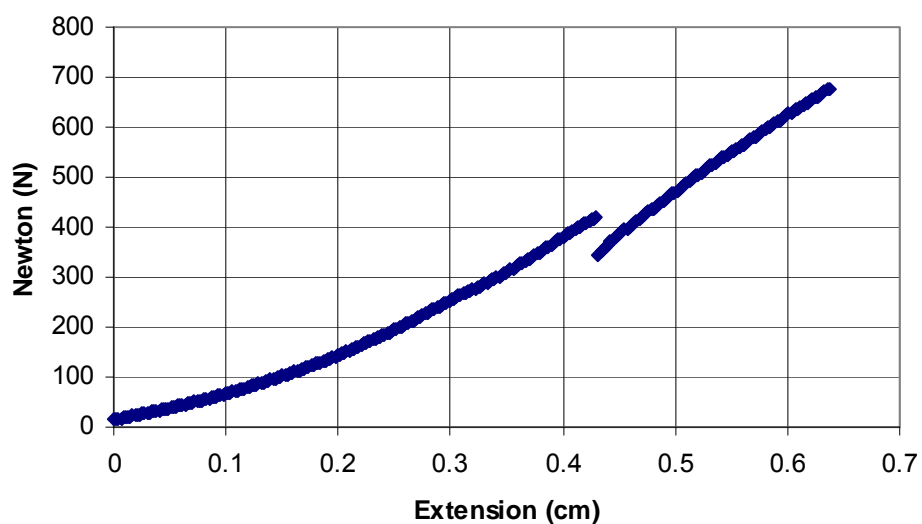


Figure I.7: Load-Extension Curve for Transverse Sample 2, Synthetic Carapace 2

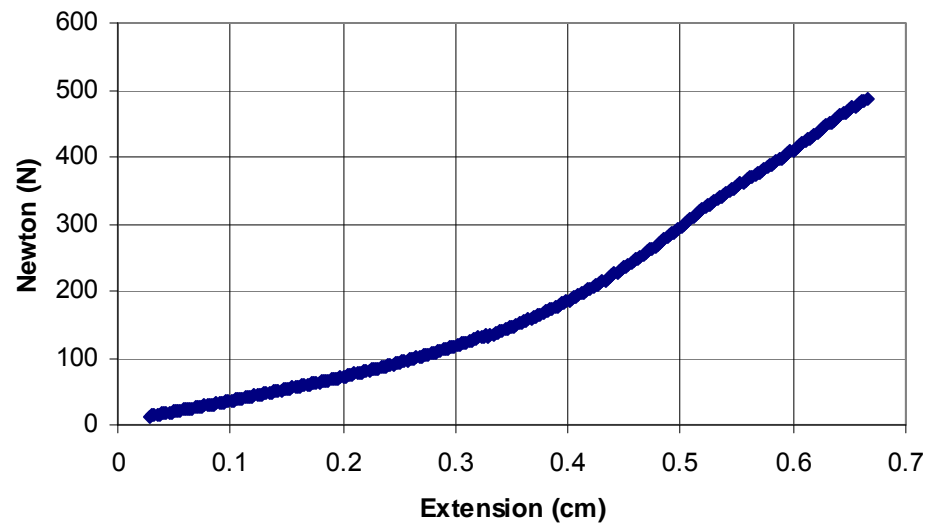


Figure I.8: Load-Extension Curve for Transverse Sample 3, Synthetic Carapace 2

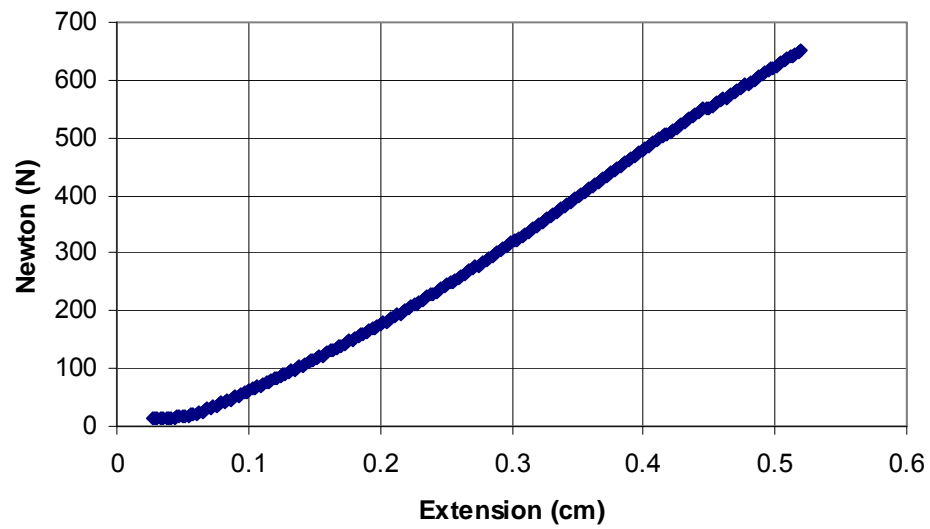


Figure I.9: Load-Extension Curve for Transverse Sample 4, Synthetic Carapace 2

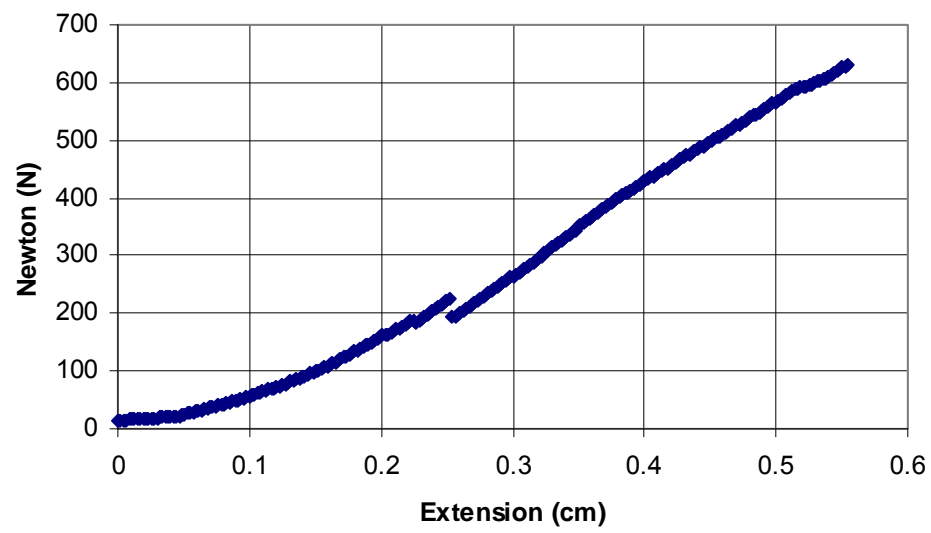


Figure I.10: Load-Extension Curve for Transverse Sample 5, Synthetic Carapace 2

References

- An, Y.H. and Draughn, R.A., (2000), Mechanical Testing of Bone and Bone-Implant Interface, CRC Press, Boca Raton, FL, pp. 175-206.
- ASTM C 565 – 93 (2005), Standard Test Method for Tension Testing of Carbon and Graphite Mechanical Properties, American Society for Testing and Materials.
- ASTM D 1623 – 03, Standard Test Method for Tensile and Tensile Adhesion Properties of Rigid Cellular Plastics, American Society for Testing and Materials.
- ASTM D 3039/D 3039M-00 (2006), Standard Test Method for Tensile Properties of Polymer Matrix Composite Materials, American Society for Testing and Materials.
- ASTM D 3420 – 95 (2002), Standard Test Method for Pendulum Impact Resistance of Plastic Film, American Society for Testing and Materials.
- ASTM D 790 – 07, Standard Test Method for Flexural Properties of Unreinforced and Reinforced Plastics and Electrical Insulating Materials, American Society for Testing and Materials.
- Balazs, G.H. (1979), “Loggerhead turtle recovered from a tiger shark at Kure Atoll”, *Hawaii Audubon Society Journal*, Vol. 39, No. 12, pp.145-147.
- Bruck, H. A., Evans, J.J., and Peterson, M.L. (2002), “The Role of Experimental Mechanics in Biological and Biologically Inspired Materials”, *Experimental Mechanics* Vol. 42, No. 4, pp. 361-371.
- Burstein, A.H., Zika, J.M., Heiple, K.G., and Klein, L. (1975), “Contribution of collagen and mineral to the elastic-plastic properties of bone”, *Journal of Bone and Joint Surgery Am.*, Vol. 57, pp. 956-961.
- Burstein, A.H., Reilly, D.T., and Martins, M. (1976), “Aging of bone tissue: mechanical properties”, *Journal of Bone and Joint Surgery Am.*, Vol. 58, pp. 82-86.
- Clifton, K. B., Yan, J., Mecholsky, J.J., and Reep, R.L. (2007), “Material properties of manatee rib bone”, *Journal of Zoology*, Vol. 274, pp. 150-159.
- Currey, J.D. (1984), “Effects of differences in mineralization on the mechanical properties of bone”, *Philosophical Transactions of the Royal Society of London. Series B, Biological Sciences*, Vol. 304, No. 1121, pp. 509-518.

- Dodd, C.K. (2006), "A bibliography of the loggerhead sea turtle *Caretta caretta* (Linnaeus, 1758) including references to fossils placed in the genus *Caretta*", <www.flmnh.ufl.edu/natsci/herpetology/caretta/caretta.htm>.
- Dodd, M. (2005), "Loggerhead turtle nesting in Georgia", Georgia Department of Natural Resources, Brunswick, GA.
- Dodd, M. (2005), "Summary of sea turtle issues for Cumberland Harbor permit appeal", Georgia Department of Natural Resources, Brunswick, GA.
- Ernst, C., Lovich, J., and Barbour, R., (1994), "Turtles of the United States and Canada", Smithsonian Institution Press, Washington, D.C.
- Frick, M. (2004), "New records and observations of epibionts from Loggerhead sea turtles", *Southeastern Naturalist*, pp. 613-620.
- Garita, B. and Rapoff, A.J. (2003), "Biomimetic Design from Bone," *Experimental Techniques, Biomechanics Series: Part 4*, pp. 36-39
- Gere, J. M. (2004), Mechanics of Materials, Brooks/Cole.
- Hazel, J. (2006), "Vessel-related mortality of sea turtles in Queensland, Australia", *Wildlife Research*, Vol. 33, pp. 149-154.
- Hazel, J., Lawler, I.R., Marsh, H., and Robson, S. (2007), "Vessel speed increases collision risk for the green turtle *chelonia mydas*", *Endangered Species Research*, Vol. 3, No. 2, pp.105-113.
- IUCN (2006), "2006 *IUCN* Red List of Threatened Species", <www.iucnredlist.org>.
- Karchin, A. (2004), "Mechanical Properties of Biomaterials", University of Washington Engineered Biomaterials, <www.uweb.engr.washington.edu/research/tutorials/mechproperties.html>.
- Li, S. H., Zeng, Q.L., Xiao, L., FU, S.Y., and Zhou, B.L. (1995), "Biomimicry of bamboo bast fiber with engineering composite materials", *Materials Science and Engineering*, Vol. 3, pp. 125-130.
- Loggerhead/Green Turtle Recovery Team (1991), Recovery plan for U.S. population of Loggerhead turtle, U.S. Department of Commerce and Atmospheric Administration and National Marine Fisheries Service, Washington, D.C., pp. 8-12.
- Magnuson, J. J., Bjorndal, K. A., DuPaul, W. D., Graham, G. L., Owens, D. W., Peterson, C. H., Pritchard, P. C. H., Richardson, J. I., Saul, G. E. and West, C. W. (1990), "Decline of the Sea Turtles: Causes and Prevention", National Research Council, National Academy of Sciences, Washington, DC, pp. 259.

Mayer, G. (2005), “Rigid Biological Systems as Models for Synthetic Composites”, *Science Magazine*, Vol. 310, No. 5751, pp. 1144-1147.

Milthorpe, B.K., Rogers, G.J. and Schindhelm, K. (1987), “Microcomputer – Based System for Tensile Testing of Biological Materials”, *Medical and Biological Engineering and Computing*, Vol. 26, No. 2, pp. 161 – 166.

Minamikawa, S., Naito, Y., Sato, K., Matsuzawa, Y., Bando, T., and Sakamoto, W. (2000), “Maintenance of neutral buoyancy by depth selection in the Loggerhead turtle *Caretta caretta*”, *Journal of Experimental Biology*, Vol. 203, No. 19, pp. 2967-2975.

National Marine Fisheries Service and the U. S. Fish and Wildlife Service (1991), “Recovery plan for U.S. population of loggerhead turtle *Caretta caretta*”, National Fisheries Service, Washington, DC. pp. 64.

National Marine Fisheries Service and the U. S. Fish and Wildlife Service (2007), “Loggerhead Sea Turtle (*Caretta caretta*) 5-Year Review: Summary and Evaluation”, National Fisheries Service, Washington, DC.

Norton, T. (2005), “Sea turtle conservation in Georgia and an overview of the Georgia Sea Turtle Center on Jekyll Island, Georgia” *Georgia Journal of Science*, Vol. 63, No. 4, pp. 208-231.

Plotkin, P.T. (Editor) (1995), “National Marine Fisheries Service and U. S. Fish and Wildlife Service Status Reviews for Sea Turtles Listed under the Endangered Species Act of 1973”, National Marine Fisheries Service, Silver Spring, Maryland.

Puxkandl, R., Zizak, I., Paris, O., Keekes, J., Tesch, W., Bernstorff, S., and Purslow, P. (2002), “Viscoelastic properties of collagen: synchrotron radiation investigations and structural model”, *The Royal Journal*, Vol. 357, No. 1418, pp. 191-197.

U.S. Fish and Wildlife Service (1978), ‘Listing and Protecting Loggerhead Sea Turtles as “Threatened Species” and Populations of Green and Olive Ridley Sea Turtles and Threatened Species or “Endangered Species”’, Federal Register, Vol. 43, No. 146.

Venizelos, L.E. (1993), “Speed boats kill turtles in Laganas Bay, Zakynthos”, *Mar. Turtle News*, Vol. 63, pp. 15.

Wang, X., Subramanian, A., Dhanda, R., and Agrawal, C.M. (1996), “Testing of Bone-Biomaterial Interfacial Bonding Strength: A Comparison of Different Techniques”, *Journal of Biomedical Materials Research (Applied Biomaterials)* Vol. 33, No. 3, pp. 133-138.

Wang, X., Bank, R.A., Tekoppele, J.M., and Agrawal, C.M. (2001), “The role of collagen in determining bone mechanical properties”, *Journal of Orthopedic Research*, Vol. 19, No. 6, pp. 1021-1026.

Yiatros, S., Wade, M.A., and Hunt, G.R. (2007), “The load-bearing duct: biomimicry in structural design”, Institution of Civil Engineers, *Engineering Sustainability*, Vol. 160, No. 4, pp. 179-188.